Separated Viscous Flows via Multigrid

Thesis by

Robert Iain McLachlan

In Partial Fulfillment of the Requirements

for the Degree of

Doctor of Philosophy

California Institute of Technology

Pasadena, California

1990

(Submitted April 19, 1990)

Separated Viscous Flows via Multigrid

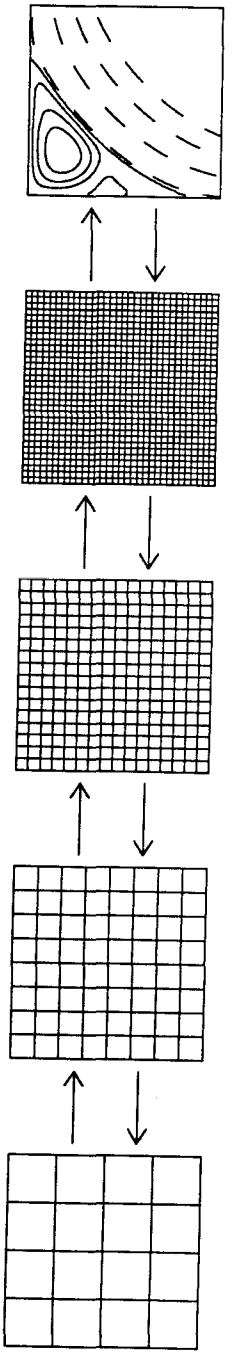

Robert McLachlan

California Institute of Technology

Acknowledgements

I would like to thank my advisor, Herb Keller, for much assistance and for continued support as the scope of the thesis evolved; Philip Saffman, for helpful discussions on the physical basis of fluid mechanics and triple deck theory; Derek Moore, for suggesting the corner flow as worthy of study, to which we owe all our positive results; Stephen Cowley, for his enthusiasm and for suggesting the integral test of §3.4.2; Eric van de Velde, for providing me with his clearly coded multigrid Poisson solver; Cathy Hayes, Vidyadhar Mudkavi and Rachel Shinn-Mendoza for informal discussions and for enlivening the Guggenheim annex; and Julie Seko for her support and encouragement.

While at Caltech I was supported by institute teaching assistantships, by contracts DOE DE-FG03-89ER25073 and ARO DAAL03-89-K-0014, and was generously allowed to hold a New Zealand University Grants Committee Scholarship.

This thesis is dedicated to my parents, Colin and Elizabeth M^{c}Lachlan.

Abstract

A multigrid code is developed to solve general systems of convection-diffusion equations when the diffusion terms are small, i.e., when the Reynolds number is large. Various upwinding, artificial viscosity and defect correction schemes are considered and compared. The code is applied to the Navier-Stokes equations for various flow configurations and used to study boundary layer separation from a leading edge, with ensuing formation of a downstream eddy. The asymptotic ("triple deck") theory of separation is developed for this case, following Sychev, and compared to the numerical calculations at Reynolds numbers of up to 5000. Much better qualitative agreement is obtained than has been reported previously. Together with a plausible choice of two free parameters, the data can be extrapolated to infinite Reynolds number, giving quantitative agreement with triple deck theory with errors of 20% or less. The development of a region of constant vorticity is observed in the downstream eddy, and the global infinite Reynolds number limit is a Prandtl-Batchelor flow; however, when the plate is stationary, the occurrence of secondary separation suggests that the limiting flow contains an infinite sequence of eddies behind the separation point. Secondary separation can be averted by driving the plate, and in this case the limit is a single-vortex Prandtl-Batchelor flow of the type found by Moore, Saffman and Tanveer (1988); we make detailed, encouraging comparisons of the vortex sheet strength and position. By altering the boundary condition on the plate we obtain viscous eddies that approximate different members of the family of inviscid solutions. The code is also used to calculate the flow over a finite flat plate aligned with a uniform free stream; in that case, earlier conflicting results about higher-order corrections to the boundary layer are explained, and the triple deck generally believed to be established around the trailing edge is found to be consistent with the numerical results. There remains a large displacement-like effect in the boundary layer, whose exact origin is unclear.

Contents

List of Figures

List of Tables

Chapter One

Introduction

The nature of the steady laminar flow of an incompressible fluid in the limit of small viscosity has received a great deal of attention ever since Prandtl's discovery in 1905 of the boundary layer that forms in such a flow next to a wall. Of course, in all real fluids, the steady flow, while presumably still existing as a solution of the equations of motion, is unstable when the viscosity is small enough. Nevertheless, unstable steady flows are studied for several reasons.

First, the flow may be of interest in itself, if it has desirable properties such as high lift or low drag in an airfoil; there may be a way to stabilize the flow while retaining its essential features.

Second, there is a large body of fluid mechanics research devoted to the study of an incompressible, inviscid fluid; one would like to know exactly when, and in what regions of the flow, these assumptions are valid. Extending from this is the hope that once the limiting steady laminar flow had been found, an asymptotic expansion could be constructed about it which would be relevant when the viscosity was large enough for laminar flow to be stable. Although some progress has been made in this direction, much of the information we have about steady flows with small viscosity comes from numerical calculations. It has turned out that asymptotic high-Reynolds number theories are complicated and contain many assumptions about non-local regions of the flow; in addition, the limit can be reached extremely slowly, so that very large Reynolds numbers are required to see the limit clearly.

Finally, finding $\lim_{\nu \to 0} \mathbf{u}$ is an interesting problem of mathematical physics in itself, which has been around at least since the Kirchoff-Helmholtz free-streamline theory of 1867 and is still not completely solved.

To study these flows, we have investigated one possible method for finding high Reynolds number flows numerically and have applied it to a class of flows in a corner.

The results are then examined for their implications regarding both the global limit at high Reynolds number, and the way in which boundary layers separate from near a leading edge.

In calculating solutions to the steady state Navier-Stokes equations, many traditional numerical methods break down when the solution to the full, time-dependent equations is unstable. In addition, the numerical grid must be very fine in order to resolve the thin boundary and shear layers that develop, and to avoid erroneous "wiggle" modes in the solution of the discretized equations. With fast computers, and particularly with enormous memories, it is now possible to use Newton's method directly on the system of discretized equations. Three successful applications of this approach are the work of Schreiber and Keller (1983, driven cavity flow up to Re=10,000), Milos, Acrivos and Kim (1987, cascade expansion flows up to Re=1000), and Fornberg (1985, flow past a cylinder up to Re=600).

On an $N \times N$ computational grid, the memory requirement for Gaussian elimination with diagonal ordering is $4N^3$, and the computational work is $O(N^4)$, which quickly exhausts any computer. We decided to investigate the use of multigrid, in which the memory and work requirements are both $O(N^2)$, to solve the equations. We have developed a general multigrid code to solve systems of elliptic equations of the form

$$-\nabla^2 \mathbf{u} + \mathbf{f}(\mathbf{x}, \mathbf{u}, \nabla \mathbf{u}) = \mathbf{0} \tag{1.1}$$

in two space dimensions when the Reynolds number is large; it is described in Chapter 2. Note that the stream function-vorticity form of the Navier-Stokes equations is in the form (1.1). It was felt that this approach would be more useful for testing and also for future applications than a specialized Navier-Stokes code.

Multigrid methods start from the observation that many common relaxation methods (such as Gauss-Seidel) reduce high frequency errors much faster than they do low frequency errors, so it would be more efficient to deal with the low frequencies on a coarser grid, such as one in which the mesh size is doubled in both directions.

In this way the solution proceeds through a series of ever coarser grids, the last being one on which the equations can easily be solved exactly. It is then possible to obtain almost the same convergence rate for the whole solution as for the high frequencies alone. This explains why the number of iterations required is independent of the number of grid points. It remains only to specify the way in which the solution is moved from one grid level to the next. A standard reference, which discusses these and many other considerations, is A. Brandt's *Guide to Multigrid Development.*

When the Reynolds number is large, many relaxation methods become unstable and no longer reduce the defect, essentially because the matrix associated with a centered difference formulation is no longer diagonally dominant when the cell Reynolds number (roughly hRe, where h is the mesh spacing) is greater than 2. This is particularly a problem for multigrid, which must still function on the coarser grids, where h is quite large. One way of dealing with this is to use corrected upwind differences, which can be stably smoothed and preserve the second order accuracy of the solution. This approach has been used by Schröder and Keller (1989), who used alternating direction line relaxation, and by Ghia, Ghia and Shin (1983), who used a relaxation method similar to incomplete lower-upper (ILU) decomposition. However, in our experience, even with sophisticated smoothers, this method will always exhibit slow smoothing when the cell Reynolds number becomes large. Instead, we concentrated on more general defect correction methods, which have the advantage that simple, fast smoothers with tiny memory requirements can be used, while still retaining adequate convergence rates (usually about 0.3 per iteration) when the cell Reynolds number is large.

Chapter 2 outlines the general approach of such methods, culminating in Brandt's double-discretization scheme. This is applied to several test problems that demonstrate that second order accuracy is retained at large Reynolds numbers, and that the accuracy is as good as in previous solutions of the Navier-Stokes equations.

The infinite Reynolds number limit of a viscous flow is expected to be at least a weak solution of the Euler equations for the motion of an incompressible, inviscid

fluid. The problem is that in most geometries there are many such solutions. For example, in flow past a cylinder, in addition to the irrotational solution there is a Kirchoff-Helmholtz free-streamline solution in which vortex sheets are attached to the cylinder 55° from the forward stagnation point and extend downstream to infinity, enclosing a region of stagnant fluid; there is the Föppl solution, irrotational except for two point vortices in the wake; there may also exist Batchelor solutions with a finite, rotational wake behind the cylinder; and the best numerical evidence now indicates that the actual limit may be a Sadovskii vortex which becomes infinitely large as the viscosity tends to zero. Selecting the correct limit would mean, at the least, constructing a consistent expansion about one of these flows, valid when the viscosity is very small but not zero.

We have concentrated on the type of solution, discussed by Batchelor (1956), in which closed-streamline regions have constant vorticity and are separated from each other (and from any external, irrotational flow) by walls or vortex sheets. The driven cavity (see, e.g., Schreiber and Keller (1983)) presumably tends to such a flow, inasmuch as all its streamlines are closed, and in fact high Reynolds number calculations show that the vorticity does become roughly constant in the main vortex. However, no Batchelor flows have been calculated in a square (perhaps because of the profusion of walls and vortex sheets!), so detailed comparisons cannot be made. Another candidate for a Batchelor flow as a limit was found by Milos, Acrivos and Kim(1987). In their geometry, straight channels in a periodic array join over a vertical step. For certain values of the ratio of channel widths before and after the step, it appeared that the downstream eddy eventually stopped growing as the Reynolds number increased. Once again, no inviscid calculation has been performed, although it would be easier to do in this case.

In this regard, D. Moore suggested that we study the corner flow sketched in Figure 1.1. The uniform straining field $\psi = -xy$ is an exact solution of the Navier-Stokes equations; however, when a flat plate is introduced at $y = 0$, $-1 < x < 1$, the flow separates shortly after hitting the plate and a counter-rotating eddy forms in

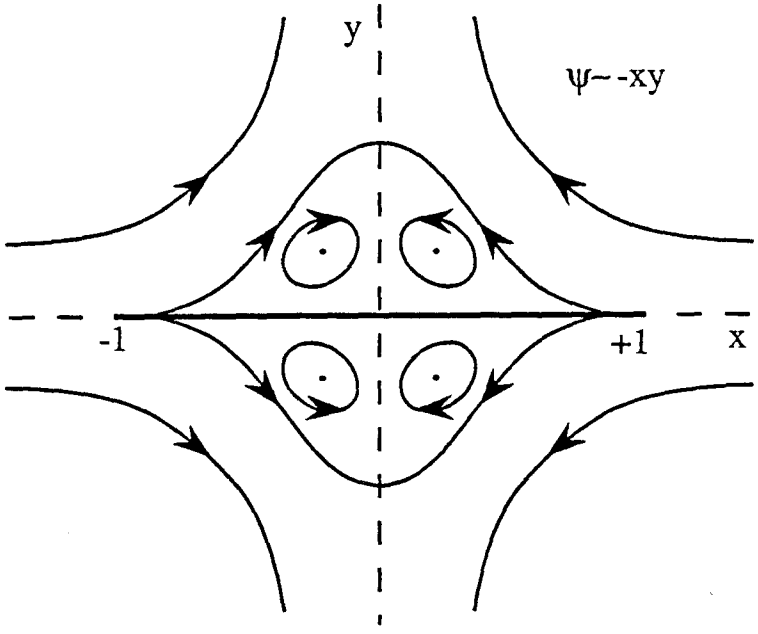

Figure 1.1 Corner flow geometry

the corner. Inviscid calculations have been done in this geometry by Moore, Saffman and Tanveer (1988), who found a whole family of Batchelor flows, parameterized by the eddy vorticity ω. An example is sketched in Figure 1.2; as ω increases, the eddies bulge out more. The corner flow is of interest not only for a possible Batchelor limit, but as a simple example of the separation of a boundary layer—an area in which it might be said that theory outstrips calculations.

This flow was first studied by L.G. Leal (1973), who obtained solutions up to a Reynolds number of 400, at which point the eddy still appeared to be fully viscous. In Chapter 3, we extend the calculations to a Reynolds number of 5000. Extensive checks of convergence and accuracy are made, including a test of the integral property of the Navier-Stokes equations that the total flux of vorticity through a closed streamline is zero. Most flow quantities are accurate to within a few tenths of a percent or less.

By Reynolds number 3000 the transition to an inviscid eddy is clear. The formation of a region of constant vorticity is seen in the main part of the eddy, and there is no evidence of any of the phenomena that might prevent the limit from being a Batchelor flow. However, at a Reynolds number of 2255, the reverse boundary layer

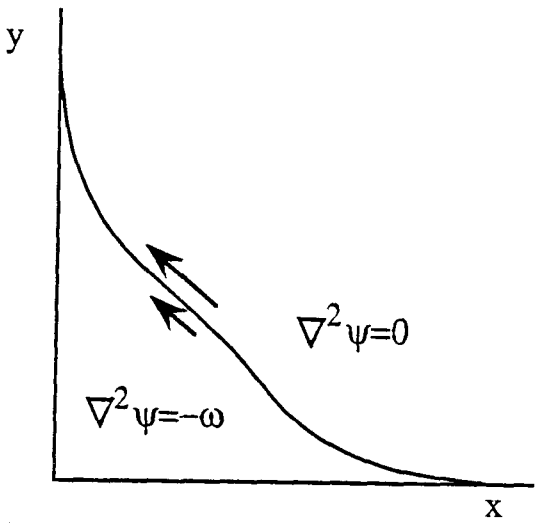

Figure 1.2 Batchelor flow in a corner

Only one quadrant is sketched; the flow is symmetric about $x = 0$ and $y = 0$, with the sign of the constant vorticity ω depending on the quadrant.

that is set up against the wall downstream itself separates, forming a secondary eddy. This means that the limit cannot be one of the one-eddy flows of Moore et al., and complicates the theoretical picture considerably.

To sidestep those difficulties for the moment, we changed the boundary condition at the wall to prevent secondary separation. These flows are given in Chapter 4. With $u(x, 0) \equiv u_p > 0$, the reverse boundary layer is accelerated instead of retarded by the wall, and remains attached. This also strengthens the main eddy considerably, causing the emergence of inviscid behavior in the corner at a lower Reynolds number, and pushes the primary separation point upstream to just ahead of the plate. The eddy now looks almost identical to those of Moore et al. and we make detailed, encouraging comparisons of the eddy shapes and the vortex sheet strengths with Batchelor flows. By changing the wall boundary condition, Batchelor flows with different vorticity levels can be found. We conclude that a simple Batchelor flow is the high Reynolds number limit in this case.

In Chapter 5 we turn our attention to the separation of the boundary layer in the original corner flow of Chapter 3. The currently accepted explanation of this is given by triple deck theory, first developed using the method of matched asymptotic expansions by V.V. Sychev in 1972 for separation from bluff bodies, and in 1979 for

separation from a leading edge, as here. It holds that separation is governed by a free interaction between the boundary layer and the external flow with the large pressure gradient acting over a small distance being just that required to prevent the Goldstein singularity. More specifically, the external flow is assumed to be locally a Batchelor flow, which has a singularity in the pressure gradient at separation; the form of that singularity is then used to derive the scale of the small interaction region. One is left with the standard boundary layer equation with unusual boundary conditions (the "lower deck problem"), which was solved by Smith (1977), among others.

We examine the dependence of various flow quantities near separation on the Reynolds number. It is found that the skin friction and the pressure gradient scale almost exactly as predicted by triple deck theory. Such good agreement has never before been found (for example, it is certainly not evident in the bluff body separation results of Fornberg (1985)). In addition, their profiles are qualitatively similar to the lower deck solution. Encouraged by this, we next attempt to make a detailed comparison by determining the two constants in the theory which are supplied by the global inviscid flow. It turns out that there are no values of the parameters that will reduce the differences between the computed flows and the lower deck solution below about a factor of two, even though the flow near separation has definitely entered an asymptotic regime. In addition, the position of the separation point as a function of the Reynolds number, while well behaved ($x_{\text{sep}} \sim Re^{-0.34}$), is nowhere near the position given by triple deck theory ($x_{\text{sep}} \sim Re^{-1/9}$).

Some of these discrepancies are explained by a higher order matching. Most flow quantities near separation are seen to depend linearly on $\varepsilon = Re^{-1/9}$, although over such a small range in ε that quadratic or higher order behavior cannot be ruled out. Even so, taking plausible values for the free parameters and extrapolating the finite Reynolds number results linearly in ε to $\varepsilon = 0$ removes all the qualitative discrepancies with triple deck theory and reduces the quantitative disagreement to about 20%. A higher order matching also explains the behavior of x_{sep}, although in this case the leading order effect is so small that it is hard to capture in the data.

We thus believe that the Sychev model of laminar separation has been fully confirmed.

Chapter 6 is independent of the rest of the thesis, and concerns a flow that is literally a textbook example in boundary layer theory (Van Dyke, 1964): the flow over a finite flat plate aligned with a uniform free stream. This would appear to be much simpler than the previous examples in that both the zeroth order solution (no disturbance to the free stream) and the first order solution (the Blasius boundary layer) are known. Difficulties arise at the next order, where a multitude of competing effects appear, and when we try to explain results from finite Reynolds number calculations.

In our investigations of the triple deck, we turned to the finite flat plate as a case in which it was known to apply and seemed to have been confirmed numerically. The theory at first appears to be easier to test in this case because it has no undetermined constants. Here the triple deck is established around the trailing edge and gives the upstream effect on the boundary layer of the singular near wake, with a contribution to the drag of $2.66Re^{-7/8}$. This agrees with Navier-Stokes calculations (Jobe and Burggraf (1974)). However, prior to the discovery of the triple deck, the second order theory of Kuo (1953), which gives the correction to the first order drag as $4.12Re^{-1}$, also seemed to be in agreement. Furthermore, a glance at the results of Dennis and Dunwoody's 1966 finite Reynolds number calculations shows that neither theory explains the calculated values of the skin friction on the plate. We decided to do some Navier-Stokes calculations ourselves to see what was really going on.

It turns out that finite Reynolds number results are greatly influenced by the small viscous regions at the leading and trailing edges in which the full Navier-Stokes equations hold. These make it impossible to see any triple deck trailing edge region directly. However, by constructing a least squares fit between the numerical data and a model theory, we can show that the triple deck theory is at least consistent with the data. One reason that the triple deck's trailing edge effect is not obvious is that there is a large displacement-like effect in the boundary layer, i.e., an $O(Re^{-1})$

increase in skin friction extending over the whole plate. Even at $Re = 600$, the largest Reynolds number considered, this was comparable in magnitude to the triple deck effect. An $O(Re^{-1})$ increase would correspond to the displacement effect of the Blasius boundary layer on the external flow, except that numerically it is about half the size of the effect calculated by Kuo.

Finally, we construct a model of the flow that includes all these effects, and show that the apparent agreement in drag found by previous workers is in fact a coincidence that is due to near cancellation of the next smallest terms of the drag expansion.

We have found multigrid to be a practical method of solving the steady-state Navier-Stokes equations. It is harder to implement than other popular solvers, and care must be taken at the boundaries if full efficiency is to be obtained. Another drawback is that it gives less information about the solution than does Newton's method (such as the occurrence of bifurcations), and that when convergence breaks down it is hard to locate the problem, although all methods suffer from this to some extent. (For example, Newton's method may require ever smaller continuation steps, or it may become impossible to solve the linear systems to the required accuracy.)

In return, solutions can be found very quickly on extremely fine grids. Solving the Navier-Stokes equations in the work of a few dozen Gauss-Seidel iterations can certainly stand as a useful benchmark.

Chapter 2

Multigrid methods

2.1 The basic multigrid algorithm.

As discussed in Chapter 1, we wish to solve the equation

$$-\nabla^2 \mathbf{u} + \mathbf{f}(\mathbf{x}, \mathbf{u}, \nabla \mathbf{u}) = \mathbf{0}, \tag{2.1}$$

which for the current description can be regarded as discretized as

$$L^k u^k = F^k, \tag{2.2}$$

where k identifies a grid with mesh size h_k. The problem (2.2) is to be solved on a sequence of M grids with mesh sizes $h_k = 2^{-k} h_0$, $0 \leq k < M$. One iteration of multigrid consists of smoothing the high frequency errors on a particular grid by relaxation, then solving for the low frequency errors by applying multigrid to the next coarser grid. It is thus inherently recursive. On the coarsest grid, the equations are solved either exactly or iteratively until the error is much smaller than the discretization error; because of the small number of equations, this is not expensive. Thus, both the relaxation method and the processes for transferring between grids need to be specified.

Let I be an interpolation operator from coarse to fine grids. Bilinear interpolation is the simplest method that maintains the order of accuracy of the corrections and is usually used. That is, the coarse grid values are simply injected into the fine grid, and the remaining fine grid unknowns are given by the linear average of their nearest neighbors.

Sometimes two restriction operators are specified: one for defects and one for solution values. However, for nonlinear problems these are both usually taken to be

the "full weighting operator" R: coarse grid values are given by the computational molecule

$$u_{i,j}^{k-1} = \frac{1}{16}\begin{bmatrix} 1 & 2 & 1 \\ 2 & 4 & 2 \\ 1 & 2 & 1 \end{bmatrix} u_{2i,2j}^{k} \equiv R u_{2i,2j}^{k}. \tag{2.3}$$

Now one iteration of the FAS ("Full Approximation Scheme", so-called because the unknowns themselves rather than just the corrections are maintained on the coarse grids) multigrid method is defined as follows:

- Smooth the high-frequency error on grid k by applying ν_1 relaxations to (2.2). If $k = 0$, solve (2.2) to high accuracy by using sufficient relaxations.
- Set up problem on grid $(k-1)$, the solution to which will correct the low-frequency errors on grid k. Another way of looking at this is to note that we correct the right hand side of the grid $(k-1)$ problem so that its solution is the interpolation of the fine grid solution.

$$\begin{aligned} u^{k-1} &= Ru^k \\ F^{k-1} &= R(F^k - L^k u^k) + L^{k-1}u^{k-1} \end{aligned} \tag{2.4}$$

- Solve the grid $(k-1)$ problem by applying this algorithm recursively: i.e., apply multigrid γ times to the coarse grid problem $L^{k-1}u^{k-1} = F^{k-1}$.
- Incorporate the corrections from the coarse grid to the fine grid. Note that interpolating the coarse grid solution itself would destroy the high frequency improvements made in the first step.

$$u^k = u^k + I(u^{k-1} - Ru^k) \tag{2.5}$$

- Relax the fine grid ν_2 times.

If the coarse grid problem were solved exactly, there would still be only a finite convergence rate on the fine grid (the "two-grid rate"), controlled by the worst-smoothed high frequency component of the error (and affected by the intergrid transfers). So there is no point in solving the coarse grid problem more accurately than necessary. In practice, using $\gamma = 1$ or 2 will usually almost attain the two-grid rate. One iteration with $\gamma = 1$ is called a V-cycle, because the algorithm descends step by step from

level k to level 0 and back to k; one iteration with $\gamma = 2$ is called a W-cycle because of the schematic representation when $k = 2$ (i.e., grid $2 \to 1 \to 0 \to 1 \to 0 \to 1 \to 2$).

Instead of starting with $u^{M-1} = 0$, the first approximation is usually found by interpolating the solution from the next coarser grid. In this way, we start by solving the problem on the coarsest grid, and progress upwards. The interpolation operator I^* used in this process can be profitably of a higher order than I, because solutions are usually smoother than corrections. This is particularly important in our application to the Navier-Stokes equations because the stream function is quadratic near the wall; failure to do so would result in $O(1)$ errors when the new boundary values are calculated. Commonly bicubic interpolation is used. In our implementation, first the coarse grid values were injected; then fine grid points with one coordinate coincident with the coarse grid were interpolated in that direction only; finally the remaining values could be found using the just-calculated adjacent fine grid values.

This gives the FMG ("Full Multigrid") algorithm:

- Solve $L^0 u^0 = F^0$ by relaxation
- For $k = 1, \ldots, M-1$, set $u^k = I^* u^{k-1}$ and solve $L^k u^k = F^k$ by N iterations of FAS multigrid.

2.2 Implementation.

A C code implementing the above algorithm for Helmholtz problems of the form

$$\begin{aligned} -\nabla^2 u + f(\mathbf{x}, u) = 0 \qquad & \text{in } \Omega = [a,b] \times [c,d], \\ u = g \qquad & \text{on } \partial\Omega \end{aligned} \tag{2.6}$$

had already been written by Eric Van de Velde and has been described extensively by him elsewhere. His main interest was in parallel implementation, not in solving a particular problem. We decided to adapt his program for the more general vector equation (2.1). Further, with an eye to eventual application to the Navier-Stokes equations, more general boundary conditions would be required, of the form

$$\mathbf{u_0} = \mathbf{g}(\mathbf{x}, \mathbf{u_1}), \tag{2.7}$$

where $\mathbf{u_0}$ is a vector of unknowns at a boundary point and $\mathbf{u_1}$ the unknowns at an immediately interior point. This allows for Dirichlet and Neumann boundary conditions, as well as for coupled Woods-type expansions of the no-slip condition (see §3.3). It does not allow for writing the discretized equation at the boundary point itself and eliminating any exterior points; this was thought to be an unnecessary complication.

When solving systems, the interpolation and restriction operators carry over easily: they can be applied to each unknown in turn. The relaxation process is more complicated. The Newton linearization of (2.1) is

$$-\nabla^2\mathbf{u}^{n+1} + \mathbf{f}_u\mathbf{u}^{n+1} + \mathbf{f}_{\nabla u}\nabla\mathbf{u}^{n+1} = -\mathbf{f}(\mathbf{u}^n) + \mathbf{f}_u\mathbf{u}^n + \mathbf{f}_{\nabla u}\nabla\mathbf{u}^n, \qquad (2.8)$$

where the Jacobians are evaluated at $\mathbf{u}^n$. It is clear that the relaxations will need access not just to $\mathbf{f}$, but to the three Jacobian matrices $\mathbf{f}_u$, $\mathbf{f}_{u_x}$, and $\mathbf{f}_{u_y}$. Furthermore, it is possible to insert the Newton linearized boundary condition when these values are needed in the interior relaxations; this requires the matrix $\mathbf{g}_v$. Once subroutines returning these values are supplied, virtually any equation of the type (2.1) with boundary conditions (2.7) can be handled. Of course, that allows many phenomena that are difficult to handle, such as singularities and indefiniteness; we concentrated on those problems arising in the solution of the Navier-Stokes equations. However, using a general implementation was useful for testing and comparison with other multigrid experiments.

2.3 Defect correction.

There are two reasons why the initial discretization (2.2) may not be suitable or adequate: we may want a solution of higher-order accuracy, without solving the higher-order equations directly; or it may be difficult to stably relax the equations as discretized, even though their solution is smooth. Multigrid is ideally suited to dealing with these problems without extra work: usually, the difference between the solution to the high- and low-order discretizations is mostly in the low frequencies,

and can be handled on the coarse grid, i.e., by choosing the intergrid transfers and the coarse grid problem appropriately. In fact, the original FAS algorithm is just a technique for solving for part of the fine grid defect.

In our case the problem is that most relaxation methods (for example, all point and line methods) become unstable when applied to center-differenced convection-diffusion equations in which convection greatly dominates diffusion. Here a "stable" relaxation of $Lu = F$ is one that reduces the defect $F - Lu$ when u is close enough to the solution $L^{-1}F$; a stable smoother need only reduce the high frequencies of the defect. Gauss-Seidel relaxation applied to the equation

$$-\nabla^2 u + au_x + bu_y = 0, \tag{2.9}$$

discretized using central differences with mesh spacing h in the x direction and k in the y direction, for example, is stable only when the "cell Reynolds number," $\alpha = |ah| + |bk|$, is less than 2. The earliest way of dealing with this problem was to use upwind differencing on the convection terms, that is, one-sided differences in the direction opposite to the convection. Here a left difference $(u_i - u_{i-1})/h$ would be used if $a > 0$. Upwind differencing leads to stable relaxation, and although it is only first-order accurate, as late as 1980 it was applied to many high Reynolds number problems. Eventually it was realized, of course, that since upwind differencing is equivalent to adding artificial viscosity proportional to the Reynolds number Re, past a certain Re (once α is much greater than 2), the numerical solution does not depend on Re at all.

One way to combine the $O(h^2)$ accuracy of central differences with the stability of upwinding is to use upwind-corrected differences. Consider the discretization of u_x. This can be decomposed as

$$\begin{aligned} \frac{1}{2h}(u_{i+1} - u_{i-1}) &= \frac{1}{h}(u_i - u_{i-1}) + \frac{1}{2h}(u_{i+1} - 2u_i + u_{i-1}) \\ \text{or} \qquad \Delta_x^0 u &= \Delta_x^- u + \frac{h}{2}\Delta_{x\bar{x}} u \end{aligned} \tag{2.10}$$

and similarly for right differences. This shows that if upwinding is used, we can retain second order accuracy by adding an artificial viscosity term to the right hand side.

To put these considerations in a more general framework, we construct a general $O(h)$ discretization $\tilde{L}u = 0$ of (2.9), which can be stably relaxed, then extend it to more general equations such as (2.8). One method is to use upwind differences on the convection terms:

$$-(\Delta_{x\bar{x}} + \Delta_{y\bar{y}})u + a\Delta_x^{\mp}u + b\Delta_y^{\mp}u = 0, \tag{2.11}$$

where we take a left difference Δ_x^- if $a > 0$ and a right difference Δ_x^+ if $a < 0$, and similarly for $\Delta_y^{\mp}$. From (2.10), this can be rewritten as

$$-(\Delta_{x\bar{x}} + \Delta_{y\bar{y}})u + a(\Delta_x^0 \mp \frac{h}{2}\Delta_{x\bar{x}})u + b(\Delta_y^0 \mp \frac{k}{2}\Delta_{y\bar{y}})u = 0 \tag{2.12}$$

or

$$-\left((1 + \frac{h|a|}{2})\Delta_{x\bar{x}} + (1 + \frac{k|b|}{2})\Delta_{y\bar{y}}\right)u + a\Delta_x^0 u + b\Delta_y^0 u = 0. \tag{2.13}$$

When applied to the linear operator on the left hand side of (2.8), this approach means using centered differences on the convection terms, as in L, and adding an artificial viscosity. A slight generalization of (2.13) gives

$$\tilde{L}u = -(d_x\Delta_{x\bar{x}} + d_y\Delta_{y\bar{y}}) + \text{convection terms}, \tag{2.14}$$

where the artificial viscosity coefficients d_x and d_y are given by

$$\begin{aligned} d_x &= \max(1, \beta h|f_{u_x}|), \\ d_y &= \max(1, \beta k|f_{u_y}|). \end{aligned} \tag{2.15}$$

This form of d_x and d_y is chosen so that in regions where there is little convection (such as near walls), the original $O(h^2)$ discretization is recovered; elsewhere, where d_x is large, the difference between (2.13) and (2.14) is not significant in our context.

$\beta = 1/2$ corresponds to upwind differencing. In the case of many unknowns, cross terms coupling the equations cause no problems; so here for f_{u_x} we use the diagonal entries of $\mathbf{f_{u_x}}$. Now that we are not limited to direct upwinding, we can experiment with different schemes: for example, making β depend on the grid level, or using isotropic artificial viscosity, i.e., $d_x' = d_y' = \max(d_x, d_y)$. De Zeeuw and van Asselt

(1985) investigated many such schemes in a multigrid context, and concluded that for fastest convergence one should use $\beta = 1/2$ on the finest grid and $\beta = 1$ on all coarser grids, and we verified their numerical experiments in the process of testing our code; but as they did not considering *removing* the added viscosity, these schemes are not useful for our problem.

We now have two discretizations of our original equation (2.1): an $O(h^2)$ one, $L^k u^k$, using central differences, and an $O(h)$ one, $\tilde{L}^k u^k$. With this notation we can write the corrected-difference iteration for the solution of $L^k u^k = F^k$ as

$$\tilde{L}^k u^{k,n+1} = \tilde{L}^k u^{k,n} + (F^k - L^k u^{k,n}). \tag{2.16}$$

There is another way to view this: with regard to the Newton linearization (2.8), upwind-correcting is equivalent to using upwind differences in the Jacobians but central differences in $\mathbf{f}$. Clearly the fixed point of the iteration will be second order accurate.

This method was used successfully by Schröder and Keller (1989) in a 3-D calculation of wavy Taylor vorticies. However, it is not suitable for arbitrarily high Reynolds numbers. Because (2.16) as described above is no longer the Newton linearization of (2.1), solving it exactly will lead to only linear convergence. If that linear rate of convergence if fast enough, this procedure is adequate because in a multigrid context, (2.16) is only relaxed, not solved exactly.

To investigate this question, we considered the corrected difference iteration (2.16) applied to the linear convection-diffusion equation (2.9) using standard Fourier error analysis. Substitution of an error term consisting of the Fourier mode $e^{imx+imy}$ in the case $b = -a$ shows that it is reduced by an amount $\alpha/(2+\alpha)$, independently of the mode m. That is, the convergence rate of (2.16), when solved exactly for $u^{k,n+1}$, tends to zero as the cell Reynolds number $\alpha \to \infty$. This is bad news if we hope to adapt (2.16) for use in multigrid, which can tolerate poor smoothing in the low frequency components of the error only. Furthermore, this $1 - O(\alpha^{-1})$ error reduction was also found to hold in applying multigrid to the Navier-Stokes equations. Since

we are hoping to have smoothing rates of at least 0.5, being limited to $1 - O(\alpha^{-1})$ is clearly inadequate. We therefore consider more general defect correction techniques.

If we abandon the idea of convergence to the exact solution of (2.2), we can construct much more robust schemes: we smooth only with respect to the stable operator $\tilde{L}$, and correct any errors later:

- Smooth $\tilde{L}^k u^k = F^k$
- Correct the defect: $\tilde{L}^k u^{k,n+1} = \tilde{L}^k u^{k,n} + (F^k - L^k u^{k,n})$. (2.17)

Because we have mixed operators, this system cannot have the same solution as (2.2). Auzinger (1987a, b) gives a representation of the altered solution and interprets (2.17) as a variant of (2.16) with a "stabilized" discretization. There is no reduction of the order of accuracy of the solution if the problem is "sufficiently smooth." Such proofs are not available for the Navier-Stokes equations, and we rely on comparison with previous solutions and on mesh refinement to determine accuracy.

For many problems, the difference between the two operators L and $\tilde{L}$ is mostly in the low freqency components. (If it is not, (2.17) will show poor convergence anyway). In this case we can conveniently combine the two steps by relegating the defect correction to the coarse grid:

- Smooth $\tilde{L}^k u^k = F^k$
- Solve $\tilde{L}^{k-1} u^{k-1} = \tilde{L}^{k-1} R u^k + R(F^k - L^k u^k)$ via multigrid. (2.18)

An analysis of this method is given in Hackbusch's book (1985). At this point we would like to apply the multigrid philosophy to the coarse grid problem itself, i.e., use the same technique to get an $O(h^2)$ solution on the coarse grid. This would enable the defect corrections to be applied on every level. However, we cannot simply replace $\tilde{L}^{k-1}$ by L^{k-1} since we need to use $\tilde{L}$ for smoothing. The remedy is to use two right hand sides on each level below the finest: F^k, to be used in computing the defect correction needed on level $(k-1)$, and $\tilde{F}^k$, to be used for smoothing on level k. This results in the *double-discretization* scheme of Brandt (1984):

- Smooth $\tilde{L}^k u^k = \tilde{F}^k$

- Compute the defect on the coarse grid, $d^{k-1} = R(F^k - L^k u^k)$.
- Set $F^{k-1} = L^{k-1} R u^k + d^{k-1}$,
  and $\tilde{F}^{k-1} = \tilde{L}^{k-1} R u^k + d^{k-1}$.
- Apply multigrid to level $(k-1)$, starting with $u^{k-1} = R u^k$, and interpolate the corrections as usual.

Note that there is no smoothing performed after interpolation of the corrections. Although including it would not degrade the *order* of the approximation of u^k, it would certainly increase the size of the error, since smoothers always alter the low freqencies to some extent.

The choice of smoothers when using a defect correction scheme is different than in regular multigrid. Of course we want the fastest smoothing rate possible, but in addition, we do not want to disturb the low frequencies, which are to be handled solely on the coarser grids. This rules out such sophisticated smoothers as incomplete LU-decomposition and block decomposition. In fact, the more we couple the unknowns across space (even by line relaxation, say) the more the low frequencies are going to be affected. This was confirmed through the solution of test problems using different smoothers. Thus one of the simplest smoothers of all, red-black Gauss-Seidel, is seen to be suitable for these problems. We wish to smooth each level enough to reduce the high frequency errors appreciably (say by 0.25–0.5) but not so much that the corrected low freqencies are degraded. In practice, $\nu = 2$ Gauss-Seidel sweeps were found to be appropriate. In the case of solving systems of equations as in (2.1), we solved for all the unknowns at a point simultaneously. Although this had the same smoothing rate as solving for each unknown in turn, it gave enhanced stability on the coarser grids.

2.4 Memory and work requirements.

Consider a system of 2 equations to be solved on an $N \times N$ grid. We must store the unknowns and the two right hand sides, F^k and $\tilde{F}^k$, on each grid. However, on the finest grid, $\tilde{F}^{M-1} = F^{M-1}$, so $\tilde{F}^{M-1}$ need not be stored. In the case of homogeneous

equations (such as the unforced Navier-Stokes equations), $F^{M-1} = 0$ and need not be stored either. All the relaxations are done in place and need no extra storage. The total memory requirement is therefore

$$2 + 6(\frac{1}{4} + \frac{1}{16} + \frac{1}{64} + \ldots)N^2 = 4N^2. \tag{2.19}$$

In practice, to keep our implementation flexible we stored F^{M-1} and the defect $F^k - L^k u^k$, so we actually used $6N^2$ locations. By way of comparison, even the simplest ILU smoother needs an extra $14N^2$ locations to do its elimination.

A work unit is defined as the computational effort to relax the fine grid once, and is commonly used to describe the work done by the total multigrid algorithm, although it ignores differences due to using different smoothers. Apart from smoothing, the computational overhead (one fine grid defect, two coarse grid defects, and four intergrid transfers) is about two work units. The total work for one FAS iteration (assuming sufficient levels that the work to solve the equations on level 0 is negligible) is therefore

$$(\nu_1 + 2)(1 + \frac{\gamma}{4} + \frac{\gamma^2}{16} + \ldots) = \frac{\nu_1 + 2}{1 - \gamma/4} \text{ work units} \tag{2.20}$$

or $2(\nu_1 + 2)$ in the case of W-cycles ($\gamma = 2$). In FMG multigrid, we perform, say, m FAS iterations on each level before progressing to the next finest level: the work is therefore

$$2(\nu_1 + 2)m(1 + \frac{1}{4} + \frac{1}{16} + \ldots) = \frac{8}{3}(\nu_1 + 2)m \text{ work units.} \tag{2.21}$$

Typically, $\nu_1 = 2$ and $m = 4$, giving the total work as 43 work units; but with point smoothers, one work unit is very fast. For example, in the computations done in Chapter 3 on a 384×320 grid with 246,000 unknowns, one work unit took seven seconds on a DEC 3100 workstation.

2.5 Testing.

We report here on the results of applying our multigrid program to two different problems: firstly, a linear convection-diffusion equation, to demonstrate the accuracy

of the defect correction technique, and secondly, the Navier-Stokes equations in a situation in which an accurate solution is already known.

The first situation is sketched in Figure 2.1a. This problem was considered by de Zeeuw and van Asselt (1985). Dirichlet data are specified on $y = 0$ on the left, and convected along circles centered on the origin. The problem is to convect the solution accurately without introducing excess diffusion.

$$\begin{aligned} 10^{-3}\nabla^2 u &= y(1-x^2)u_x - x(1-y^2)u_y \quad \text{on } [-1,1]\times[0,1], \\ u(x,0) &= 1+\tanh(10+20x), \quad -1 \le x \le 0, \\ \frac{\partial u}{\partial n} &= 0 \quad \text{on rest of boundary} \end{aligned} \tag{2.19}$$

First, an "exact" solution u_e was obtained by solving the standard $O(h^2)$ discretization on a 128×64 grid, by using 4 ILU relaxation sweeps applied to the upwind-corrected equations on the finest grid, and double-discretization on all coarser grids. This solution was compared to that obtained by two other methods: u_1, using the double-discretization method described above, and u_2, using a single-discretization method in which artificial viscosity is added in the smoothing steps, but not removed; i.e., $\tilde{L}$ was used throughout. In all cases the coarsest grid was 8×4, and nonisotropic artificial viscosity as in (2.15) was used with $\beta = 0.5$ on the two finest grids and $\beta = 1$ on all others. For both u_1 and u_2, the error reduction per iteration, although slightly worse on the finer grids, was always in the range 0.3–0.5. Four W cycles were performed.

In Table 2.1 we have given the mean and maximum errors for the two algorithms and estimated the order of accuracy as a power of the grid spacing. Of course, u_2 is only $O(h)$ because viscosity proportional to h has been added; but in u_1, the same viscosity has been removed by defect correction, and, as expected, it is $O(h^2)$ accurate.

The second test is the driven cavity problem, in which the Navier-Stokes equations are solved in $[0,1] \times [0,1]$, with $u = 1$ on the top edge and $\mathbf{u}.\mathbf{n} = 0$ on the rest of the boundary. The flow is sketched in Figure 2.1b. We consider this problem because

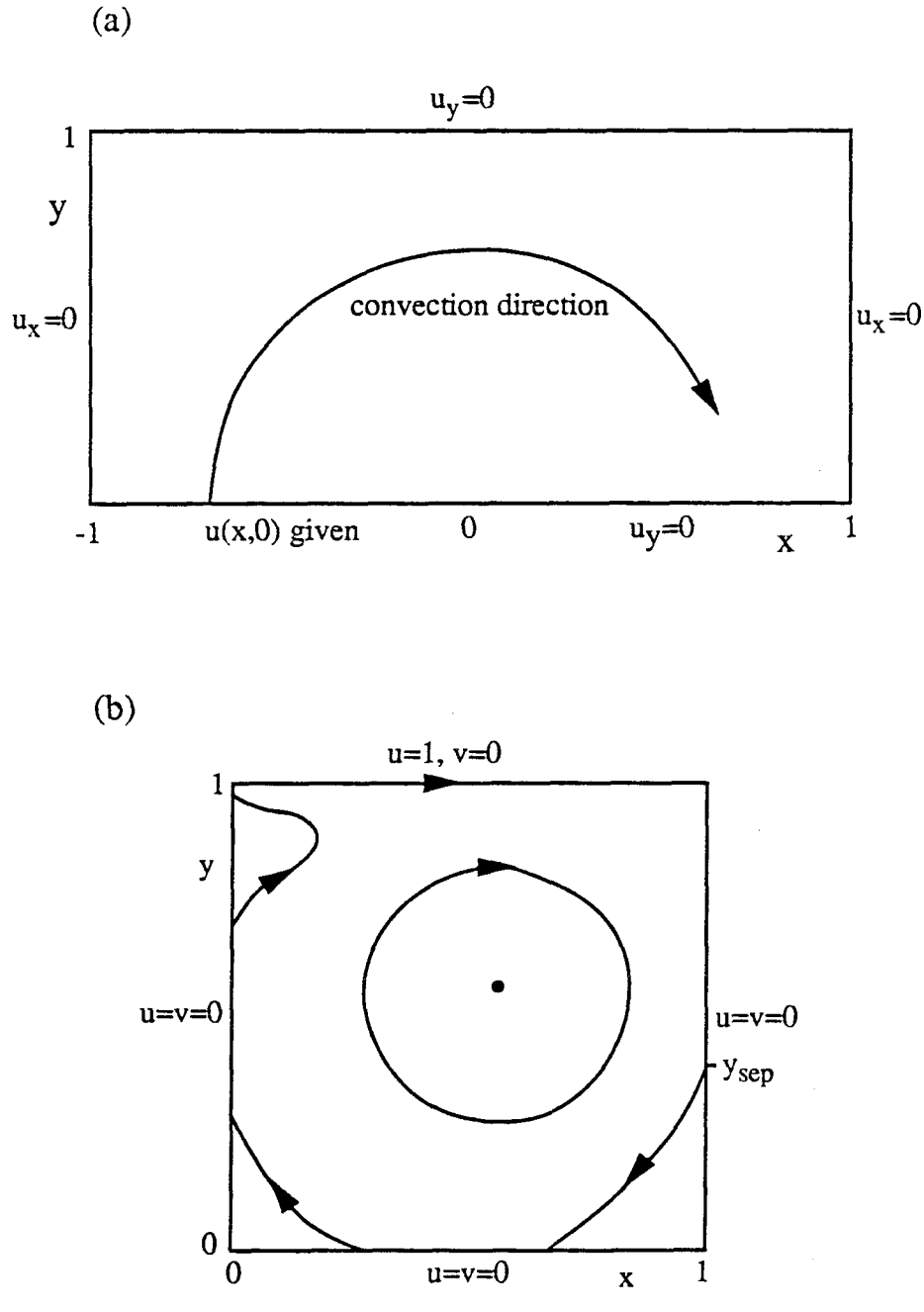

Figure 2.1 Two test problems

(a) linear convection-diffusion equation; (b) the driven cavity.

Table 2.1 Defect correction applied to a convection-diffusion equation

Grid	$\|u_1 - u_e\|_2$	$\|u_1 - u_e\|_\infty$	$\|u_2 - u_e\|_1$	$\|u_2 - u_e\|_\infty$
32×16	0.0767	0.2707	0.1387	0.5455
64×32	0.0237	0.0998	0.0757	0.3142
128×64	0.0037	0.0175	0.0304	0.1336
Order	2.18	1.98	1.09	1.01

highly accurate solutions have already been found by Schreiber and Keller (1983). They solved the equations to $O(h^2)$ using Newton's method and continued in the Reynolds number, on fine grids. Here we take Re=400, and solve the problem using relatively coarse grids to check accuracy. The boundary conditions are evaluated using a Woods expansion as explained in §3.3.

We found that $\beta = 0.5$, the smallest permissible value for linear stability of the relaxations, was no longer stable when used on the Navier-Stokes equations. Instead we used $\beta = 0.6$ on the two finest grids and $\beta = 1$ on the others. Six iterations were necessary for convergence below truncation errors (this was checked later by doing more iterations). The results for N=32, 48, and 64 are shown in table 2.2, where the accuracy on those coarse grids is compared with the Schreiber and Keller solution which is Richardson-extrapolated from N=100 and N=141. Here ψ and ω are the values of the stream function and vorticity at the center of the main vortex, defined as the extremum of ψ. e_ψ and e_ω are their respective errors. y_{sep} is the point of separation of the secondary eddy in the lower right corner (this could only be estimated from Schreiber and Keller's plot).

Table 2.2 Defect correction applied to the driven cavity problem

N	$-\psi$	e_ψ	$-\omega$	e_ω	y_{sep}
"exact"	0.11399		2.2898		~ 0.33
32	0.09872	0.0153	2.1707	0.119	0.346
48	0.10649	0.0075	2.2032	0.089	0.336
64	0.10993	0.0041	2.2393	0.050	0.327
64,$O(h^2)$		0.0050		0.042	

Although the h dependence is somewhat irregular, since the position of the center of the vortex can be located only up to $O(h)$, the accuracy is clearly comparable to an

exact solution of the $O(h^2)$ equations. In the last line of Table 2.2, the error in that solution has been estimated from Schreiber and Keller's results on two finer grids.

In addition, a run with N=96 gave $y_{\text{sep}} = 0.3271$, so it can be seen that the solutions with smaller N locate it correctly to within about $\frac{1}{2}h$ (except for N=64, which is accidentally accurate).

In conclusion, we are confident that the solution shift is negligible compared to the basic discretization error, and that our solution is in fact $O(h^2)$ accurate. All that remains is to determine the *actual* accuracy, which is best done by examining sensitive features of the solution (such as wall vorticity) to see how they depend on h. In the following chapter we present extensive convergence and accuracy tests for our main computations.

Chapter 3

Separated corner flow

3.1 Introduction.

In 1973, L.G. Leal studied the eddy formed when a straining field (given by the stream function $\psi = -xy$) impinges on a flat plate, lying on the x-axis from -1 to 1 (see Figure 1.1). This flow is simpler than others that have been examined at high Reynolds numbers, but retains many features of interest, such as a separating boundary layer, a reattaching shear layer, and an eddy. In addition, it is especially amenable to accurate numerical calculations, for several reasons:

1. The eddy size does not appear to grow without limit as the Reynolds number tends to infinity, so the problem can be solved in a fairly small domain.
2. Downstream of the eddy, the converging flow helps the vorticity diffuse across the axis of symmetry. Apart from a narrow vortical wake, no sophisticated boundary conditions are required to keep the computational domain small, in contrast to such cases as uniform flow past a bluff body, or even channel flow over a step.
3. The geometry permits a simple conformal map that concentrates grid points near the leading edge, where the boundary layer separates.

Leal obtained numerical results up to a Reynolds number of 400, based on a reference velocity of 1 and the plate semilength, 1. He was able to establish that the flow was regular through separation, with no sign of the Goldstein singularity emerging, but all the eddies appeared to be fully viscous. Our calculations show that the transition to inviscid dynamics takes place over the range of Reynolds numbers 1000–3000.

By extending the calculation to Re=5000, extensive comparisons of the behavior of the boundary layer near separation with triple deck theory are possible. In addition, the transition to a largely inviscid eddy is seen: the eddy is pushed downstream

and a region of constant vorticity develops. For $Re \geq 2255$, secondary separation occurs, complicating the theoretical picture considerably and invalidating a one-eddy Batchelor flow as the infinite Reynolds number limit.

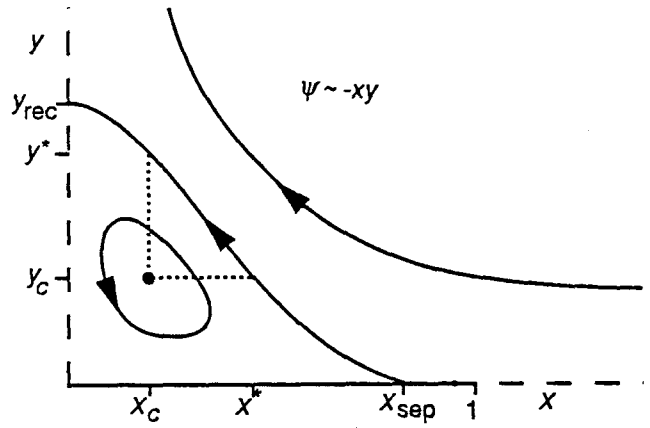

Figure 3.1 Local flow geometry

3.2 The physical problem and the equations of motion.

The flow geometry is sketched in Figure 1.1, and the quadrant in which we solve the equations in Figure 3.1. The flow is completely specified by the plate, the lines of symmetry on the axes, and the uniform strain in the far field. In the absence of the plate, $\psi = -xy$ is an exact solution of the Navier-Stokes equations with velocity $u = -x$, $v = 0$ on the x-axis. Superficially, this problem is similar to the problem solved by Howarth (1938), of the evolution of a boundary layer placed in a linearly decelerated free stream, which shows separation at $x = 0.88$. Although there would be no separation without deceleration in the free stream, the velocity outside the boundary layer and the separating streamline are strongly coupled and cannot be considered in isolation. Indeed, the skin friction ahead of separation turns out to show no resemblance to Howarth's solution.

We use the stream function–vorticity representation of the flow, in which the velocities are related to the stream function ψ by $u = \psi_y$, $v = -\psi_x$ and the vorticity ω is defined by $\omega = v_x - u_y$. Nondimensionalizing lengths by the position of the

leading edge, 1, and velocities by the undisturbed velocity at the leading edge, 1, the Navier-Stokes equations for incompressible, steady flow are

$$\begin{aligned} \nabla^2\psi &= -\omega, \\ \nabla^2\omega &= Re(\psi_y\omega_x - \psi_x\omega_y), \end{aligned} \tag{3.1}$$

where the Reynolds number $Re = 1/\nu$ and ν is the kinematic viscosity. Transforming to elliptical cylindrical coordinates with $x = \cosh\xi\cos\eta$, $y = \sinh\xi\sin\eta$, these become

$$\begin{aligned} \nabla^2\psi &= -J(\xi,\eta)\omega, \\ \nabla^2\omega &= Re(\psi_\eta\omega_\xi - \psi_\xi\omega_\eta), \end{aligned} \tag{3.2}$$

where $J(\xi,\eta) = \frac{1}{2}(\cosh 2\xi - \cos 2\eta)$ is the Jacobian of the transformation and now $\nabla^2 = \partial_{\xi\xi} + \partial_{\eta\eta}$. The quarter-plane $x \geq 0$, $y \geq 0$ maps to the semi-infinite strip $\xi \geq 0$, $0 \leq \eta \leq \frac{\pi}{2}$, with the plate at $0 \leq x \leq 1$, $y = 0$ mapping to the η axis ($\xi = 0$, $0 \leq \eta \leq \frac{\pi}{2}$).

The boundary conditions must be expressed in stream function-vorticity form and transformed to the new coordinates. Let $\mathbf{n}$ be a vector normal to a boundary. The x- and y-axes are streamlines so we have $\psi = 0$ there. The symmetry condition (shown as dashed lines in Figure 3.1) $\nabla\mathbf{u}.\mathbf{n}$ is easily rewritten as $\omega = 0$. The no-slip condition at the plate, $\mathbf{u} = \mathbf{0}$, becomes $psi_{\mathbf{n}} = 0$, or $\psi_y = 0$ here, which transforms to $\psi_\xi = 0$.

The boundary conditions in the computational coordinates are

$$\psi \to -xy = -\frac{1}{4}\sinh 2\xi \sin 2\eta, \quad \omega \to 0 \qquad \text{as } \xi \to \infty, \tag{3.3a}$$

$$\psi_\xi(0,\eta) = \psi(0,\eta) = 0 \qquad \text{for } 0 \leq \eta \leq \frac{\pi}{2}, \tag{3.3b}$$

$$\psi(\xi,0) = \psi(\xi,\pi/2) = \omega(\xi,0) = \omega(\xi,\pi/2) = 0 \qquad \text{for } \xi > 0. \tag{3.3c}$$

The flow in the computational coordinates is sketched in Figure 3.2.

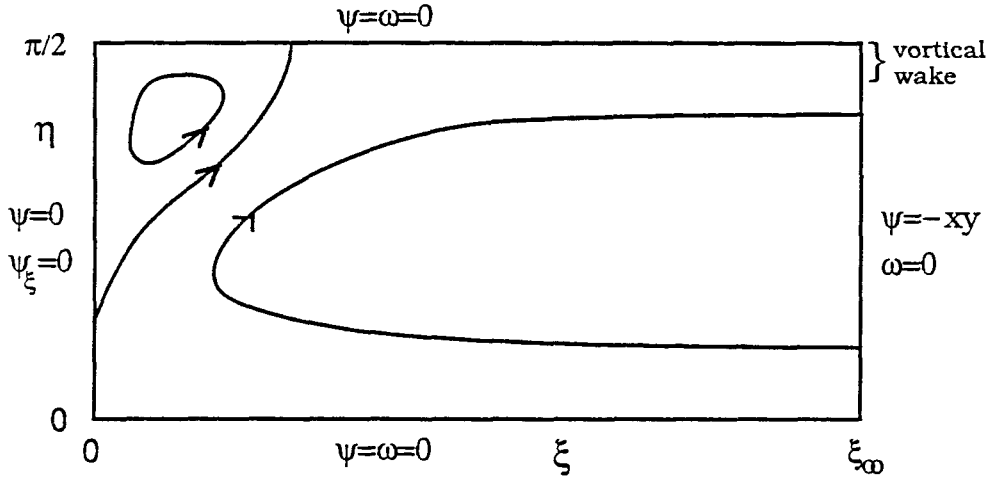

Figure 3.2 Flow in transformed coordinates

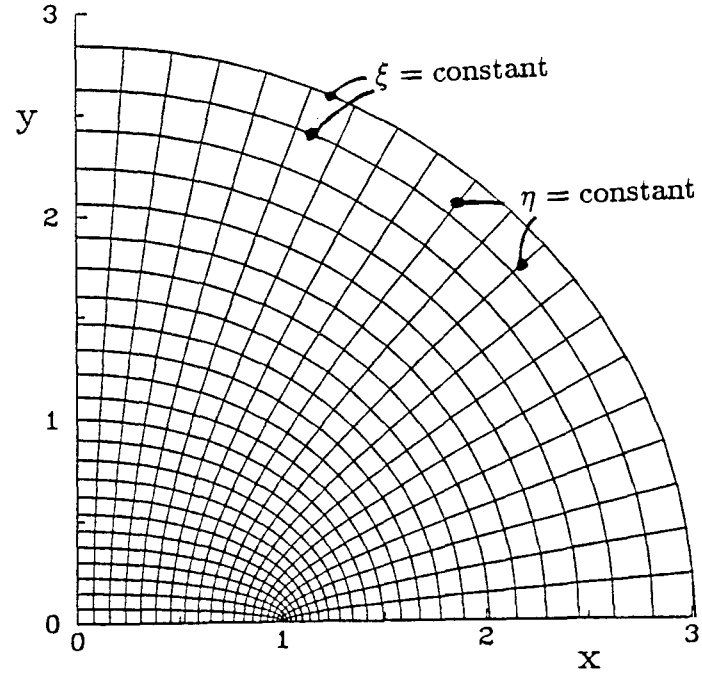

Figure 3.3 Computational grid

The third coarsest grid (24 x 20) is shown in the original coordinates. Here $\xi_\infty = 1.767$ and $y_\infty = 2.84$.

3.3 Treatment of the boundary conditions.

One of the coarser computational domains is shown in Figure 3.3. Let h be the grid spacing in the ξ direction, and k in the η direction. Because of the coordinate mapping, the grid spacing on the plate near the leading edge is $\Delta x \sim k^2/2$. This concentrates grid points in the region we are interested in, and also reduces the spatial effect of errors caused by the leading edge singularity. Notice that the actual singular point, $\xi = \eta = 0$, is never used in the relaxations.

The no-slip boundary condition $\psi_\xi = 0$ was transformed using the expansion of Woods, in which the surface vorticity is written as a function of the adjacent stream function and vorticity. The Taylor expansions of ψ and ω with respect to ξ are written out at $\xi = 0$, and the first three derivatives of ψ eliminated using the boundary conditions and (3.2). This gives

$$J(0,\eta)\omega_0 = -\frac{3}{h^2}\psi_1 - \frac{1}{2}J(h,\eta)\omega_1 + O(h^2), \tag{3.4}$$

where $\omega_j = \omega(jh,\eta)$. In some problems, a drawback of this method is that it destroys the expansion of the truncation error in powers of h^2 (useful in Richardson extrapolation) which is obtained using an $O(h)$ approximation for the surface vorticity. However, in solving model problems, (3.4) was found to be much more accurate than other expansions at modest values of h. Also, the defect correction process will introduce new errors of order h^2 and every higher order.

Over most of the domain, the far field boundary condition can be approximated by setting $\psi = -\frac{1}{4}\sinh 2\xi \sin 2\eta$ and $\omega = 0$ at $\xi = \xi_\infty$. A more accurate condition can be found by setting $\omega = 0$ and solving $\nabla^2\psi = 0$ in $[\xi_\infty, \infty) \times [0, \pi/2]$, leading to a relationship between ψ and ψ_ξ at $\xi = \xi_\infty$; however, the grid stretching at large ξ makes it easy to check the effect of the finite domain. In §3.4.2 we show that it is negligible, so that asymptotic boundary conditions are not required.

Close to the y-axis a wake persists, and the vorticity is *not* exponentially small. The form of this vortical wake can be found as follows. If we assume that the flow

in the wake is relatively undisturbed by the vorticity close to the x-axis, then the vorticity transport equation

$$u\omega_x + v\omega_y = \nu\nabla^2\omega \tag{3.5}$$

can be approximated in the straining field $u = -x$, $v = y$ by

$$-x\omega_x + y\omega_y = \nu\omega_{xx}, \tag{3.6}$$

with boundary conditions

$$\omega(0, y) = 0, \qquad w \to 0 \text{ exponentially as } x \to \infty. \tag{3.7}$$

We seek a similarity form for ω, say $\omega = y^\beta g(z)$, where $z = xy^\gamma$. Substituting in (3.6) leads to

$$-zg' + \beta g + \gamma zg' = \nu y^{2\gamma} g'', \tag{3.8}$$

so we take $\gamma = 0$ for similarity. In this flow the outward diffusion of the vorticity is just balanced by the inward compression of the flow.

This equation can be solved exactly by transforming it into the parabolic cylinder equation. However, it turns out that only one solution is both positive and decays exponentially as $x \to \infty$ (negative wake vorticity is not expected in this problem); this solution has $\beta = -2$ and

$$\omega = ay^{-2} g(x/\sqrt{\nu}), \quad g(w) = we^{-w^2/2}, \tag{3.9}$$

where the constant a, a measure of the strength of the wake, is supplied by the whole flow and cannot be locally determined.

The correction to the far field stream function $\psi = -xy$ is found to be $O(\nu y^{-2})$, and can be safely ignored. The corrections to the velocities are $O(\nu^{1/2})$, justifying our initial approximation (3.6). The small size of the wake, about $3\sqrt{\nu}$, and its fairly rapid decay in y help the process of finding this flow.

Equation (3.9) cannot be imposed as a Dirichlet condition because the wake strength a is unknown. A simple boundary condition that retains the structure of the wake is

$$\omega(\xi_\infty, \eta) = \left(\frac{y_{\xi_\infty - h}}{y_{\xi_\infty}}\right)^2 \omega(\xi_\infty - h, \eta) \tag{3.10}$$

for $x < 4\sqrt{\nu}$, and $\omega = 0$ elsewhere. This works because the wake is resolved only on the finest grids, and on these grids near the y-axis, x is almost constant from one grid point to the next. Interpolation to constant x is not necessary.

3.4 Numerical solution of the equations.

The equations (3.2), together with boundary conditions (3.3), (3.4), and (3.10), are now in the general form (2.1) considered in Chapter 2, and are to be solved in a rectangular domain. We generally used the standard full multigrid algorithm with W-cycles.

An extension was made to the interpolation operator (I) used for incorporating coarse grid corrections to the fine grid to improve convergence for this problem. For points not adjacent to the wall $\xi = 0$, bilinear interpolation was sufficient. However, $\psi \sim \xi^2$ near the wall, and this behavior must be preserved by interpolations. Linear interpolation is $O(h^2)$ accurate, which translates into an $O(1)$ error in the wall vorticity on application of the boundary condition (3.4). The simplest way to avoid this is to use the interpolation operator

$$(I\psi^{2h})(h,\eta) = \psi^{2h}(2h,\eta)/4 \tag{3.11}$$

in the ξ direction and linear interpolation in the η direction. Higher order interpolations at the wall and bicubic interpolation of the corrections everywhere were experimented with but were found to give worse convergence at high Reynolds numbers, presumably because the corrections in the defect correction method are not sufficiently smooth. It is also correct to use (3.11) when the boundary condition is $\psi_\xi = g(\eta)$, because only the corrections in ψ are interpolated; the linear part of ψ, $\xi g(\eta)$, does not change.

Secondly, the vorticity is singular at the origin, and the interpolations should take this into account. Bilinear interpolation at the point (h,k) would use the value of the vorticity at $(0,0)$, which is not defined. Instead, we use interpolations that preserve

the form of the singularity. Writing the Carrier-Lin (1948) leading edge singularity in our coordinates,

$$\tilde{\omega} = \frac{\eta^2 + \xi^2}{\eta}\omega \tag{3.12}$$

is nonsingular at the origin. At the point $(h, 2k)$ we interpolate linearly from two adjacent $\tilde{\omega}$ values. On $\eta = 0$, $\tilde{\omega}$ is not defined, so for values at (h, k) and $(2h, k)$ we just use the values on $\eta = 2k$. Finally, (3.12) is used to get interpolated values for ω.

3.4.1 Multigrid convergence.

The coarsest grid was always 6×5, i.e., $N = 5$ points on the plate. Collective Gauss-Seidel-Newton relaxations were used with both unknowns being updated simultaneously at a point. The grid points were scanned in red-black order. Here we consider the convergence of the multigrid iterations in a specific case: $Re = 1000$ with $N = 80$ points on the plate. The cell Reynolds number in this case is typical of all our runs. We cannot test convergence by looking at the defect, because it does not go to zero under the defect correction scheme. Nor do we know the solution ahead of time. Instead, we monitor a particular flow quantity from iteration to iteration. $\Omega = \int_0^1 \omega\, dx = \int_0^{\pi/2} \omega \sin\eta\, d\eta$ is used, which is sensitive because of the high order boundary conditions used, and because the negative vorticity in the eddy region partially cancels the square-root singularity near the leading edge. The behavior of Ω^n on the finest grid at the end of each multigrid iteration n was used as a convergence test throughout our work.

Table 3.1 gives the convergence history over 12 iterations, with $\nu = 2$ smoothing steps, $\beta = 0.6$ on the two finest grids and $\beta = 1$ on all others. Convergence is not monotonic but is quite rapid overall, with about the same rate in the initial and final iterations. We use $(\Omega^n - \Omega^{n-1})/(\Omega^{n-1} - \Omega^{n-2})$ as an estimate of the convergence rate, or error reduction per iteration. In this case, the asymptotic convergence rate is about 0.30, and the mean rate over all twelve iterations is 0.33.

To show that this algorithm generates "full multigrid" convergence similar to that found in linear problems, Table 3.2 gives the reconnection point y_{rec} after different

Table 3.1 Multigrid convergence

FMG is used with initial guess 0 on the coarsest grid; results are given for $n = 12$ iterations on the finest grid.

n	Ω^n	$\Omega^n - \Omega^{n-1}$
1	5.705991	
2	5.083912	0.622
3	5.245922	0.162
4	5.226105	0.020
5	5.268903	0.043
6	5.278613	0.010
7	5.282886	0.0043
8	5.283479	0.00059
9	5.283669	0.00019
10	5.283793	0.00012
11	5.283814	0.00002
12	5.283827	0.00001

Asymptotic convergence rate ~ 0.30

Table 3.2 FMG convergence

This measures the error after completing n FMG iterations. The error e^n is the difference between y_{rec} and the value, 0.6153, found with $N = 160$. We also give a common FMG error norm, $\theta^n = e^n/e^\infty$.

n	y_{rec}	e^n	θ^n
2	0.5891	0.0262	1.42
3	0.5940	0.0213	1.16
4	0.5954	0.0199	1.08
10	0.5969	0.0184	

numbers of FMG iterations. Even after two iterations, the distance from the actual value is much less than the discretization error. If we count the computational overhead (one fine grid defect, two coarse grid defects, and four interpolations and restrictions) as two work units (this is borne out by actual timings), we therefore require a minimum of 11 work units to solve the equations to within truncation errors. In practice, of course, we usually solve the equations much more accurately, both to ensure that we have algebraic convergence, and to allow later Richardson extrapolation.

Table 3.3 gives the dependence of the convergence rate on the number of smooth-

Table 3.3 Convergence rates

Here ν is the number of smoothing sweeps applied per level; k is the number of fine grids on which $\beta = 0.6$ (on coarser grids, $\beta = 1$); and "Rate" is the mean error reduction in Ω per iteration, averaged over twelve iterations.

ν	k	Rate	e^n	θ^n
1	2	0.50	0.0154	
2	2	0.33	0.0184	
3	2	0.35	0.0206	
1 ILU	2	0.21	0.0281	
(2.5 times slower)				
2	0	0.42	0.0247	1.20
2	1	0.39	0.0202	1.34
2	2	0.33	0.0184	1.16
2	3	0.44	0.0168	1.40

ing sweeps ν applied on each level and the corresponding error in y_{rec}. Increasing ν from 2 to 3 shows no improvement because at that point convergence is limited by the defect correction iterations, not by the smoothing of high frequency errors. The errors e^n increase with ν because each smoothing with respect to $\widetilde{F}$ moves the unknowns farther from the solution with respect to F. Clearly, $\nu = 1$ and $\nu = 2$ are both good choices; we usually used $\nu = 2$ except at the highest Reynolds numbers.

For $Re \leq 3000$ the algorithm was found to be very robust: convergence and accuracy properties hardly depended on the method's parameters. Table 3.4 gives results for four different runs using an artificial viscosity parameter of $\beta = 0.6$ on the 1, 2 and 3 finest grids, respectively, and for $\beta = 1$ everywhere. (We cannot use 0.6 on all grids because then the relaxations do not smooth the errors on the coarsest grid, slowing or destroying convergence.) Setting $\beta = 0.6$ on the two finest grids only is the best choice, and this was usually used. This behavior stands in contrast to the results of de Zeeuw and van Asselt (1985), who found that a small coefficient should be used only on the finest grid for fastest convergence when a defect correction scheme is not used.

For finer grids and larger Reynolds numbers the convergence rates are the same, up to a point. Eventually we began to experience convergence problems with full

multigrid. This was related to the existence of spurious solutions to the discrete equations close to the "real" solution. In these solutions the secondary eddy was either larger and much stronger than expected, or it collapsed. After checking convergence to these solutions carefully, it was eventually realized that their vorticity wiggles on the plate and their large errors in the flux test (described below) indicated that they were spurious. These solutions were avoided by using trivial continuation in the Reynolds number, starting multigrid on the finest level with a solution obtained at a lower Reynolds number. Large steps in Reynolds number (e.g., 1000) could be used. In addition, for $Re > 3000$, we obtained better results using $\beta = 0.6$ on the finest grid only (stabilizing the second-finest grid relaxations), with $\nu = 1$ relaxation (decreasing the defect correction error).

At $Re = 5000$, $N = 320$, the method converges at the same rate initially (averaging 0.53 with one smoothing step for the first 6 iterations) but slows down in the asymptotic stage (rate about 0.74). This degraded asymptotic convergence rapidly gets worse, and at $Re = 6000$ the method no longer converges. (The first few iterations still show convergence to something close to a solution, but $\int_0^1 \omega$ behaves erratically after that, changing about 0.05 from iteration to iteration.) This problem is believed to be linked to the growing differences between $\tilde{F}^h$ and F, and between $\tilde{F}^h$ and $\tilde{F}^{2h}$, as the cell Reynolds number increases, for this flow field. This behavior is not seen in the linear convection-diffusion equation tested in Chapter 2, which can be solved with the same convergence rate for any Reynolds number. Thus we do not expect a linear analysis to pinpoint the problem. We return to this question later.

3.4.2 Accuracy of the solutions.

The errors due to the finite domain are extremely small. At $Re = 1000$, $N = 160$, moving the outer boundary from $\xi_\infty = 1.767$ ($y_\infty = 2.84$) to $\xi_\infty = 2.356$ ($y_\infty = 5.23$) changed the reconnection point y_{rec} by only 10^{-4}—2% of the discretization error. Imposing the free stream condition downstream at $\xi_\infty = 1.767$ led to larger errors of about 0.0012, or 25% of the discretization error. Accordingly, all runs used the wake boundary condition (3.10) with $\xi_\infty = 1.767$ for $Re > 1000$.

Originally, we examined the dependence of the solutions on h by repeatedly doubling N and checking that they were in fact second order accurate. This confirmed that the errors were $O(h^2)$ throughout the flow field. Some tests are shown in Figure 3.4. In all cases the errors increased faster than the Reynolds number—this is shown in Table 3.5. Since $\nabla\omega = O(Re)$ in the boundary layers, and the vorticity transport equation has terms proportional to $Re\nabla\omega$, we might expect discretization errors of order $O(Re^2)$; fortunately, it appears that these thin layers do not excessively pollute the rest of the solution. However, instead of presenting these results, we concentrate here on a test that checks a known property of incompressible steady flows against the numerical solutions.

The Kirchoff circulation theorem for steady flow (Batchelor 1967) states that

$$\nu \int_C \nabla \times \omega \, d\mathbf{s} = 0, \tag{3.13}$$

where the integral is taken around any closed streamline; that is, the total flux of vorticity through any material surface is zero. This conservation law is clearly not built into our numerical solution, so we can use (3.13) to see how well we have satisfied the Navier-Stokes equations globally. We take C to be the contour surrounding the main eddy:

$$C = \bigcup \Big\{ \begin{array}{l} (x,0) : 0 \le x \le x_{\text{sep}} \\ (x,y) : \psi(x,y) = 0 \text{ separating streamline} \\ (0,y) : y_{\text{rec}} \ge y \ge 0 \end{array} \Big\} \tag{3.14}$$

This includes the entire shear layer, which is where the greatest errors are expected. The entire contour is contained in boundary layers of thickness $O(Re^{-1/2})$ (except at its corners), so we expect the local flux of vorticity to be $O(Re)$—hence the normalizing ν in (3.13).

The integral (3.13) must be evaluated carefully. We use the trapezoidal rule for the integration, taking care to retain second order accuracy at the corners, where the flux is large. The position of $\psi = 0$ and the flux there are found using linear

interpolation from adjacent points. There is one convenient point: because (ξ, η) is a conformal map of (x, y),

$$-\omega_y \, dx + \omega_x \, dy = -\omega_\eta \, d\xi + \omega_\xi \, d\eta, \tag{3.15}$$

so it is straightforward to compute the integrand in the computational coordinates. The mapping functions enter only when the flux itself is computed.

In this flow, the flux of vorticity is directed into the eddy on the separating streamline, and out of the eddy on $x = 0$ and $y = 0$. We estimate the relative error as the total flux divided by the absolute flux in or out of the eddy. It would be useful to compare our errors with those in other numerical Navier-Stokes solutions, but tests such as (3.13) do not seem to have been applied in the past, to our knowledge.

Table 3.4 Accuracy of vorticity and total vorticity flux

Here the "fine grid" has N points on the plate, and the "coarse grid" $N/2$. The vorticity is evaluated at the center of the Richardson-extrapolated eddy. The flux error is defined in the text.

Re	N	Vorticity at center			Flux error		
		Coarse	Fine	Richardson	Coarse	Fine	Richardson
150	160	0.670	0.667	0.666	0.006	0.004	
400	160	1.313	1.293	1.285	0.013	0.004	
1000	160	1.616	1.583	1.572	0.058	0.012	0.007
2000	320	1.818	1.777	1.762	0.048	0.008	0.007
3000	320	1.979	1.912	1.889	0.091	0.019	0.007
4000	320	2.105	2.014	1.984	0.148	0.034	0.006
5000	320	2.200	2.105	2.074	0.193	0.045	0.007

Table 3.4 gives the flux errors for various mesh sizes and Reynolds numbers. Although (3.13) might accidentally be very small in a particular case, the consistent results indicate that this is not happening. The relative error appears to be slightly better than $O(h^2)$, because the discretization error of the integral itself is decreasing.

One great advantage of solving $F^h u = r$ directly using Newton's method is that the accuracy can be improved by eliminating the discretization error term by term by Richardson extrapolation. This is usually done at a single point, after checking that the error is indeed of the required order. With our approach, if the same solution

parameters are used with a smaller N (e.g., $\beta = 0.6$ on the two finest grids), the discretization error of the defect-corrected solutions will have the same coefficients of h^2. This term can then be eliminated, leaving an error of $O(h^3)$. In addition, we have a *post facto* check that the extrapolation was valid by computing the new flux balance. This new flux error is also shown in Table 3.4, and in every case it is about the same size as the discretization error in the integral (3.13), which is only computed to $O(h^2)$. Also note that the integrand is the third derivative of the stream function, evaluated in a thin boundary layer, and is expected to have much larger errors than those in ψ and ω.

Unfortunately, those derivatives are precisely the quantities required in studying the flow: for example,

$$(\nabla \times \omega)(x,0) = \omega_y(x,0) = Re\, p_x(x,0) \tag{3.16}$$

is the (scaled) adverse pressure gradient experienced by the main boundary layer. So, although extrapolation at the coarse grid points is sufficient for the gross flow, for greatest accuracy at the boundaries we need to evaluate quantities like (3.16) on the finest grid. In this case, we first interpolate the $N/2$ solution to the fine grid using bicubic interpolation, introducing new $O(h^4)$ errors—smaller than those of the final solution. Figure 3.4 compares different methods of computing this quantity at Re=5000.

Finally, we have estimated the relative error in our final solution at $Re = 5000$, as follows. First the dependence of the errors on Reynolds number was estimated for each quantity. Then the coefficient of h^3 in the Richardson-extrapolated solutions was found at $Re = 400$ (from $N = 40$, $N = 80$, and $N = 160$ calculations), and this result extrapolated to $Re = 5000$ using the observed power law dependence. (Thus, we are assuming that this dependence is the same at both second and third order). The relative errors are given in Table 3.5 and are mostly a few tenths of a percent. The error is larger in $\max p_x$ because the maximum occurs near the leading edge singularity, where the finite differences break down.

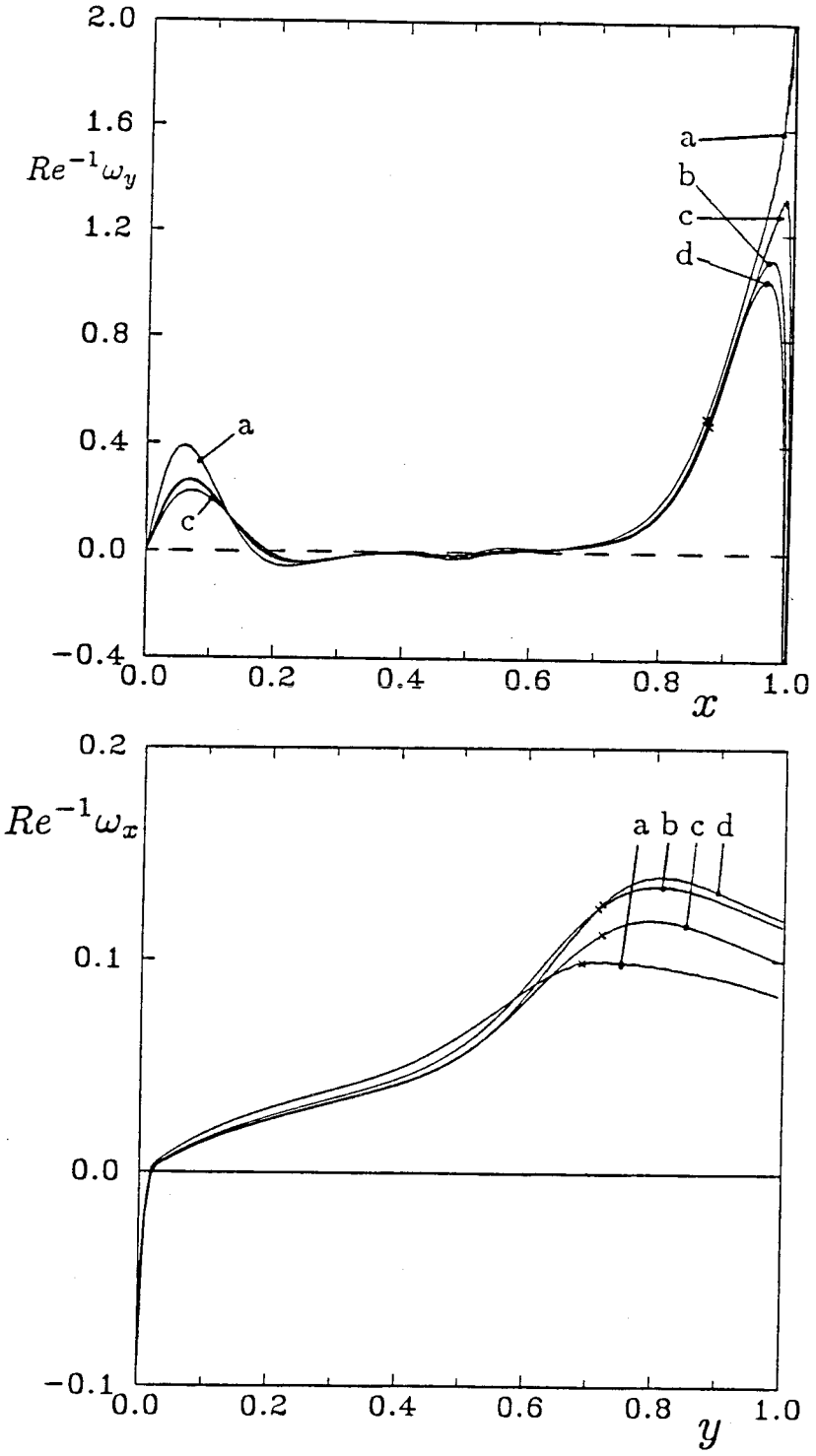

Figure 3.4 Accuracy of boundary quantities

The flux of vorticity is shown at $y = 0$ (top) and $x = 0$ (bottom) for $Re = 5000$, calculated using third order finite differences. (a) N=160 points on the plate; (b) N=320; (c) Richardson extrapolation evaluated on coarse grid; (d) Richardson extrapolation evaluated on fine grid.

Table 3.5 Relative errors in final $Re = 5000$ solution

Quantity	Re dependence	Relative error
$1 - x_{\text{sep}}$	$Re^{0.5}$	5×10^{-4}
ω_c	$Re^{1.3}$	1.5×10^{-3}
$\tau_x(x_{\text{sep}})$	$Re^{1.0}$	1.3×10^{-3}
$p_x(x_{\text{sep}})$	$Re^{1.4}$	3×10^{-3}
$\max p_x$	$Re^{1.4}$	3×10^{-2}

3.5 The basic flow structure.

3.5.1 Previous results due to L.G. Leal.

Leal (1973) used $Re = 2/\nu$, so his nominal Reynolds number is twice ours. His Reynolds numbers have been rewritten here using $Re = 1/\nu$ in an attempt to avoid confusion.

He found that after the boundary layer has separated, the eddy shape rapidly assumed a fairly constant form as the Reynolds number increased. The large amount of positive vorticity generated at the leading edge was convected increasingly efficiently downstream, forming a shear layer. By studying the shear stress through separation, Leal found no sign of the Goldstein singularity. He noted that the Howarth result ($x_{\text{sep}} = 0.88$) is irrelevant when the external flow is modified by the eddy, and performed a boundary layer calculation using the observed pressure distribution on the plate, which gave similar results to the full Navier-Stokes solution; however, this pressure was still changing at $Re = 400$, the highest Reynolds number he considered.

By comparing the shape of the eddy to sample viscous and inviscid eddies, he noted that all the eddies were largely viscous and that there was no hint of any transition, in contrast with the classical work of Batchelor. In fact, as we shall see, the inviscid transition was just about to take place, and already at $Re = 400$ there is evidence that vorticity is starting to be convected around the eddy.

3.5.2 The inviscid transition.

Table 3.6 gives global properties of the flows for $150 \leq Re \leq 5000$. Contour plots of the stream function and vorticity are shown in Figure 3.5. All results were

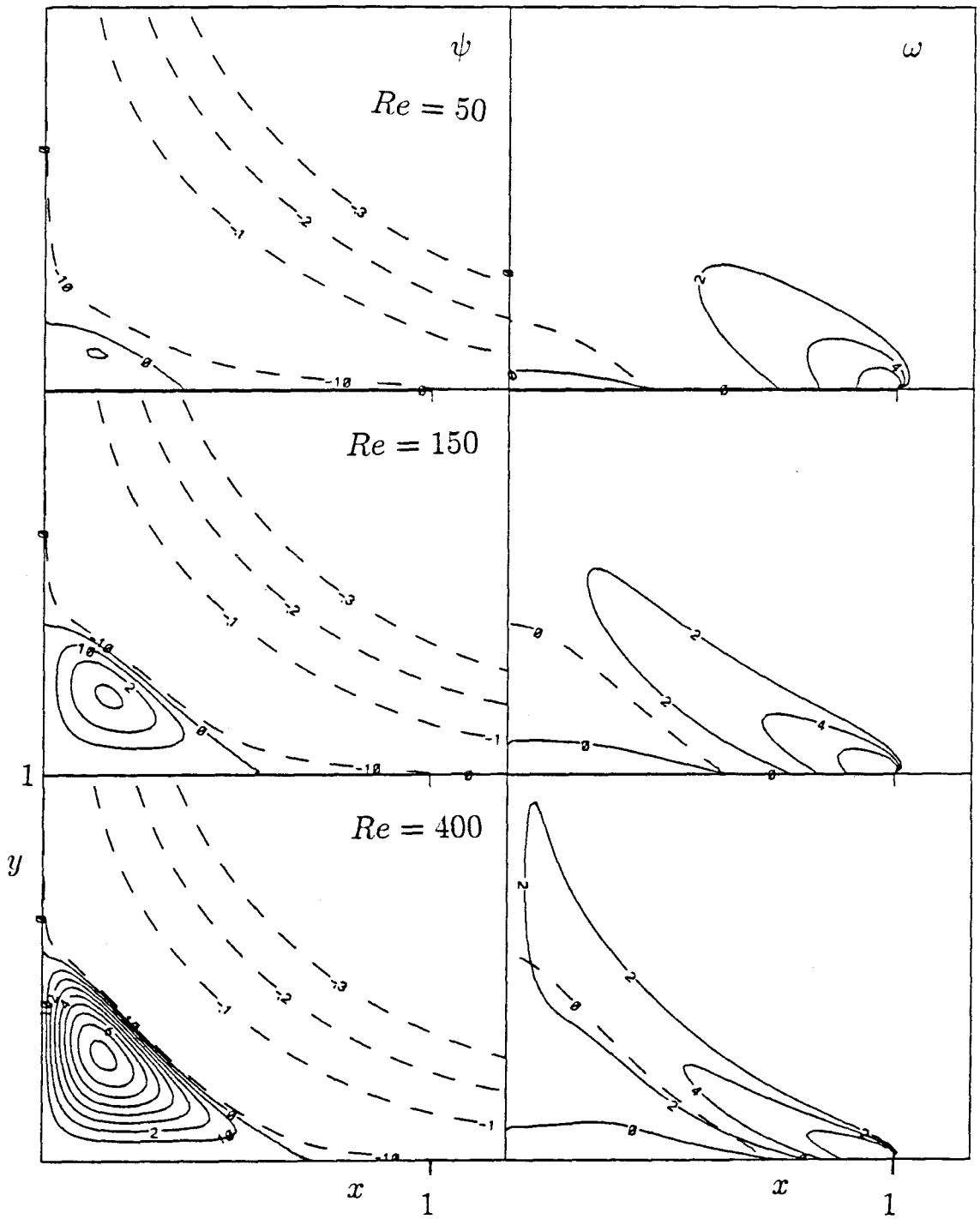

Figure 3.5 Streamline and vorticity contours

The interior contour levels are $\psi = -0.001(0.001)0.004$, then $\delta\psi = 0.004$; and $\delta\omega = 2$. The wiggles near the leading edge are caused by linear interpolation in the plotting routine. The vorticity contours, on the right, also include the separating streamline as a dashed line.

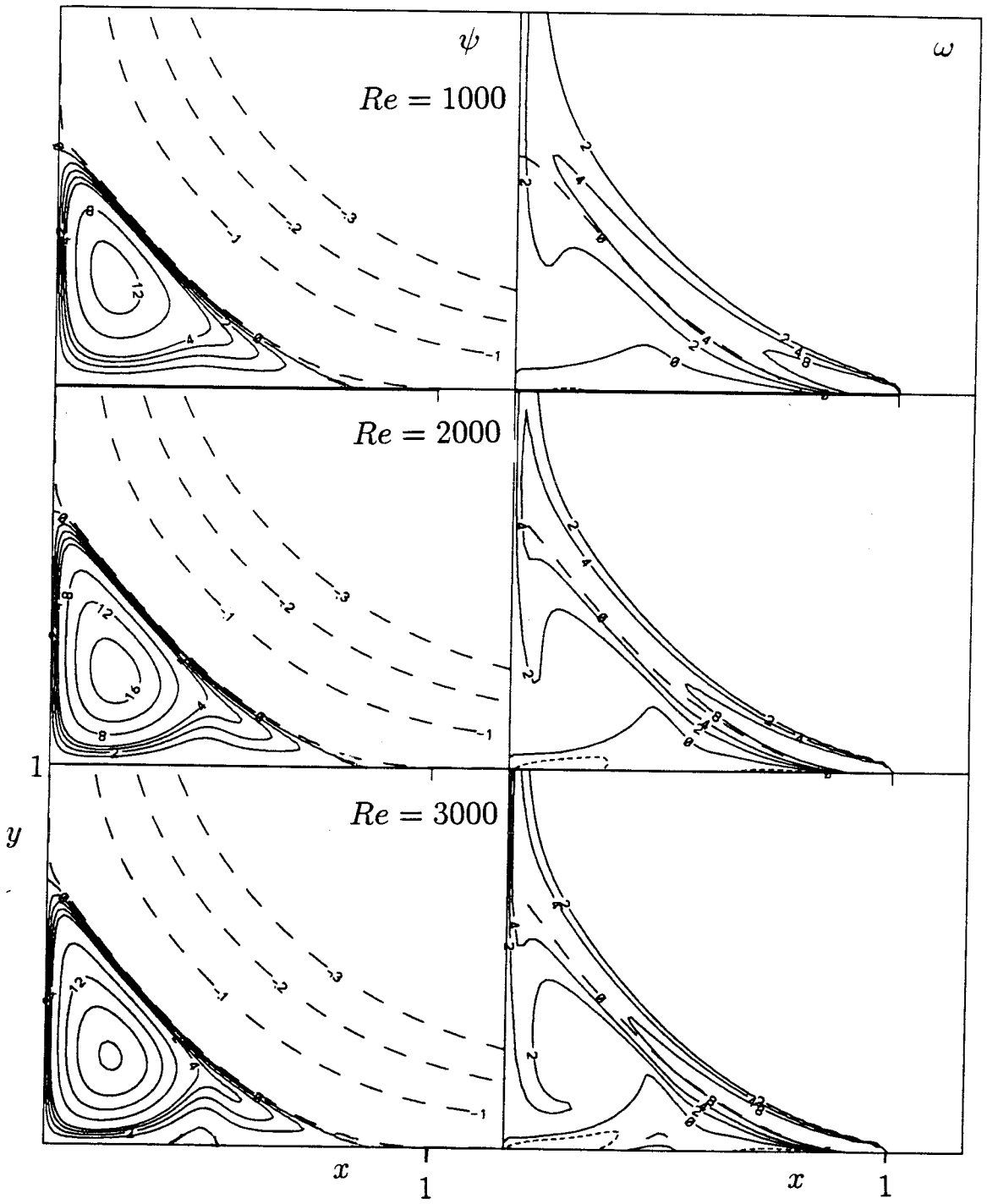
ψ
ω
$Re = 1000$
$Re = 2000$
$Re = 3000$
1
y
x
1
x
1

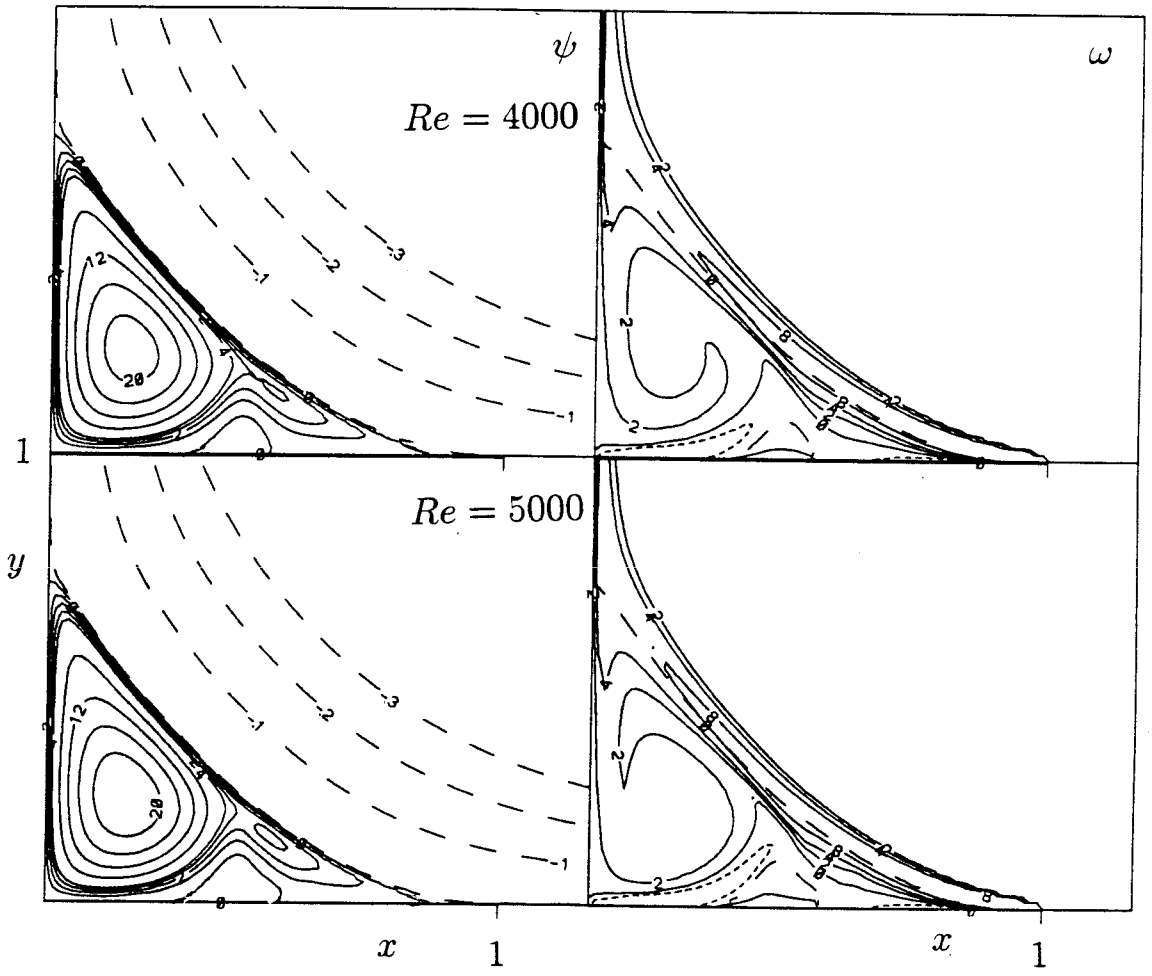
ψ
ω
$Re = 4000$
$Re = 5000$
1
y
x
1
x
1

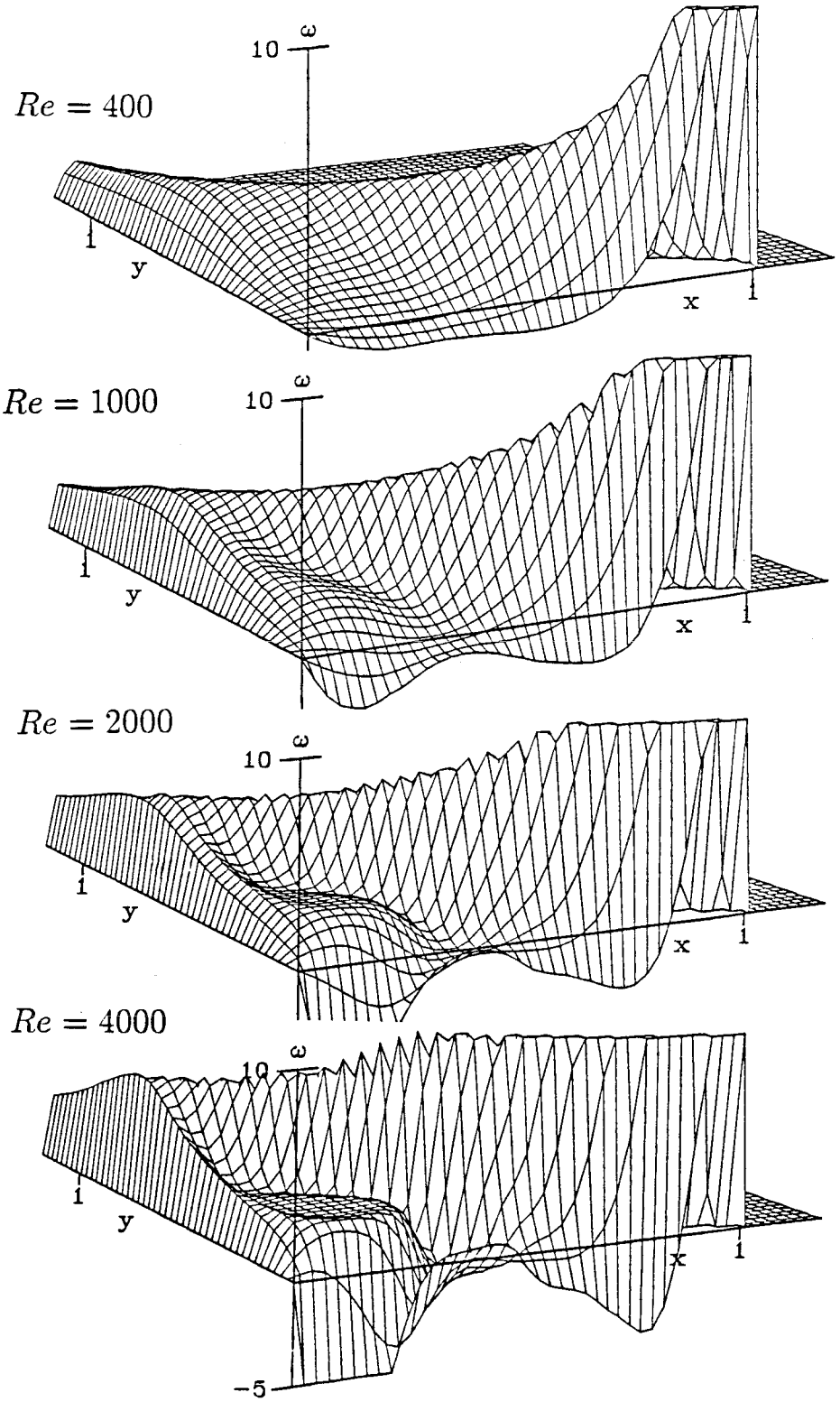

Figure 3.6 Perspective view of vorticity

Here ω has been truncated to lie in the range $-5 < \omega < 10$.

Table 3.6 Primary eddy characteristics

These are the values found by Richardson extrapolation. ψ_c and ω_c are values at the center of the main eddy. See Figure 3.1 for more information.

Re	x_{sep}	y_{rec}	$y_{\text{rec}}/x_{\text{sep}}$	x_c	y_c	ψ_c	ω_c	$x_c/x^*, y_c/y^*$
150	0.5696	0.3902	0.685	0.1695	0.2010	0.0031	0.667	(0.53,0.62)
Leal	*.58*	*.39*	*.68*			*0.003*		*(.52,.63)*
400	0.6968	0.5321	0.764	0.1524	0.2766	0.0083	1.285	(0.47,0.62)
Leal	*.70*	*.515*	*.735*			*.0072*		*(.52,.63)*
1000	0.7814	0.6191	0.792	0.1524	0.2766	0.0140	1.572	(0.41,0.55)
2000	0.8278	0.6678	0.807	0.1657	0.2337	0.0182	1.762	(0.39,0.48)
3000	0.8497	0.6908	0.813	0.1705	0.2289	0.0205	1.889	(0.38,0.45)
4000	0.8633	0.7069	0.819	0.1755	0.2287	0.0221	1.984	(0.40,0.46)
5000	0.8729	0.7165	0.821	0.1755	0.2287	0.0234	2.074	(0.39,0.45)

Table 3.7 Secondary eddy characteristics

Re	x_{sep}	x_{rec}	x_c	y_c	$10^4\psi_c$	ω_c
2250	~ 0.38				0	0
3000	0.3307	0.4556	0.4055	0.0295	−0.47	−0.347
4000	0.3052	0.4894	0.4239	0.0542	−2.96	−0.760
5000	0.2896	0.5126	0.4371	0.0497	−4.34	−0.733

calculated using Richardson extrapolation from the solutions found with N and $N/2$ grid points on the plate. For very small Reynolds numbers there is no reverse flow. At $Re = 25$ the flow separates from the plate, first at $x = 0$ but rapidly separating farther upstream as the Reynolds number increases. For $100 < Re < 1000$, the main global changes are the upstream motion of the separation point, the increasing aspect ratio due to increasingly efficient convection of the shear layer, and a rapid strengthening of the eddy. At the origin, a nearly uniform downward jet impinges on the plate; locally there is Heimenz flow. Because of the symmetry condition at $x = 0$, there is no possibility of a sequence of corner eddies (either because of boundary layer separation, as in the driven cavity, or viscous Moffat vortices, which are subdominant to Heimenz flow in this geometry).

We note that at finite Reynolds number the flow separates at a finite angle to the plate. Near separation (given by the point of zero skin friction), there is a Stokes region in which inertial forces are subdominant to viscous forces. The equation for

the stream function is then $\nabla^4\psi = 0$, and the solution which represents separation at an angle θ from a wall is

$$\psi = y^2(y\cos\theta - x\sin\theta), \tag{3.17}$$

where separation takes place at the origin. From this it is easy to show that the initial slope of the $\omega = 0$ contour is one-third of the slope of the separating streamline $\psi = 0$, which can be seen in Figure 3.5, and that that slope is

$$\tan\theta = \frac{3\omega_x(0,0)}{\omega_y(0,0)}. \tag{3.18}$$

Consideration of inertial forces shows that (3.17) is valid for $x < Re^{-1/3}$.

The quantities x_c/x^* and y_c/y^* give the relative position of the eddy center and characterize the structure of the eddy (see Figure 3.1). Table 3.6 shows that the eddy center moves first left and then down as the Reynolds number increases and remains fixed for $Re \geq 3000$. Leal computed two "reference" eddies, one viscous ($\nabla^4\psi = 0$) which had $x_c/x^* = (0.52, 0.63)$, and one inviscid ($\nabla^2\psi = -1$) which had $x_c/x^* = (0.40, 0.47)$. Comparing these values to the results in Table 3.6, we see that the structure of the eddy changes from viscous to inviscid as Re increases from 400 to 2000. Looking at Figure 3.6, this corresponds to the emergence of a region of almost constant vorticity.

The similarity of our Navier-Stokes flows to Leal's sample eddies is surprising, and suggests that other features (the flow near separation, the actual values of the vorticity, the formation of a secondary eddy) are less important than the relative magnitude of the viscous and convective terms.

With hindsight, it is easy to see why a Reynolds number of 400 is insufficient to see inviscid flow: the flat plate "brakes" the eddy, which has typical velocities $\bar{u} \sim \psi_c/y_c \sim .03$ or a local Reynolds number of about 12. At Re=2000, $\bar{u} \sim .08$, so the local Reynolds number is about 160, which is much more likely to show inviscid dynamics. Furthermore, a circular vortex patch with constant vorticity ω_0 has $\psi_c =$

$\frac{1}{4}\omega_0 y_c^2 \sim .028$ here, so we conjecture that the main part of the eddy has reached its asymptotic state.

Batchelor (1956) has shown that in a region of flow in which the streamlines remain closed as $Re \to \infty$ and do not pass through a singular region, the vorticity will tend to a constant. (In brief, at $Re = \infty$, vorticity is clearly constant *along* a closed streamline; the net flux of vorticity *across* it must always be zero; it only remains to show that the flux is actually zero everywhere.) As we have observed the rapid development of a region of constant vorticity, and as there is absolutely no sign of either of the two caveats mentioned above, we believe that the infinite Reynolds number limit of this flow does indeed follow the Prandtl-Batchelor model of constant vorticity regions separated by vortex sheets.

It is interesting that the level of vorticity in the plateau is still increasing slowly but almost linearly at $Re = 5000$. This is because the local Reynolds number in some parts of the boundary layers is much less than 5000, so that they have not yet reached their asymptotic state. But it does raise the question as to whether the level at $Re = \infty$ is substantially higher.

3.5.3 Secondary separation.

As Re increases, the local Reynolds number near the wall downstream increases rapidly, and a reverse boundary layer forms there. This is evident in the vorticity near the wall in Figure 3.5. In contrast to the smaller Reynolds numbers, at $Re = 1000$ the flow is almost stagnant behind the separation point. The reverse boundary layer has broadened significantly and the faster downstream fluid does not come back that far.

At $Re = 2255$ (determined with $N = 320$), the reverse boundary layer separates, first at $x = 0.38$, and a secondary eddy forms. This may be explained as follows. Let (x_c, y_c) be the center of the vortex. A Batchelor vortex with constant internal vorticity ω_0 will have a slip velocity at $y = 0$ which rises from zero at $x = 0$ to a maximum of about $\frac{1}{2}\omega_0 y_c$ at $x = x_c$ (by comparison with a circular vortex), and falls

to zero at $x = 1$, being $O\left(\omega_0(1-x)^{3/2}\right)$ near the cusp. If the viscosity ν is very small but not zero, boundary layers will develop to satisfy the extra boundary condition—in this case, a no-slip wall. Boundary layer integrations with applied external velocities show that initially accelerated boundary layers tend to separate almost immediately after the external velocity begins to decrease.

Characteristics of the secondary eddy are shown in Table 3.7. It grows fairly rapidly and its large-Re behavior can be guessed from the results in $3000 \leq Re \leq 5000$. Some fluid must always return from the main part of the eddy to the cusp, to supply the mass entrained by the shear layer. It appears, though, that as the secondary eddy grows, this return takes place in an $O(Re^{-1/2})$ shear layer next to the main, outgoing one. Interestingly, all the calculations show a third, weak center in this layer; possibly it disappears as $Re \to \infty$. Velocities are very small, about 0.03 , in the region between separation and the secondary reconnection, but it seems inevitable that a tertiary eddy will form there eventually. (A flattening of ω in this region is already evident at $Re = 5000$; see Figure 3.7.) The inviscid limit would thus consist of an infinite sequence of eddies behind the separation point, each one containing still finer structure. The rapidly decreasing velocities mean that the number of eddies will grow very slowly with the Reynolds number, probably logarithmically.

3.6 Asymptotic behavior at boundaries.

This will be discussed in detail in Chapter 5. As the Reynolds number increases, the separation point continues to move closer to the leading edge. The reconnection point also continues to increase, but the aspect ratio of the eddies levels off sharply once inviscid behavior has set in.

Figure 3.7 shows the vorticity at the wall (proportional to shear stress) divided by $Re^{1/2}$, the expected asymptotic growth for a boundary layer. Although the scaled value is roughly $O(1)$, the boundary layer is still developing at $Re = 5000$. Note that the incipient secondary separation is already hinted at at $Re = 400$: ω has a local maximum. The pressure gradient in the boundary layer (equal to the flux of vorticity

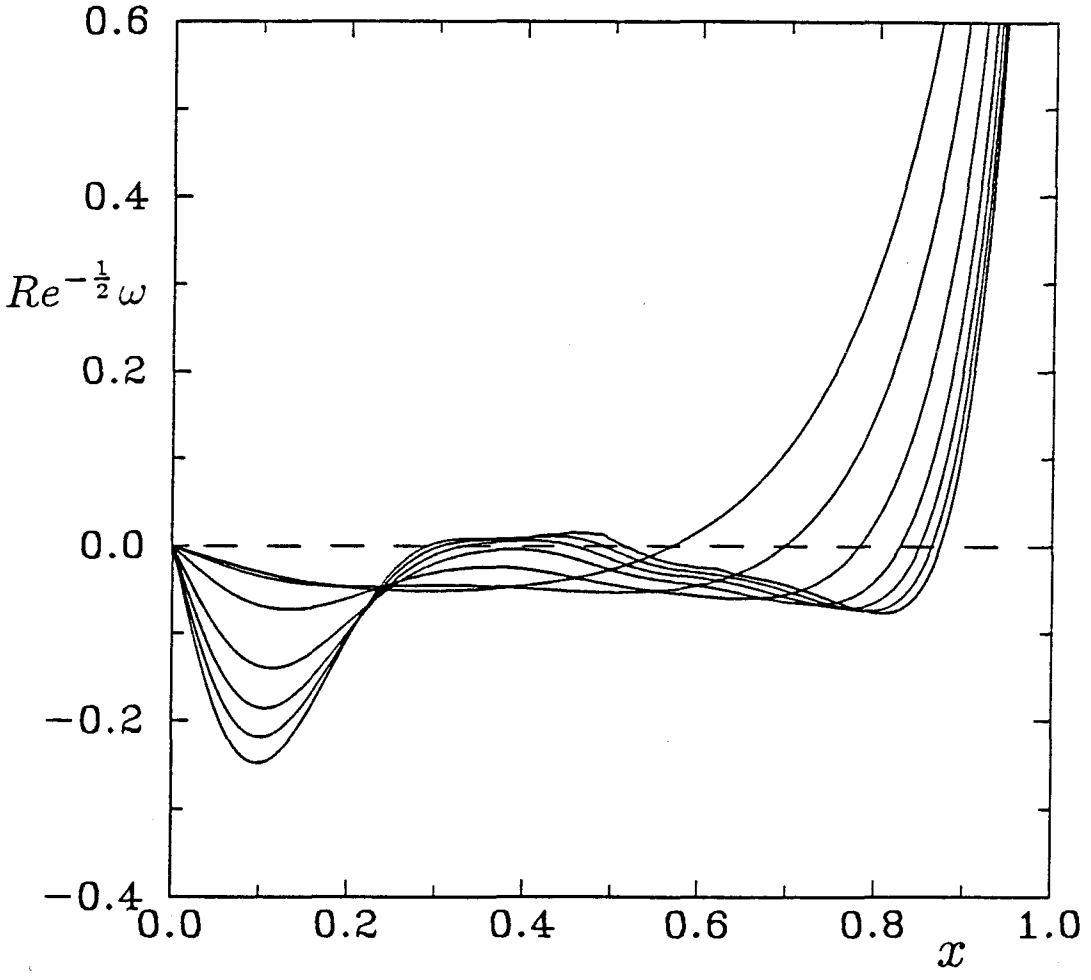

Figure 3.7 Wall vorticity

Here and in Figures 3.8, 3.9, and 3.10, results are given for Re = 150, 400, 1000, 2000, 3000, 4000 and 5000. Separation takes place at the point where $\omega = 0$, which moves to right (towards the leading edge) as Re increases.

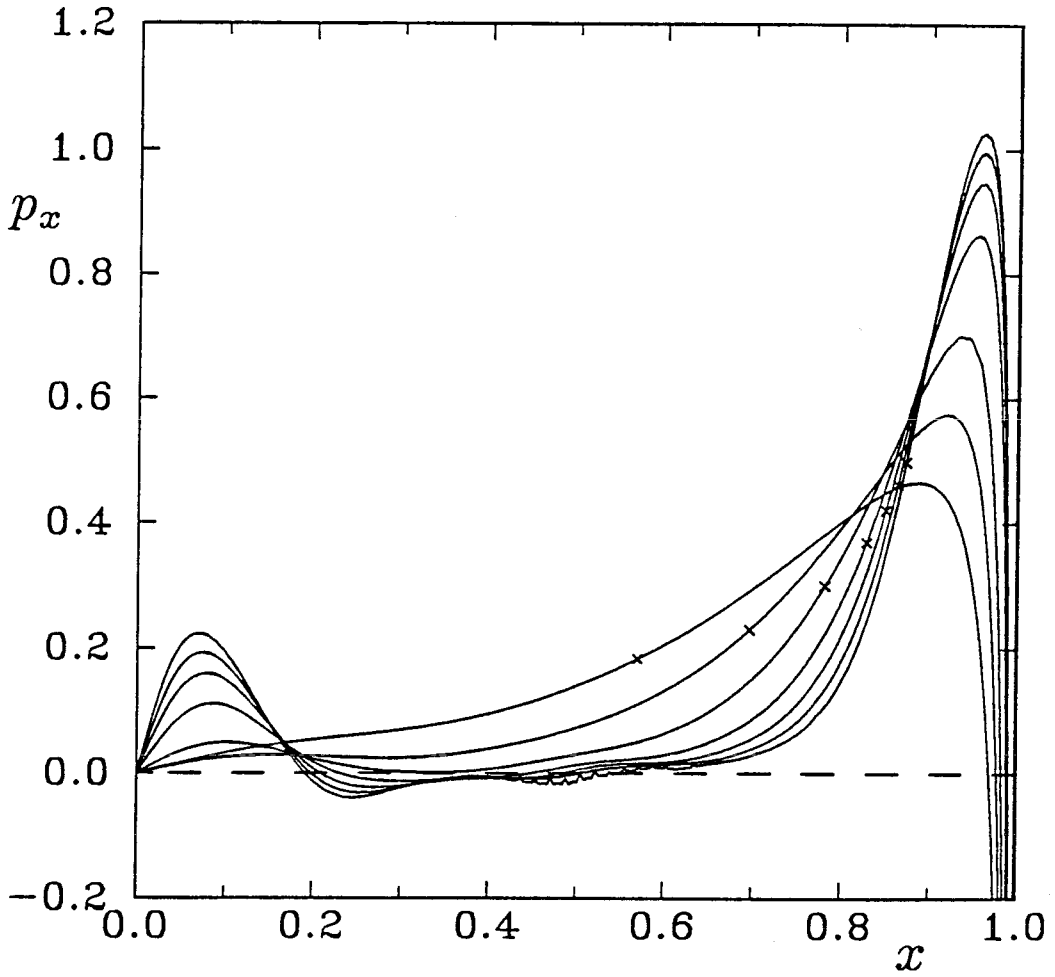

Figure 3.8 Wall pressure gradient

Computed as $\omega_y(x,0)/Re$ using third order finite differences. $\max p_x$ increases with Reynolds number. The wiggles at $Re = 5000$ are introduced by extrapolation using the $N = 160$ solution, which does not completely converge; the $N = 320$ solution is smooth. The sign has been changed so that a positive value represents an adverse pressure gradient near the leading edge. The separation point is marked ×.

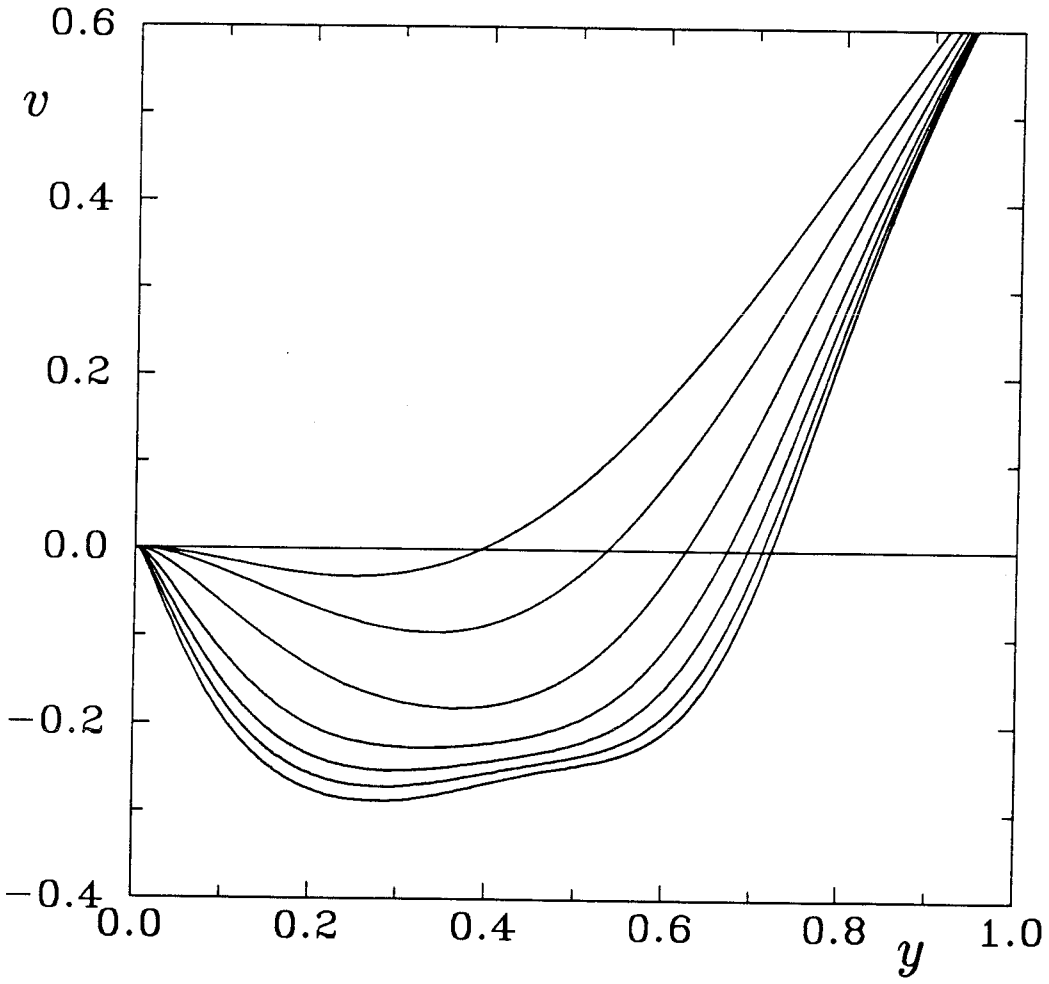

Figure 3.9 Vertical velocity at $x = 0$

Velocity decreases with increasing Reynolds number.

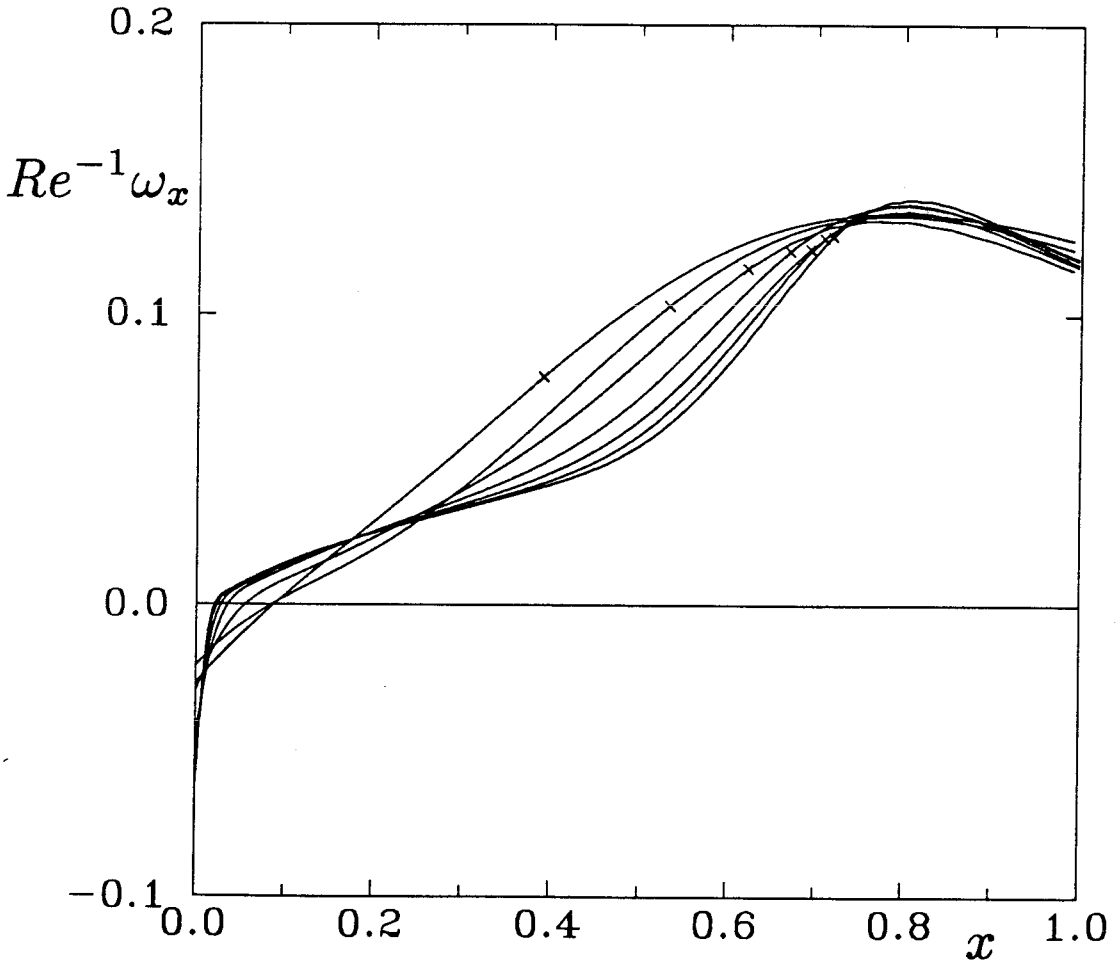

Figure 3.10 Flux of vorticity at $x = 0$

The reconnection point, which increases with increasing Reynolds number, is marked $\times$.

at the wall divided by Re) is shown in Figure 3.8. There is a Carrier-Lin singularity at the leading edge, followed by an adverse pressure gradient that increases slowly with Reynolds number, falling to near zero behind separation. Figure 3.9 shows the vertical velocity ($v = 0$ corresponding to reconnection), and 3.10 the scaled vorticity flux (or p_y) at $x = 0$. They are still changing at $Re = 5000$ because the shear layer has diffused considerably by the time it reaches the x-axis.

We note that Figures 3.9 and 3.10 are strongly supportive of a triple deck-like interaction as the smallest scale phenomenon at reconnection. The vertical velocity gradient v_y at separation is proportional to $Re^{0.31}$, and the scaled vorticity flux, to $Re^{0.06}$, both exponents being close to their triple deck values of 1/4 and 1/8, respectively. However, $y_{\rm rec}$ increases only slowly: if we assume that the inviscid flow reconnects at $y = 1$, then $1 - y_{\rm sep} \propto Re^{-0.175}$. This is believed to be due to a relatively large scale inviscid interaction caused by the shear layer, which rapidly broadens as it nears reconnection. A self-consistent asymptotic description of this process is still under construction.

3.7 Summary.

We have found accurate solutions to the Navier-Stokes equations for $Re \leq 5000$. For Re less than about 400, the corner eddies are fully viscous. In $1000 \leq Re \leq 3000$, their main part undergoes a rapid transition to inviscid character, and the Prandtl-Batchelor model of infinite Reynolds number flow is definitely correct in this case. However, the next stage, in which all the viscous layers reach an asymptotic state, will be considerably slower, especially near $x = 0$. Near separation, Figures 3.7 and 3.8 appear to indicate that separation is already in an asymptotic regime at $Re = 150$; we study this extensively in Chapter 5. At $Re = 2250$, the downstream reverse boundary layer separates, and we speculate that the inviscid limit contains an infinite sequence of eddies behind the separation point.

Batchelor (1967) includes a photo of an experiment in which a splitter plate is introduced in front of a stagnation point. We have reproduced it in Figure 3.11.

The main changes from our flow are that the free stream has uniform flow, rather than uniform strain, and that there is also a wall at $x = 0$, apparently extending to $y = 0.55$. Unfortunately the Reynolds number is not given.

Nevertheless, the similarity with our flows is striking. The flow in 3.11 appears to separate at $x = 0.81$, and the eddy center in the top eddy is at $x_c = 0.23$, $y_c = 0.13$—less than our value because of the different oncoming flow. Secondary separation occurs at $x = 0.33$. These values suggest that the Reynolds number is between 1000 and 2000. Notice, however, that there are two strong secondary eddies in $y > 0$ and several weaker ones, in contrast to our results. Because there is not exact symmetry between the two halves of the flow, we believe that these eddies are due to unsteadiness. There may well there exist time-periodic flows in which a sequence of secondary eddies appears at much smaller Reynolds numbers than in our steady flows.

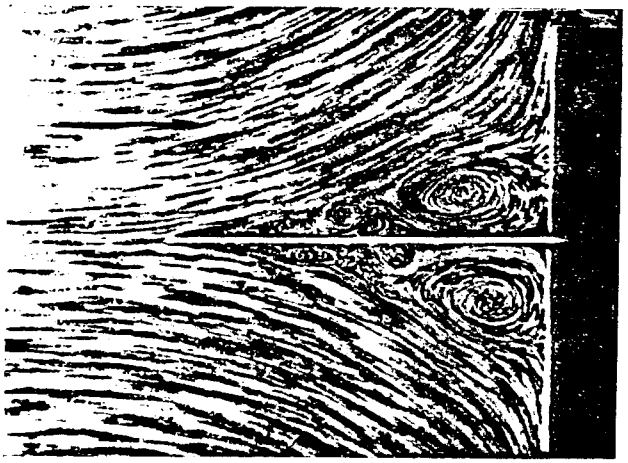

Figure 3.11 An experiment showing separated corner flow
Reproduced from Batchelor (1967), Plate 7.

Chapter 4

Viscous corner eddies and Batchelor flows

4.1 The Batchelor model of infinite Reynolds number flow.

Inviscid flows consisting of regions of constant vorticity separated by vortex sheets and possibly bounded by walls were first proposed by Batchelor (1956) as possible limits of viscous flows at infinite Reynolds number. Pressure is constant across a vortex sheet, and if the velocities on either side are q_+ and q_- then Bernoulli's theorem shows that the sheet strength $\gamma = q_+ - q_-$ obeys

$$\gamma(q_+ + q_-) = q^2 \tag{4.1}$$

with q a constant. For example, a corner flow can be found using Kirchoff's free streamline theory which consists of a stagnant corner separated from an external, irrotational flow by the line $x^{2/3} + y^{2/3} = 1$, on which $q_- = 0$ and $q_+ = 3/4$. (More details of this flow are given in §5.8.) The initial behavior of the dividing streamline, $y \sim ax^{3/2}$, is always present unless $q = 0$. The simplest example of a rotational Batchelor flow is the circular vortex with constant vorticity ω embedded in irrotational flow, in which the fluid has tangential velocity $\omega r/2$ at a distance r from the vortex's center.

A family of rotational corner flows was found by Moore, Saffman and Tanveer (1988) (henceforth referred to as MST), which had internal vorticity $0 < \omega < 6.11^+$. The corresponding flow separating at $x = L$, say, would have vorticity ω and would reconnect at $y = L$, since only symmetric eddies were found to exist. If such a flow is to be the limit of viscous flow as $Re \to \infty$, the viscous flow would presumably have a core of constant vorticity, with thin $O(Re^{-1/2})$ boundary layers near the walls to satisfy the extra boundary condition not present in inviscid flow, and with the vortex sheet being replaced by a shear layer with velocity jump γ. L and ω would then be determined by the wall boundary conditions.

The Navier-Stokes solutions of the previous section show a transition to a largely inviscid eddy that cannot, however, be an MST vortex. First, the aspect ratio of the eddies does not tend to 1, but seems to level off at about 0.8; only symmetric Batchelor vortices were found by MST. More important, the constant-vorticity core does not spread over the whole eddy, but stays downstream; upstream, secondary separation occurs.

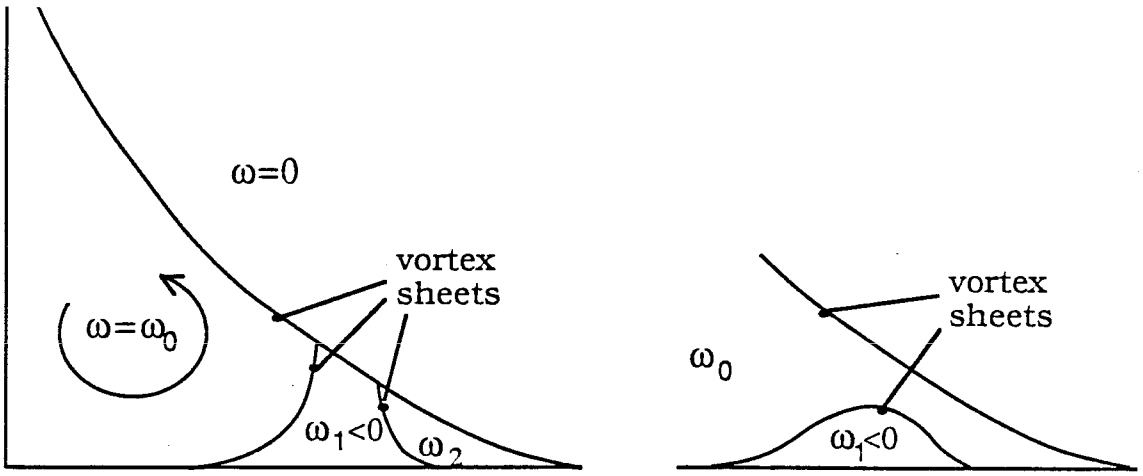

Figure 4.1 Two possible Batchelor flows with secondary separation
The results of Chapter 3 suggest the limiting flow on the left.

There are probably more inviscid solutions, consisting of several regions of constant vorticity, each bounded by a vortex sheet. Two possibilities are sketched in Figure 4.1. This would certainly break the symmetry of the 1-region family. However, there is no reason to suppose that tertiary separation is avoided either, which in principle can give rise to an infinite sequence of eddies in the cusp, as suggested by Messiter (1975). Since $u = o(1-x)$, the Reynolds number necessary to form each successive eddy would increase. This sequence could terminate if the velocity in the cusp decreased with increasing Reynolds number, but this is not indicated by the $Re = 5000$ results.

Despite these problems, the eddy shapes calculated in Chapter 3 *are* rather similar to the MST vortices. Figure 4.2 shows the separating streamline at $Re = 1000$ and

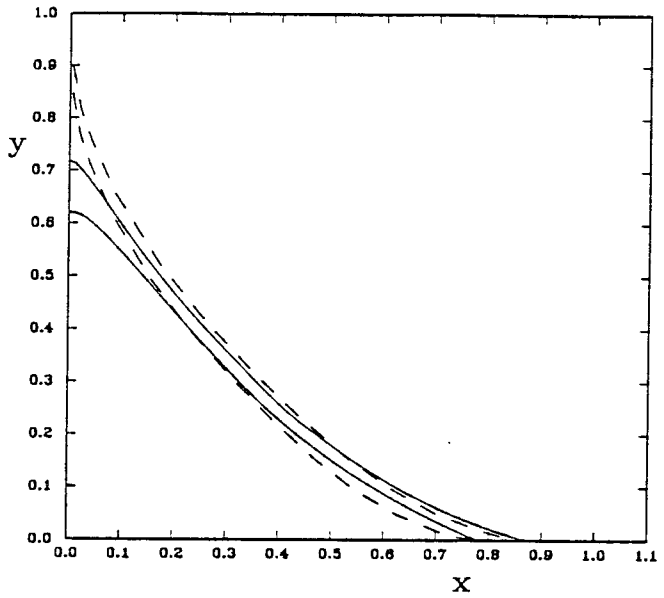

Figure 4.2 Separating streamlines in corner eddy

The inner solid line is the $\psi = 0$ streamline at $Re = 1000$, and the outer line is $\psi = 0$ at $Re = 5000$. Results taken from Chapter 3. The dashed lines are inviscid vortex sheet positions, as explained in the text.

5000, compared to the MST vortex with constant vorticity 2 separating at the same position as the viscous flow. At $Re = 1000$, the flow near separation is different, but at $Re = 5000$ the agreement is encouraging, and surprising, in view of the secondary separation—although the secondary eddy may interfere with the external flow as it continues to grow in strength. Certainly the difference is less than the thickness of the shear layer.

4.2 Single eddy flows with a moving wall.

The behavior of the flat plate problem suggests that to see the simplest Batchelor vortex it is necessary to prevent separation of the reverse boundary layer. One way to do this would be to apply suction at the wall. However, this would upset the mass balance, creating an unknown far field. A simpler way is to give the plate a positive horizontal velocity. Setting $u(x,0) = u_p$ gives $\psi_\xi = u_p \sin\eta$, which is implemented as (cf. (3.10))

$$J(0,\eta)\omega_0 = -\frac{3}{h^2}\psi_1 - \frac{1}{2}J(h,\eta)\omega_1 + \left(\frac{3}{h} + \frac{h}{2}\right)u_p \sin\eta. \tag{4.2}$$

The first flow computed was with $u_p = 0.2$ at $Re = 1000$, shown in Figures 4.3 and 4.5. The moving plate did indeed stop the boundary layer from widening excessively; furthermore, the "strength" of the eddy (the maximum value of the stream function) increased from 0.014 in the stationary plate case to 0.041, because of the velocity imparted to the eddy by the plate. The increased local Reynolds number in the eddy explains the more nearly inviscid flow: there is already a distinct plateau of vorticity with $\omega_0 \sim 2.5$. When $u_p > 0$ the streamline $\psi = 0$ clearly cannot contact the plate. One possibility is for a thin layer of reversed flow to remain near the plate for a short distance, but this does not turn out to be the case. (It may occur in the singular limit $u_p \to 0$.) Instead, there is a stagnation point a distance $O(\nu)$ ahead of the plate and the flow immediately separates. Because the external flow never comes in contact with the plate, it remains inviscid, and the dividing streamline behaves like $ax^{3/2}$. A graph of $y_{sep}^{2/3}$ is a straight line away from the stagnation point, and we find $a \sim 0.590$. The distance s from the origin to the shear layer along the line $y = x$ can be found approximately if its position is taken as the point of maximum vorticity. This gives $s = 0.54$. These values closely correspond to the MST vortex with $\omega_0 = 2.5$ (see Table 4.2).

Increasing the Reynolds number to 2000 and 4000 gave similar flows, shown in Figure 4.3, suggesting that secondary separation is definitely averted. ω_0 increased slowly, as shown in Table 4.3. It thus appears that one of the family of MST vortices is selected as the large Reynolds number limit, which one depending on the boundary conditions on the axes. The finite-Re solutions agree well with the corresponding MST vortex, with two exceptions:

1. The aspect ratios remain less than one. This is probably due to viscous action close to $x = 0$, because the dividing streamline follows the proposed vortex sheet closely until then. Note that at finite Reynolds numbers, the streamline must reconnect at right angles in a stagnation point, not in a cusp. Reconnection is discussed briefly in §3.7 and is the subject of ongoing research. We believe that it *is* possible for the cusp-shaped shear layer to reattach in an orderly fashion.

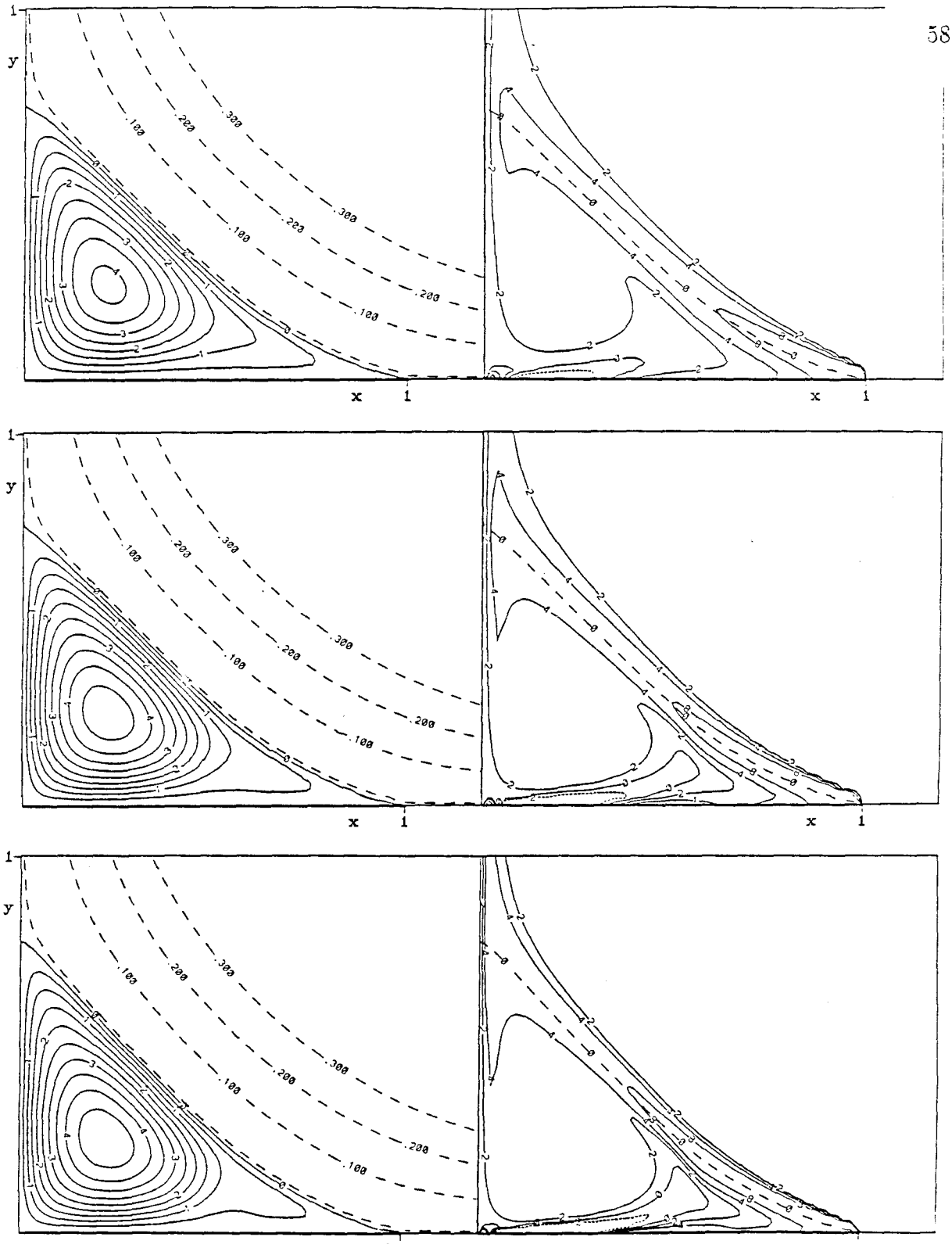

Figure 4.3 Streamline and vorticity contours

for $u(x,0) = 0.2$ and Re=1000, 2000 and 3000. The contour intervals are $\Delta\psi = .005$ and $\Delta\omega = 2$. Note the developing region of constant vorticity, and the boundary layer near $y = 0$. The wiggles near the leading edge are caused by interpolation in the plotting routine.

2. The constant vorticity region does not cover the whole eddy. The problem this time is not slow flow upstream—in fact, the flow is nearly inviscid in the cusp, as shown by the vorticity contours that follow the streamlines everywhere except near the wall. Instead, disturbances generated in the downstream boundary layer are swept away from the wall by the natural motion of the eddy.

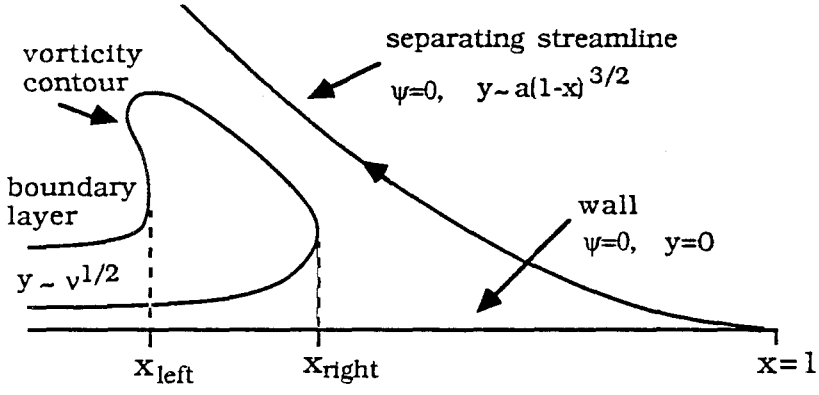

Figure 4.4 Viscous flow in the cusp

This effect can be estimated as follows. Consider the Batchelor flow with internal vorticity ω. The equation for the stream function in the cusp is approximately $\psi_{yy} = -w$, with $\psi = 0$ at $y = 0$ and at $y = y_{sep} = ax^{3/2}$, so

$$\psi = \frac{1}{2}\omega y(y_{sep} - y). \tag{4.3}$$

Thus the streamlines turn around as shown in Figure 4.4 when $u = 0$, or

$$x = \left(\frac{8\psi}{\omega a^2}\right)^{\frac{1}{3}}, \tag{4.4}$$

measuring distance from the leading edge. Now suppose that viscous effects do not greatly alter the flow field. Downstream, in the boundary layer, $\psi = u_p y + O(y^2)$ and $y = O(\nu^{1/2})$. So streamlines (or, equivalently, vorticity contours) originating in the boundary layer will turn around when $x = O(\nu^{1/6})$; the constant vorticity region will enter the cusp very slowly.

Of course, the disturbance from the boundary layer invalidates the original approximation, which is only correct downstream of the disturbance. Nevertheless, the

result seems to hold throughout the cusp. Table 4.1 shows the left and right turning points for the $\omega = 2$ contour at three Reynolds numbers; the dependence is about $Re^{-.135}$, close to that predicted. Evaluating the constants shows a disagreement of about 20%; evidently, the streamlines are not disturbed much by the boundary layer.

Table 4.1 Turning points of $\omega = 2$ contour

"ratio" is the distance at that value of Re divided by the distance at the next smallest Re; the distances are predicted to go like $Re^{-1/6}$.

Re	$1 - x_{left}$	ratio	$1 - x_{right}$	ratio	$\triangle \mathrm{Re}^{-1/6}$
1000	.609		.362		
2000	.553	.908	.337	.931	.891
3000	.531	.960	.311	.923	.935

Table 4.2 Properties of the Batchelor corner flow

Reproduced from MST. Here q is the jump in the square of the velocity across the sheet, s is the distance from the origin to the vortex sheet measured along $y = x$, and a is the constant in the initial sheet position $y = ax^{3/2}$.

ω	q	s	a
0.0	0.75	0.5	$(2/3)^{3/2}$
1.0	0.7464	0.5056	0.550
2.0	0.7344	0.5231	0.568
3.0	0.7099	0.5541	0.605
4.0	0.6619	0.6028	0.683
5.0	0.5598	0.6790	0.874
6.0	0.2255	0.8262	2.17
6.115	0		$y \sim x^{1/2}$

By altering the boundary condition on the plate, different members of the family of MST vortices can be found. The first set of solutions was found by setting $u \equiv u_p$ and increasing u_p at $Re = 2000$. Solutions could be found up to $u_p = 0.85$, beyond which the multigrid iterations did not converge, presumably because the local Reynolds number was too large. The eddy shapes are shown in Figure 4.6. The flows behaved roughly like the MST family, with the eddy bulging out as ω_0 increased, but because of the large velocity enforced near $x = 1$—not present in a Batchelor flow—the correspondence of eddy shapes is not exact. However, the sheet strength

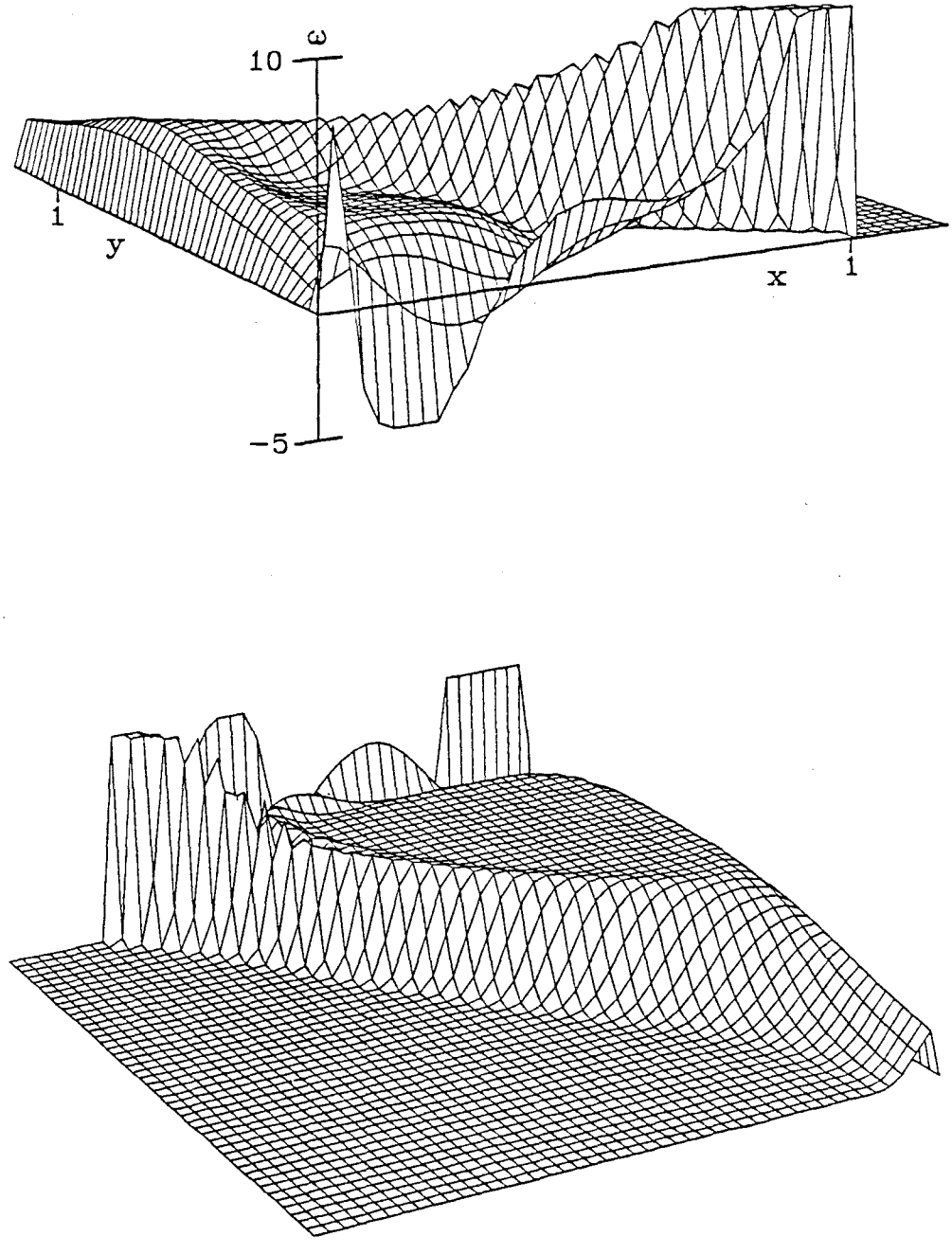

Figure 4.5 Perspective view of vorticity

(a) $u(x,0) = 0.2$, Re=1000 (compare the developed plateau here with the $u(x,0) = 0$ case in Figure 3.6); (b) $u(x)$ piecewise linear, $u_p = 1.5$, Re=2000, opposite viewpoint (note the large plateau and negligible shear layer). ω has been truncated to lie in the range $-5 < \omega < 10$ because of the singularity at the leading edge and the boundary layer on the plate.

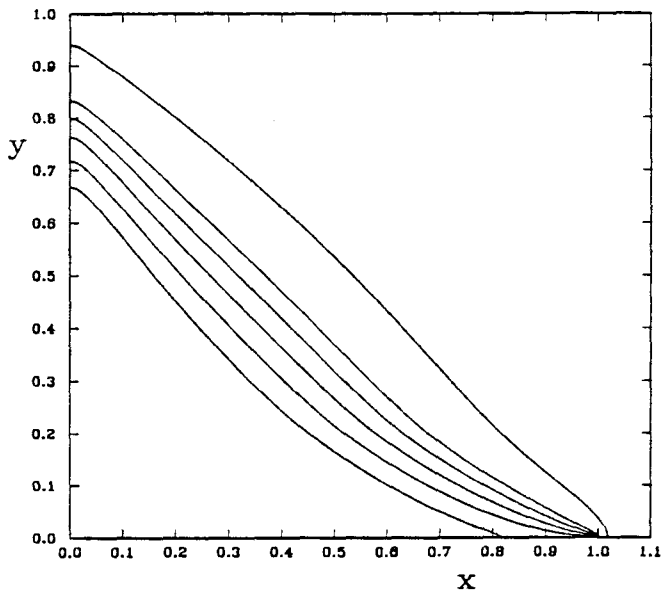

Figure 4.6 Dividing streamlines

for $u(x,0) = 0$, 0.1, 0.2, 0.3, 0.4 and 0.75 at Re=2000. The eddy is pushed outward because of the higher velocities in the interior. For larger u_p, the separation point is pushed upstream and the $x^{3/2}$ behavior is lost.

was estimated in two cases and is shown in Figure 4.7. The numerical values disagree by about 10%, but the broad features are correct, including a weak sheet with a boundary layer at the cusp when ω_0 is large.

(The sheet strength $\gamma = q_+ - q_-$ was estimated as follows. The velocity is roughly linear away from the shear layer, so it was linearly extrapolated to the point at which $\psi = 0$. For the points marked $\sqcup$, q_+ and q_- were found, giving an estimate for $q = \gamma(0)$, marked $\times$. For the points marked $\triangle$, only q_+ could be estimated, and γ was calculated from $q^2 = {q_+}^2 - {q_-}^2$. Relative arclength was defined as arclength along the line $\psi = 0$ measured from $x = 1$, divided by twice the arclength to the symmetry point $y = x$.)

4.3 Comparison with Moore-Saffman-Tanveer inviscid flows.

To see if finite Reynolds number eddies could be found that corresponded even more closely to Batchelor flows, the (somewhat artificial) boundary condition was chosen in which $u(x,0)$ is piecewise linear, and $u(0) = u(1) = 0$, $u(1/4) = u_p$. The length scale L of the corresponding Batchelor flow was estimated by extrapolating

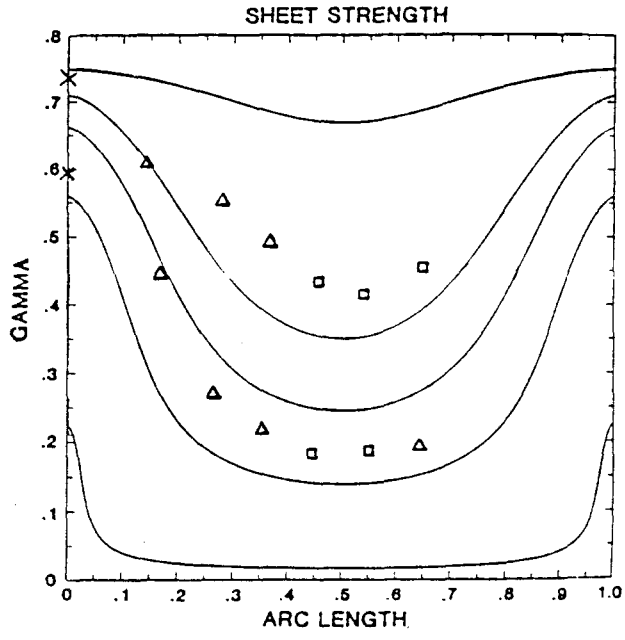

Figure 4.7 Vortex sheet strengths

The solid lines are the sheet strengths of Batchelor corner flows with internal vorticity 0.5, 3, 4, 5, and 6 (strength decreasing with increasing ω), reproduced from MST. Also shown are estimates of sheet strength for two finite-Reynolds number calculations, $u(x,0) \equiv 0.2$ at $Re = 3000$, which had $\omega_0 = 2.87$ (upper marks) and $u(x,0) \equiv 0.75$ at $Re = 2000$, $\omega_0 = 4.53$ (lower marks). See text for further explanation.

the $y \sim x^{3/2}$ behavior to the x-axis. The dividing streamlines for six u_p values are shown against the position of the vortex sheet in Figure 4.8. Considering that the width of the shear layer in these cases is more than 0.1, the agreement is extremely good, and it must be concluded that for this geometry, the limit of small viscosity is indeed a Batchelor flow.

The results for different wall conditions are summarized in Table 4.3. Both the internal vorticity and the relative size of the plateau region increase roughly linearly with u_p, the latter confirming that the presence of inviscid dynamics is controlled by the local Reynolds number. The decrease in A_2 at $u_p = 2$ shows that the ω is not completely constant; $u_p = 2$ is really beyond the limit at which we can obtain reliable results.

The question arises as to whether all of the MST vortices are possible large Reynolds number limits of Navier-Stokes solutions with appropriate boundary con-

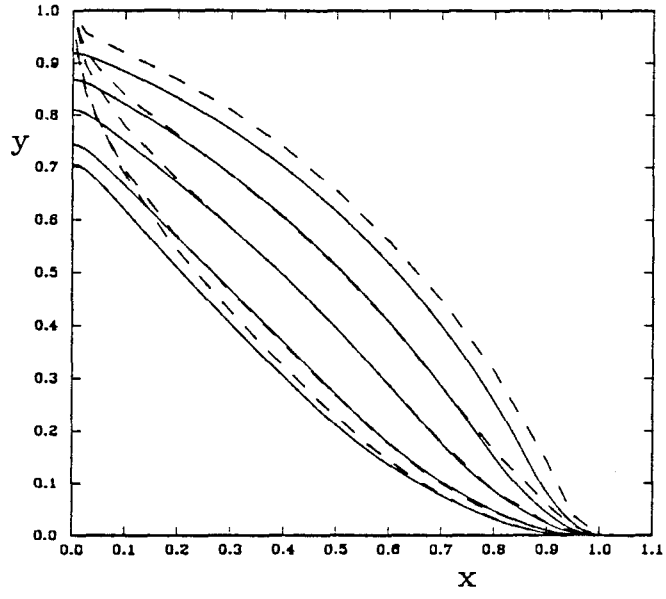

Figure 4.8 Eddy shapes and vortex sheets

The dividing streamline is shown for Re=2000, $u(x)$ piecewise linear and $u_p = 0.25$, 0.5, 1.0, 1.5, and 2, for which $\omega_0 = 2.44$, 3.19, 4.41, 5.26 and 5.98. The vortex sheet of each corresponding MST vortex flow with internal vorticity ω_0 is shown for comparison (dashed lines). For $u_p = 0.25$ and 0.5, it is drawn with length scale $L = 0.93$ and 0.96, respectively; for the others, the length scale was so close to 1 that we used $L = 1$.

ditions. Eddies with small ω_0 would be difficult to realize, since braking the flow by adding walls, etc., can cause secondary boundary layer separation, and the slow speed in the eddy would make it difficult to calculate the inviscid limit. Large ω_0 values seem quite possible, since ω_0 appears to increase linearly with u_p. Although it could level off, it seems more likely that either L would increase, giving larger and larger eddies, or that flows with $\omega_0 > 6.12$ might correspond to Batchelor flows with inward-pointing cusps, which have not been calculated.

4.4 A note on accuracy.

All the calculations used $N = 320$ and $\xi_\infty = 1.767$. Because we are not interested in knowing the vorticity gradients, etc., very accurately, we have performed less stringent tests. Computations in the $u(x,0)$ piecewise linear, $u_p = 1$ case with $N = 160$, $\xi_\infty = 1.767$ and $N = 320$, $\xi_\infty = 2.356$, showed a difference in ω_0 and ψ_c of about 2%, so the error in the $N = 320$ results is about 0.5%. At $u_p = 2$, the

Table 4.3 Properties of driven viscous corner eddies

Here the wall condition on $u(x)$ is either constant or piecewise linear, ω_0 is the value of vorticity in the plateau, A_1 is the total area of the eddy, and A_2 is the proportion of the eddy taken by the plateau. The plateau was defined as the area enclosed by a streamline such that the standard deviation of the vorticity in its interior was less than 0.05; this was found to correspond to an intuitive definition from vorticity plots such as Figure 4.5.

Re	$u(x)$	u_p	ψ_c	ω_0	A_1	A_2
1000		0.0	0.0140	1.61	0.203	0.005
2000		0.0	0.0182	1.75	0.218	0.046
3000		0.0	0.0205	1.89	0.221	0.145
4000		0.0	0.0220	1.98	0.221	0.226
5000		0.0	0.0234	2.07	0.221	0.260
1000	constant	0.2	0.0408	2.51	0.296	0.068
2000	constant	0.2	0.0458	2.74	0.302	0.222
3000	constant	0.2	0.0484	2.87	0.302	0.288
4000	constant	0.2	0.0498	2.94	0.303	0.317
2000		0.0	0.0182	1.75	0.218	0.046
2000	constant	0.1	0.0313	2.27	0.262	0.141
2000	constant	0.2	0.0458	2.74	0.302	0.222
2000	constant	0.3	0.0621	3.21	0.340	0.294
2000	constant	0.4	0.0776	3.51	0.379	0.346
2000	constant	0.75	0.1414	4.53	0.506	0.476
2000	linear	0.25	0.0346	2.44	0.252	0.187
2000	linear	0.50	0.0550	3.19	0.295	0.324
2000	linear	1.0	0.1028	4.41	0.376	0.527
2000	linear	1.5	0.1555	5.26	0.458	0.613
2000	linear	2.0	0.2125	5.98	0.540	0.430

difference was only 0.5%—the computation is more accurate for larger values of u_p. These "driven" flows appear to be governed by less subtle dynamics than those of Chapter 3. The level of vorticity in the plateau is locally undetermined and is fixed by viscous action in the boundary layers. When the wall is moving, the local Reynolds number is large everywhere, so the approach to inviscid dynamics is more rapid than in the $u(x,0) = 0$ case. The $u(x,0) \to 0$ limit is singular, because for $u(x,0) > 0$ the dividing streamline must leave from $x > 1$.

Chapter 5

Laminar separation from a leading edge

> In certain cases the flow separates from the surface at a point entirely determined by external conditions. A fluid layer, which is set in rotation by the friction on the wall, is thus forced into the free fluid and, in accomplishing a complete transformation of the flow, plays the same role as the Helmholtz separation layers. A change in the viscosity μ simply changes the thickness of the turbulent layer ... It is therefore possible to pass to the limit $\mu = 0$ and still retain the same flow figure. ... the necessary condition for the separation of the flow is that there should be a pressure increase along the surface in the direction of the flow [whose magnitude] can be determined only by the numerical evaluation of the problem which is yet to be undertaken.
>
> *L. Prandtl*, 1905

> Here the main stream, which has hitherto been in close contact with the body, suddenly, and for no obvious reason, breaks away, and downstream a region of eddying flow, which is usually turbulent even if the flow elsewhere is laminar, is set up. ... The main problem we have to face, if we believe that the boundary layer is intimately associated with separation, is how its thickness can change abruptly from $O(R^{-1/2})$ upstream of [separation] to $O(1)$ downstream, especially as the Reynolds number R may be scaled out of the boundary-layer equations. The only way in which this can happen is by breakdown of the solution of the boundary-layer equations ...
>
> *S.N. Brown and K. Stewartson*, 1969

> ... separation of the flow on a smooth surface occurs under the action of large pressure gradients acting over a small portion of the surface. The flow scheme in which it is assumed that separation ... occurs as the result of an adverse pressure gradient distributed over a finite portion of the body surface, ... apparently does not hold in actuality.
>
> *V.V. Sychev*, 1972

5.1 Introduction.

In this chapter we return to the flows of Chapter 3—a decelerating free stream impinging on an aligned, stationary flat plate—to consider the separation of the boundary layer from the plate. After a long period of development, this process is now thought to be governed by a free interaction between a thin viscous layer and the changes it induces in the external flow. Such interactions are found in a wide variety

of situations and are generally known as "triple deck" theories because of the three distinct sublayers embedded in the external flow.

Triple deck theory first emerged in 1969 when Stewartson and Williams expanded on an early idea of Lighthill's to explain supersonic separation. Stewartson (1969) and Messiter (1970) simultaneously found a similar structure at the trailing edge of a finite flat plate. The case of incompressible separation was developed by Sychev in 1972 for separation from a bluff body, and in 1979 for separation from the leading edge of a flat plate. The brief derivation below is based on this latter work, but corrects an error in Sychev's final lower deck equations.

5.2 The global flow.

The basic problem in incompressible, large-Reynolds number flows is that the limiting inviscid solution is not known. Usually there are many solutions that fit the boundary conditions. Which one is selected in the limit $Re \to \infty$ remains an open question. However, the most promising candidate in our case is a Prandtl-Batchelor flow. As discussed in Chapter 4, the one-eddy model is not correct for the stationary plate, but the global shape does seem to be roughly correct.

Two aspects of the inviscid solution are used in deriving the asymptotic theory. One is the local form of the separating streamline. This is unlikely to be affected by changes in the downstream eddy, such as asymmetry or more complicated structure (although certain coefficients could change). The other is the flow in the cusp just behind separation, which supplies a boundary condition for the triple deck. This is discussed in §5.4 below.

An example of a Prandtl-Batchelor flow is given in an appendix (§5.8). In general, if separation is located at $x = x_{\rm sep}$, then the pressure gradient in the inviscid solution just ahead of that point is given by

$$p_x \sim c(x_{\rm sep} - x)^{-1/2} \qquad \text{as } x \to x_{\rm sep}^-. \tag{5.1}$$

The constant c cannot be negative or zero, because *some* adverse pressure gradient is required for separation to take place; but $c > 0$ and an unbounded gradient appears

to imply separation upstream of x_{sep}, a contradiction. In the case of bluff body separation, the resolution is that c is positive but tends to zero as $Re \to \infty$—it turns out to be $O(Re^{-1/16})$. However, in leading edge separation (Sychev 1979), there is no contradiction because the separation point can move up to the leading edge as $Re \to \infty$; c is then a positive constant determined by the global geometry.

Thus, in contrast to the bluff body case, where c is given by the triple deck theory and the dependence of x_{sep} on c by inviscid theory (e.g., in Brodetsky (1923)), here x_{sep} is determined once c is supplied.

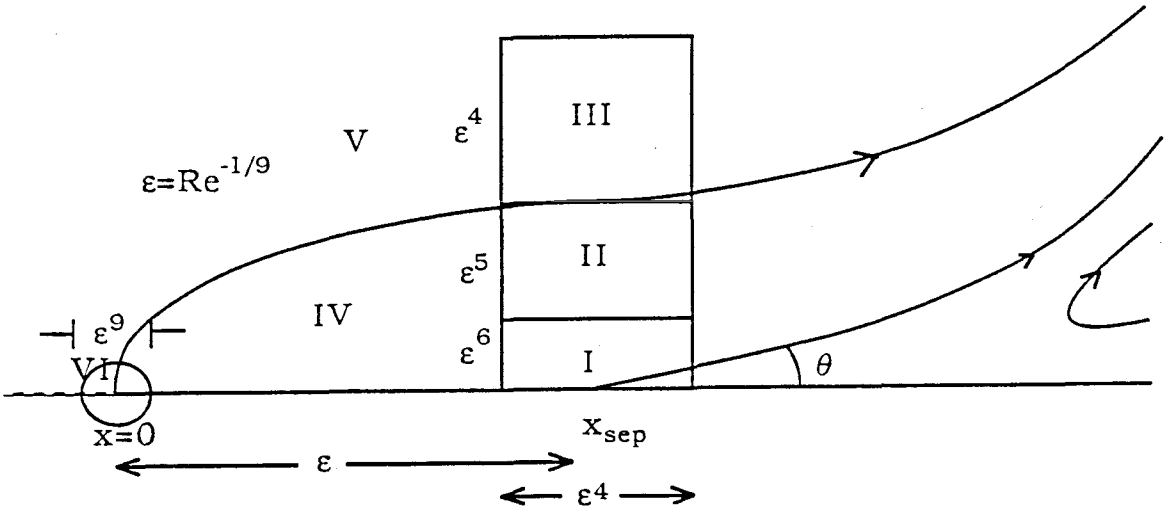

Figure 5.1 Flow structure near separation

I. Lower deck—viscous boundary layer equations hold. **II.** Middle deck—inviscid, vorticity present. **III.** Upper deck—inviscid, linearized Euler equations hold. **IV.** Blasius boundary layer. **V.** External inviscid flow. **VI.** Fully viscous—Navier-Stokes equations hold.

5.3 Construction of the triple deck.

The local flow situation is sketched in Figure 5.1, along with the various regions of the flow in which distinct approximations to the Navier-Stokes equations are valid. The small, fully viscous region at the leading edge has a purely local effect and will not be considered further here (although its effect can sometimes be substantial—see Chapter 6). The leading edge is situated at $x = 0$. Conventionally, the speed of the

external flow is taken to be positive, so that the x coordinate of Chapter 3 must be reversed.

Let ν be the kinematic viscosity, and suppose that lengths have been nondimensionalized by a characteristic length l, and velocities by the uniform straining at infinity U_∞. Then the relevant Reynolds number is $Re = U_\infty l/\nu$, and our results will be expressed in terms of the same quantities that are computed numerically.

The leading order outer solution is taken as a Prandtl-Batchelor flow separating at x_{sep}. However, we assume that the change in its behavior from the equivalent flow separating at the leading edge is a lower order correction, and use the properties of the latter.

Let U_0 be the velocity of the external flow at the leading edge. It is initially unknown, since the upstream flow is affected by the (also unknown) eddy shape. It will probably be less than the undisturbed velocity U_∞. For example, $U_0 = \frac{3}{4}$ for the irrotational corner eddy. The inviscid pressure gradient and separating streamline are given by

$$p_x = cU_0^2(x_{\text{sep}} - x)^{-1/2}, \qquad x < x_{\text{sep}}; \tag{5.2}$$

$$y_{\text{sep}} = \frac{4}{3}c(x - x_{\text{sep}})^{3/2}, \qquad x > x_{\text{sep}}. \tag{5.3}$$

Suppose that $x_{\text{sep}} \sim \varepsilon \ll 1$, and that as the singular behavior (5.2) develops in the main part of the boundary layer, it is modulated by a local interaction (initiated by a thin, viscous layer next to the plate—region I in Figure 5.1) between the pressure and the ejecting boundary layer, occurring on a small length scale $|x - x_{\text{sep}}| \sim \varepsilon^\alpha$. Then the pressure gradient $p_x \sim \varepsilon^{-\alpha/2}$. For a viscous boundary layer we require

$$uu_x \sim p_x \sim Re^{-1}u_{yy}. \tag{5.4}$$

Close to the plate $u \sim \Delta u$, giving $u \sim \varepsilon^{\alpha/4}$ and $y \sim Re^{-1/2}\varepsilon^{3\alpha/8}$. To be consistent with the inviscid breakaway (5.3), $y \sim (x - x_{\text{sep}})^{3/2}$, giving

$$x - x_{\text{sep}} \sim \varepsilon^\alpha \sim Re^{-4/9}. \tag{5.5}$$

If $\alpha > 1$, a standard attached Blasius boundary layer of thickness $Re^{-1/2}\varepsilon^{1/2}$ will already have developed by the time the interaction region is reached; and if $\alpha > 4/3$ it will be thicker than the lower deck. This is shown as region IV in Figure 5.1. The correct matching between the two layers would then be

$$\lim_{y\to 0}(u_y)_{\text{Blasius}} \sim Re^{1/2}\varepsilon^{-1/2} \quad \sim \quad (u_y)_{\text{interaction}} \sim Re^{1/2}\varepsilon^{\alpha/4-3\alpha/8}, \tag{5.6}$$

giving $\alpha = 4$ and $\varepsilon \sim Re^{-1/9}$. Values of $\alpha \leq \frac{4}{3}$ do not appear to lead to consistent matching.

Now that the dimensions of the lower deck have been found, *define* $\varepsilon_0 = (U_0 Re)^{-\frac{1}{9}}$ and change to local coordinates: let

$$u = \varepsilon_0 U_0 U, \quad v = \varepsilon_0^3 U_0 V, \quad p = \varepsilon_0^2 U_0^2 P, \quad x - x_{\text{sep}} = \varepsilon_0^4 X, \quad y = \varepsilon_0^6 Y. \tag{5.7}$$

First consider the oncoming Blasius layer which forms the upstream boundary condition for the lower deck. At a distance x from the leading edge, with an external free stream of speed U_0, its velocity profile near the wall is

$$u = U_0^{3/2} a_0 x^{-1/2} Re^{1/2} y, \tag{5.8}$$

where $a_0 \approx 0.3321$. If separation occurs at $x = \beta\varepsilon_0$, say, this is $U = a_0\beta^{-1/2}Y$ in the local coordinates.

The problem in the lower deck is now partially specified: standard boundary layer equations hold,

$$U_X + V_Y = 0, \quad UU_X + VU_Y + P_X = U_{YY}, \tag{5.9}$$

with boundary conditions

$$U = V = 0 \qquad \text{at } Y = 0 \tag{5.10}$$

$$U \to a_0\beta^{-1/2}Y, \quad V \to 0 \qquad \text{as } X \to -\infty \tag{5.11}$$

$$P \to -2c(-X)^{1/2} \qquad \text{as } X \to -\infty. \tag{5.12}$$

To complete the system we must consider the interaction between this region and the outer, inviscid flow. The $O(\varepsilon^2)$ pressure jump in the lower deck is transmitted unchanged through the continuing Blasius layer and induces a similar sized perturbation

in velocities in the main stream, of vertical extent $O(\varepsilon^4)$. Therefore, the linearized Euler equations hold, which have a known solution

$$A_X(X) \equiv V_{\text{upper}}(X,0) = -\frac{1}{\pi}\int_{-\infty}^{\infty} \frac{P(\xi)}{X-\xi}\,\mathrm{d}\xi, \tag{5.13}$$

where we have defined the displacement velocity $A(X)$, which would be an $O(\varepsilon^6)$ quantity in outer coordinates. The vertical velocity in the upper deck is $\varepsilon_0^2 U_0 V_{\text{upper}}$. This turning of streamlines cannot be supplied by the middle deck, which is essentially inviscid here, so it must match to the outer limit of the lower deck. Details of this matching process are given in Stewartson (1974). Essentially, the main deck is displaced vertically by an amount $\varepsilon_0 A(X)$, so that the position of the separating streamline y_{sep} in inner coordinates is asymptotically $A(X)$ as $X \to \infty$. The result of the matching is

$$U \to a_0 \beta^{-1/2}(Y + A(X)) \qquad \text{as } Y \to \infty. \tag{5.14}$$

Finally, (5.12)–(5.14), together with the inviscid result that $P \to 0$ downstream, imply

$$A \to -\frac{4}{3}cX^{3/2} \quad \text{as } X \to \infty, \tag{5.15}$$

which matches with (5.3).

Downstream conditions (i.e. $X \to \infty$ with Y fixed) are usually found by assuming that the inviscid flow is stagnant downstream. The outgoing shear layer entrains fluid from the eddy, with the mass supplied by an incoming reverse boundary layer on the plate.

We can now apply a linear transformation to the lower deck problem to put it in the same form as that solved by Smith (1977). There is a two parameter family of linear scalings of all variables which leaves (5.9) and (5.13) invariant. If we want both the coefficients of Y and of A in (5.14) to be 1, we must choose

$$U = \lambda\overline{U}, \quad V = \lambda^3\overline{V}, \quad X = \lambda^{-5}\overline{X}, \quad Y = \lambda^{-3}\overline{Y}, \quad P = \lambda^2\overline{P}, \quad A = \lambda^2\overline{A}, \tag{5.16}$$

where $\lambda = (a_0\beta^{-1/2})^{1/4}$. This transforms the far field boundary conditions to

$$\overline{U} \to \left(\overline{Y} + \overline{A}(\overline{X})\right) \quad \text{as } \overline{Y} \to \infty \tag{5.17}$$

$$\overline{P} \to -\alpha\left(-\overline{X}\right)^{-1/2} \quad \text{as } \overline{X} \to -\infty \tag{5.18}$$

where $\alpha = 2c\lambda^{-9/2}$.

The system (5.9) with conditions (5.10,13,17 and 18) has been solved numerically, and it appears that a solution only exists for one value of α. Smith (1977) used the Flügge-Lotz approximation to continue the boundary layer integration into the region of reversed flow and found that his iterative method only converged for $\alpha = 0.44$. Korolev (1980) used upwind differencing and found $\alpha = 0.42$. Van Dommelen and Shen (1983), using a Newton collocation method to satisfy the Hilbert relation (5.13), were able to solve the full equations directly for α, giving $\alpha = 0.415$. (We use $\alpha = 0.42$ throughout.) The lower deck problem is thus regarded as solved.

These three solutions are all qualitatively similar and are summarized in Table 5.2. Unfortunately, in some quantities which we would like to evaluate, they disagree with one another substantially.

The final step is to eliminate λ and solve for β, giving $\lambda = (\alpha/2c)^{-2/9}$ and the asymptotic distance to separation as

$$x_{\text{sep}} = \beta\varepsilon_0 = a_0^2 U_0^{-1/9}(\alpha/2c)^{16/9} Re^{-1/9}. \tag{5.19}$$

5.4 The effect of external vorticity.

The presence of vorticity in the limiting flow does not appear to alter this asymptotic structure. Inviscid considerations were discussed by J.H.B. Smith (1982). In the external flow, the addition of a flow with vorticity is subdominant at separation to the irrotational flow; in the cusp, although vorticity gives a different matching condition, the final result (5.3) for the separating streamline is unaltered. The cusp is too small for vorticity to have a local effect.

Consider an inviscid flow with internal vorticity ω_0 and external vorticity ω_1. When viscosity is present, the change in velocities in the main deck ahead of separation is $O(\omega_1 y) = O(\varepsilon^5)$, much smaller than the $O(\varepsilon^2)$ perturbations induced by the free interaction. Downstream, typical velocities inside the wedge $0 < y < y_{\text{sep}} = O((x - x_{\text{sep}})^{3/2})$ are $O(\omega_0 y_{\text{sep}})$. In the irrotational theory, there is a slow return flow near the wall of magnitude $O(\varepsilon^{13/3}(x - x_{\text{sep}})^{-5/6})$. (This is required to supply the mass for the outgoing shear layer; details are in Sychev (1979)). Comparing these two quantities, it is clear that the latter becomes dominant well before the interaction region $x - x_{\text{sep}} = O(\varepsilon^4)$ is reached. Thus, vorticity in the cusp does not alter the matching procedure of the triple deck.

In our case, and apparently in all cases of steady separation, secondary eddies appear downstream. These may alter U_0 and c slightly, but their main effect is on the downstream matching of the triple deck. We believe that there is no local change: velocities in the cusp are always extremely small, and because the return flow required by the triple deck is accelerating, it will dominate any effect which tends to zero in the cusp. There could, however, be a change farther downstream, in a region in which these two effects are of the same order.

5.5 Comparison with numerical solution of the Navier-Stokes equations.

Previous comparisons of the incompressible triple deck with experiments or calculations have found that, while separation was plausibly a local phenomenon, there was no numerical agreement in detail (Smith 1977). For example, in Fornberg's 1985 calculation of uniform flow past a cylinder up to Reynolds number 600 (based on cylinder diameter), the skin friction at separation behaves roughly like $Re^{0.65}$, instead of the bluff body triple deck dependence $Re^{7/8}$; and the pressure gradient at separation actually decreased over the entire range of Reynolds numbers considered, roughly like $Re^{-0.23}$, instead of the gradual $Re^{1/8}$ increase expected. Numerical comparisons are difficult because the limiting flow is unknown. In the Kirchoff-Helmholtz flow, $U_0 = 1$ is required to match the free stream at infinity downstream, and since the limiting

position of the separation point is known to be 55° from the front of the cylinder, the scaled skin friction $\lambda = Re^{-1/2}u_y$ there can be estimated from moderate Reynolds number calculations—although even this procedure is not formally valid. However, in a Batchelor flow, U_0, λ, and the limiting separation point are determined by the vorticity in the eddies; i.e., from a local point of view, we have two free parameters again, just as in leading edge separation.

It was hoped that by considering leading edge separation, where the interaction region is smaller, and by going to higher Reynolds numbers, better agreement could be obtained.

For the purposes of comparison, since U_0 is unknown, we first rewrite the inner variables of the lower deck in terms of the quantities actually used in the calculation. Letting $\varepsilon = Re^{-1/9} = U_0^{1/9}\varepsilon_0$, and dropping the bars on the inner variables,

$$\begin{aligned} u &= \varepsilon U' = \varepsilon U_0^{8/9}\mu^{-2/9}U, \\ v &= \varepsilon^3 V' = \varepsilon^3 U_0^{6/9}\mu^{-6/9}V, \\ p &= \varepsilon^2 P' = \varepsilon^2 U_0^{16/9}\mu^{-4/9}P, \\ x - x_{\text{sep}} &= \varepsilon^4 X' = \varepsilon^4 U_0^{-4/9}\mu^{10/9}X, \\ \text{and} \quad y &= \varepsilon^6 U' = \varepsilon^6 U_0^{-6/9}\mu^{6/9}Y, \end{aligned} \tag{5.20}$$

where $\mu = (\alpha/2c)$. Primed coordinates can then be directly calculated. Some additional quantities of interest are the skin friction and pressure gradients:

$$\tau_x \equiv u_{yx} = \varepsilon^{-9}T'_{X'} = \varepsilon^{-9}U_0^2\mu^{-2}T_X, \tag{5.21}$$

$$\text{and} \quad p_x = \varepsilon^{-2}P'_{X'} = \varepsilon^{-2}U_0^{20/9}\mu^{-14/9}P_X. \tag{5.22}$$

Here $T = U_Y$ is the lower deck skin friction.

In Table 5.1, various flow quantities from the calculations of Chapter 3 are measured near separation. As in Chapter 3, the sign of p_x has been changed so that a positive value represents an adverse pressure gradient, as in (5.1). The effect of Reynolds number on dependent variables is shown in Figure 5.2, and on streamwise scales in Figure 5.3. It is immediately apparent that the qualitative predictions of

Table 5.1 Separation at finite Reynolds number

Re	x_{sep}	$-\tau_x(x_{\text{sep}})$	$-T'(0)$	$\min \tau$	$\min T$
150	0.4304	6.106	0.0407	-0.63	-0.0391
400	0.3032	15.96	0.0399	-1.07	-0.0384
1000	0.2185	41.12	0.0411	-1.92	-0.0413
2000	0.1722	84.44	0.0422	-3.00	-0.0439
3000	0.1503	129.9	0.0433	-3.91	-0.0458
4000	0.1367	175.7	0.0439	-4.81	-0.0479
5000	0.1271	223.0	0.0446	-5.45	-0.0480
Power law fit:	$Re^{-0.34}$	$Re^{1.05}$		$Re^{0.60}$	
Re	$p_x(x_{\text{sep}})$	$P'_{X'}(0)$	$\max p_x$	$\max P'_{X'}$	
150	0.1828	0.0600	0.4651	0.1527	
400	0.2298	0.0607	0.5745	0.1517	
1000	0.2999	0.0646	0.7005	0.1509	
2000	0.3693	0.0682	0.8628	0.1593	
3000	0.4208	0.0710	0.9459	0.1596	
4000	0.4618	0.0731	0.9951	0.1575	
5000	0.4978	0.0750	1.0261	0.1546	
Power law fit:	$Re^{0.34}$		$Re^{0.24}$		

triple deck theory are fully confirmed. As the Reynolds number increases, an increasingly large pressure gradient does act over a decreasing region of the plate, triggering separation.

We therefore move on to consider quantitative comparisons, for which we need values for U_0 and c to determine the scalings in (5.20). We also need values to compare *to*, which unfortunately are not known reliably; results of the three solutions of the lower deck problem are summarized in Table 5.2.

5.5.1 Skin friction at the wall.

These are shown in scaled coordinates X', T' in Figure 5.3 for $150 \leq Re \leq 5000$. Numerical values of $\tau_x(x_{\text{sep}})$ are given in Table 5.1. The skin friction near separation scales in precisely the manner predicted by the theory. The best fit of a power law relationship on the skin friction gradient gives $\tau_x(x_{\text{sep}}) \sim Re^{1.05}$, extremely close to the triple deck exponent of 1. $T'(X')$ appears to have converged, at least to graphical

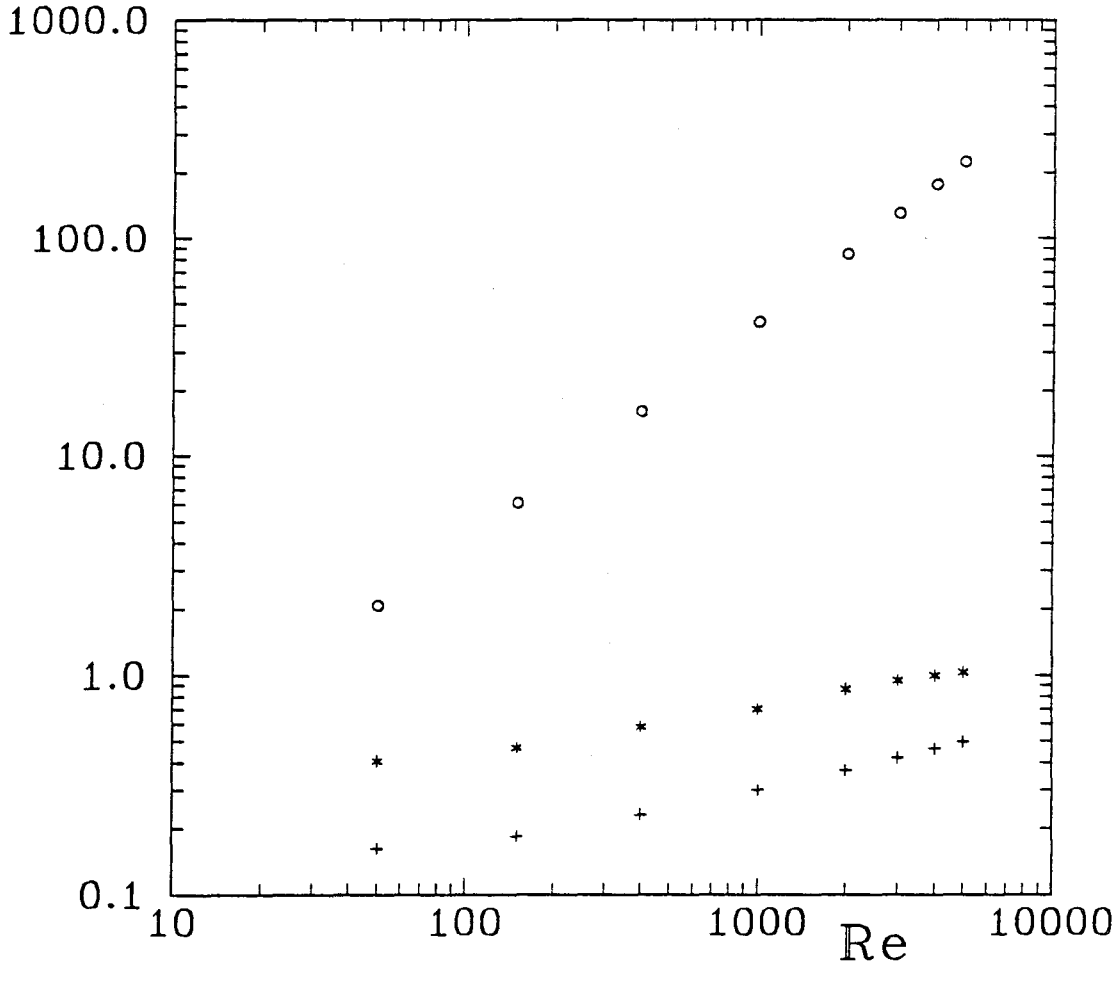

Figure 5.2 Effect of Reynolds number on laminar separation

Here the Reynolds number increases by a factor of 100. The skin friction gradient at separation, $u_{yx}(x_{sep})$, is marked o. The adverse pressure gradient at separation is marked $\star$. The maximum adverse pressure gradient on the plate is marked +.

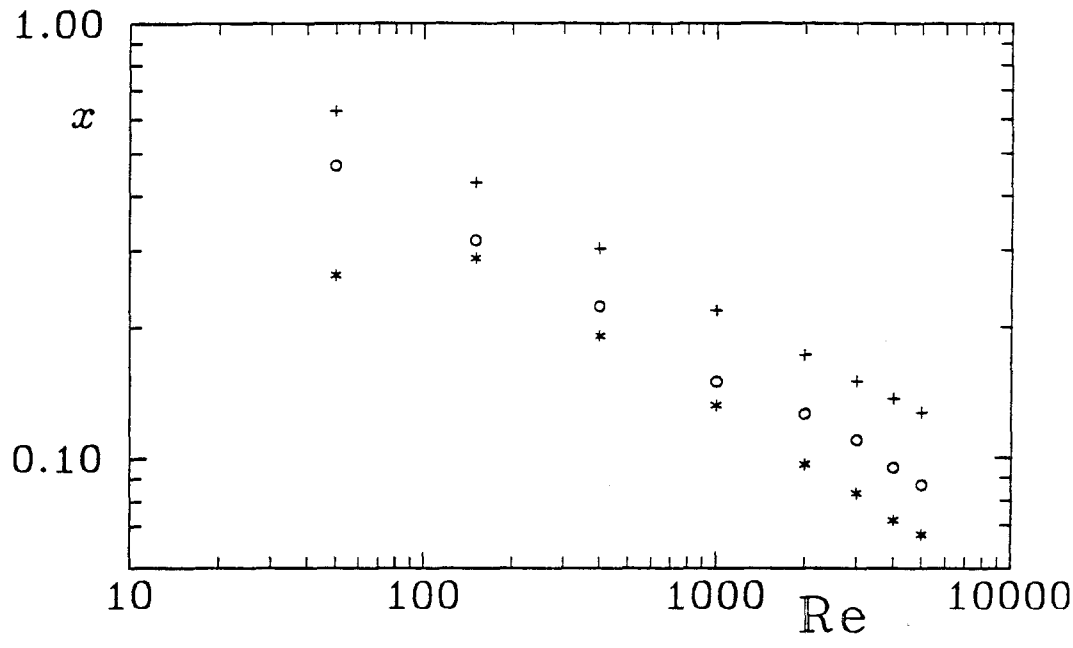

Figure 5.3 Effect of Reynolds number on streamwise scales

The distance from the leading edge to the separation point is marked +. The distance upstream from separation to the point of maximum pressure gradient is marked o. The distance downstream from separation to the point of minimum skin friction is marked $\star$.

accuracy, over the range $-4 < X' < 6$. It reaches a minimum behind the separation point, as predicted, which is proportional to $Re^{0.60}$, close to the triple deck exponent of 5/9. The main qualitative discrepancy is that it is concave upward for $X' < -1$; but as the leading edge is still quite close (at $X' = -5.6$ at $Re = 5000$), this is probably due to the influence of $x^{-1/2}$ singularity there.

If we try to find values of U_0 and μ by matching to the known lower deck solution, however, we immediately run into problems. Positioning the minimum correctly requires $U_0^{-4/9}\mu^{10/9} \sim 0.5$, and matching its value requires $U_0^{14/9}\mu^{-8/9} \sim 1.65$ (using values at $Re = 5000$), or $U_0 = 0.97$, $\mu = 0.54$; these values give $-T_X(0) = 0.11$, three or four times too large.

In other words, no values of U_0 and μ correctly account for the main observed features of the skin friction.

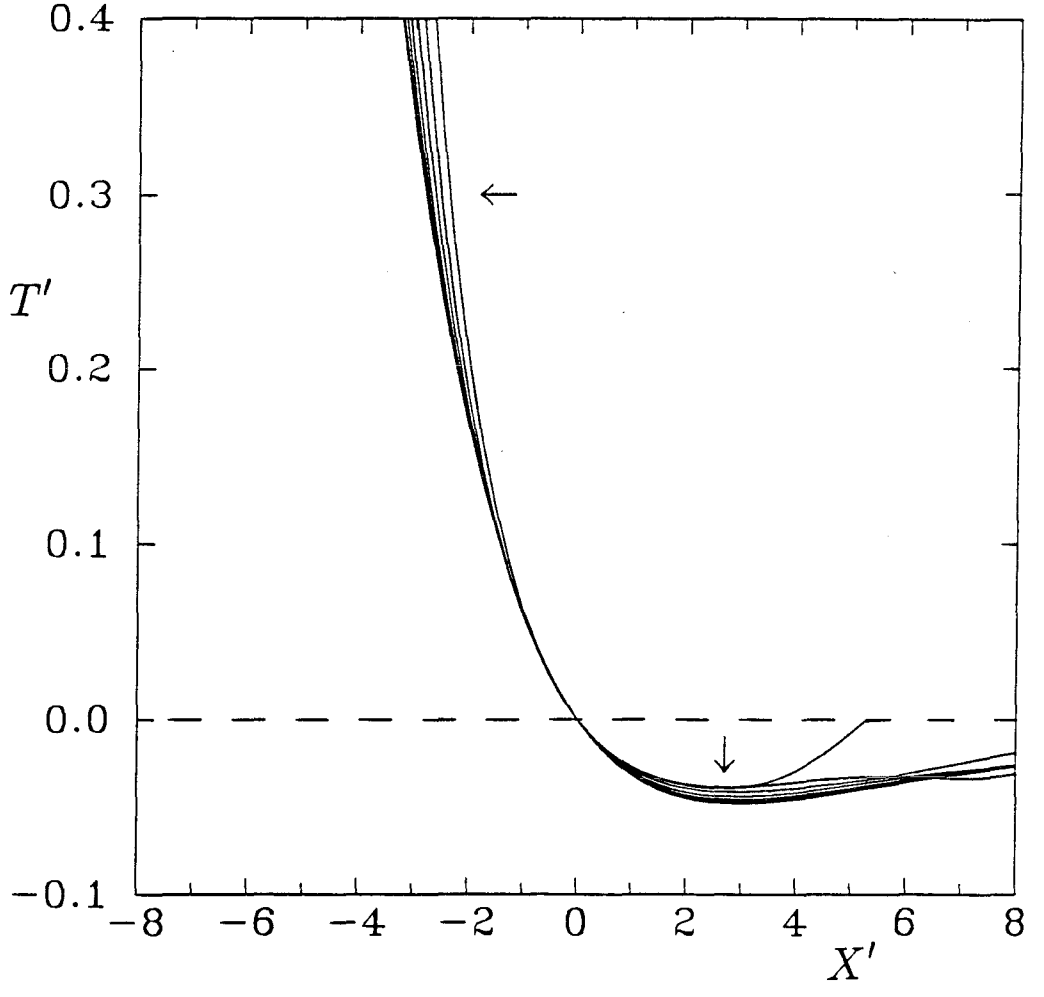

Figure 5.4 Skin friction near separation in scaled coordinates.
Here Re = 150, 400, 1000, 2000, 3000, 4000, and 5000, and arrows indicate the direction of increasing Reynolds number.

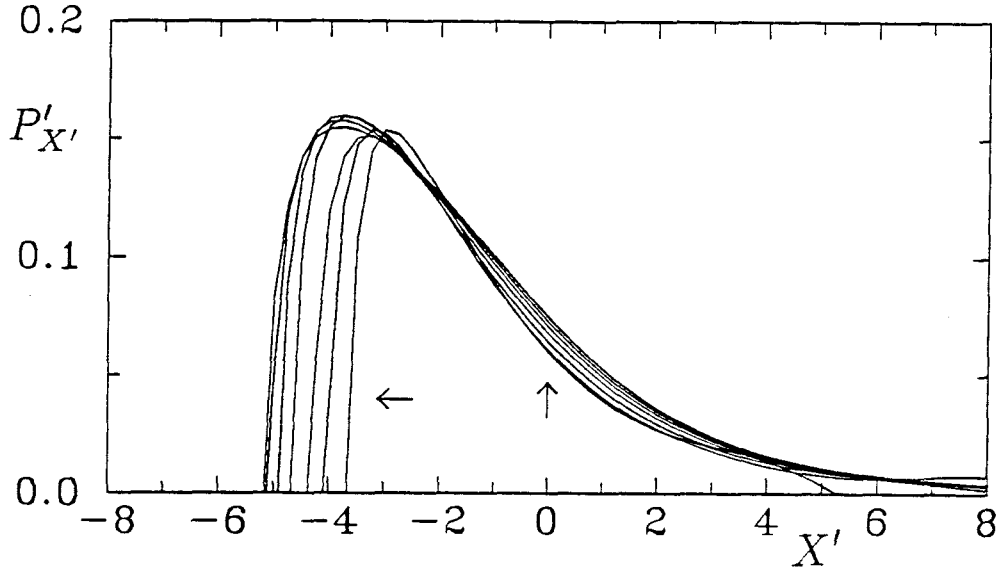

Figure 5.5 Pressure gradient at the plate near separation in scaled coordinates. See Figure 5.4 for caption.

Table 5.2 Properties of lower deck solution

Values from three calculations (Smith (1977), Korolev(1980) and van Dommelen and Shen (1983)) are compared. The maximum pressure gradient is attained between $X = -3$ and $X = -4$, and the minimum skin friction between $X = 6$ and $X = 8$. The values from $Re = 5000$ are given in primed coordinates, i.e., without factors of U_0 and μ (see (5.20)).

	α	$-T_X(0)$	$\min T$	$P_X(0)$	$\max P_X$
Smith	0.44	0.033*	-0.079†	0.073*	0.090*
Korolev	0.42	0.036*	-0.078†	0.072*	0.086*
v. D. & S.	0.415	0.025*	-0.079	0.072†	0.075
$Re = 5000$		0.045	-0.048 (at $X' = -3$)	0.075	0.155 (at $X' = -3.75$)

†Value read from graph
* Slope read from graph

5.5.2 Pressure gradient.

These are shown in Figure 5.5. The pressure gradients scale approximately correctly in x, and maintain the same general profile in $-4 < X < 6$. The leading edge singularity is seen to the left; however, once the Reynolds number is greater than about 1000, the pressure gradient maximum has settled down and does not seem to be influenced by the singularity. Again, we have qualitative agreement with the theory: there is a pressure gradient maximum followed by a fall to zero behind

separation.

However, throughout the whole range of Reynolds numbers, there remain three major discrepancies. Firstly, $p_x(x_{\rm sep})$ is increasing faster than predicted rate ($p_x \sim Re^{0.34}$, compared to the predicted exponent 2/9). Secondly, the maximum pressure gradient is about twice as large as the value at separation, instead of 5%–20% larger, and it decays much too rapidly. Finally, there is no way that the positions of the pressure gradient and skin friction extrema can both be scaled to agree with the lower deck solutions.

If we discount the large maxima as caused by the proximity of the leading edge, we might take $P'_{X'}(0) = 0.075$ to obtain the matching condition $U_0^{20/9}\mu^{-14/9} = 0.97$. Together with $T'_{X'}(0) = -0.045$ or $U_0^2\mu^{-2} = 1.36$, we find $U_0 = 0.67$, $\mu = 0.57$. These are plausible values, but this "matching" is hardly a good fit: nothing agrees except the two values we have selected.

5.5.3 Distance to separation.

These are shown in Figure 5.3. They appear to have an exact power law dependence on the Reynolds number: $x_{\rm sep} \sim Re^{-0.34}$. This is completely at odds with triple deck theory, which predicts an exponent of $-1/9$. However, recall that this $Re^{-1/9}$ dependence came from matching the Blasius boundary layer to the *upstream* limit of the interaction region (see (5.11)), and that the asymptotic sizes of this region, given in (5.7), had already been found before we did that final matching. So it is not implausible that the interaction region could develop at a lower Reynolds number than that for the final behavior (5.19).

If we regard (5.19) as specifying the *onset* of the interaction region (unfortunately only vaguely defined in the theory), we might expect a large component of order $X = Re^{-4/9}$ in $x_{\rm sep}$. Indeed, a best fit of $x_{\rm sep}$ to functions of the form $aRe^{-1/9} + bRe^{-\gamma}$ gives $\gamma = 0.43$, very close to 4/9. Under this hypothesis, significant departure from straight line behavior in Figure 5.3 might not be seen until the Reynolds number is in the range 10^4 to 10^5.

5.6 Higher order matching.

There are no values of the parameters U_0 and μ that can make the difference between the computed profiles and the lower deck solutions less than a factor of about two. But, since we have verified the main features of the free interaction, let us relax our standards and *assume* that triple deck theory is valid. U_0 and μ are determined by the external flow, which sees only the shape and outer velocity of the shear layer centered on the separating streamline $\psi = 0$. These quantities seem to depend only weakly on the detailed structure of the eddy. For example, we computed a flow with stationary walls at both $y = 0$, $-1 < x < 1$ and $x = 0$, $-1 < y < 1$. The extra downstream wall braked the eddy (ψ_c was reduced from 0.014 to 0.009) and made it fully viscous, but all the separation quantities in Table 5.1 changed by only 1–2%. Since the shape of the eddies is very similar to that of the Moore-Saffman-Tanveer vortex with the same internal vorticity level, it seems reasonable to use that vortex as a model of the external flow. Of course, the secondary eddy could have a *local* effect not visible in Figure 4.2, which will change the constants; however, in the MST vortices, U_0 and μ depend very weakly on ω_0 (at least for $\omega_0 <\sim 4$).

We therefore investigate the consequences of taking $\omega_0 = 2$, $U_0 = 0.734$ and $\mu = 2\alpha/3a = 0.493$.

In triple deck theory, all quantities Q are expanded in each deck as a power series in ε; i.e., $Q = \varepsilon^n(Q_0 + \varepsilon Q_1 + \varepsilon^2 Q_2 + \ldots)$. Matched asymptotics gives n, but to date, the lower deck problem has only been solved to first order: only Q_0 has been found.

There is no reason to believe that the higher order coefficients Q_1, Q_2, ... are small compared to Q_0, and their effect may be considerable, because ε is so large ($5000^{-1/9} = 0.388$). In Figure 5.6 we have plotted $T'(-2)$, $T'_{X'}(0)$, and $\min T'$ against ε. Remarkably, for $Re \geq 1000$, they all seem to be linear functions of ε. The same behavior is seen in Figure 5.7 for the pressure gradients at five values of X'. We thus make the guess that the effect of second and higher order terms is small, and linearly extrapolate to $\varepsilon = 0$ to determine Q'_0 and Q'_1 in each case.

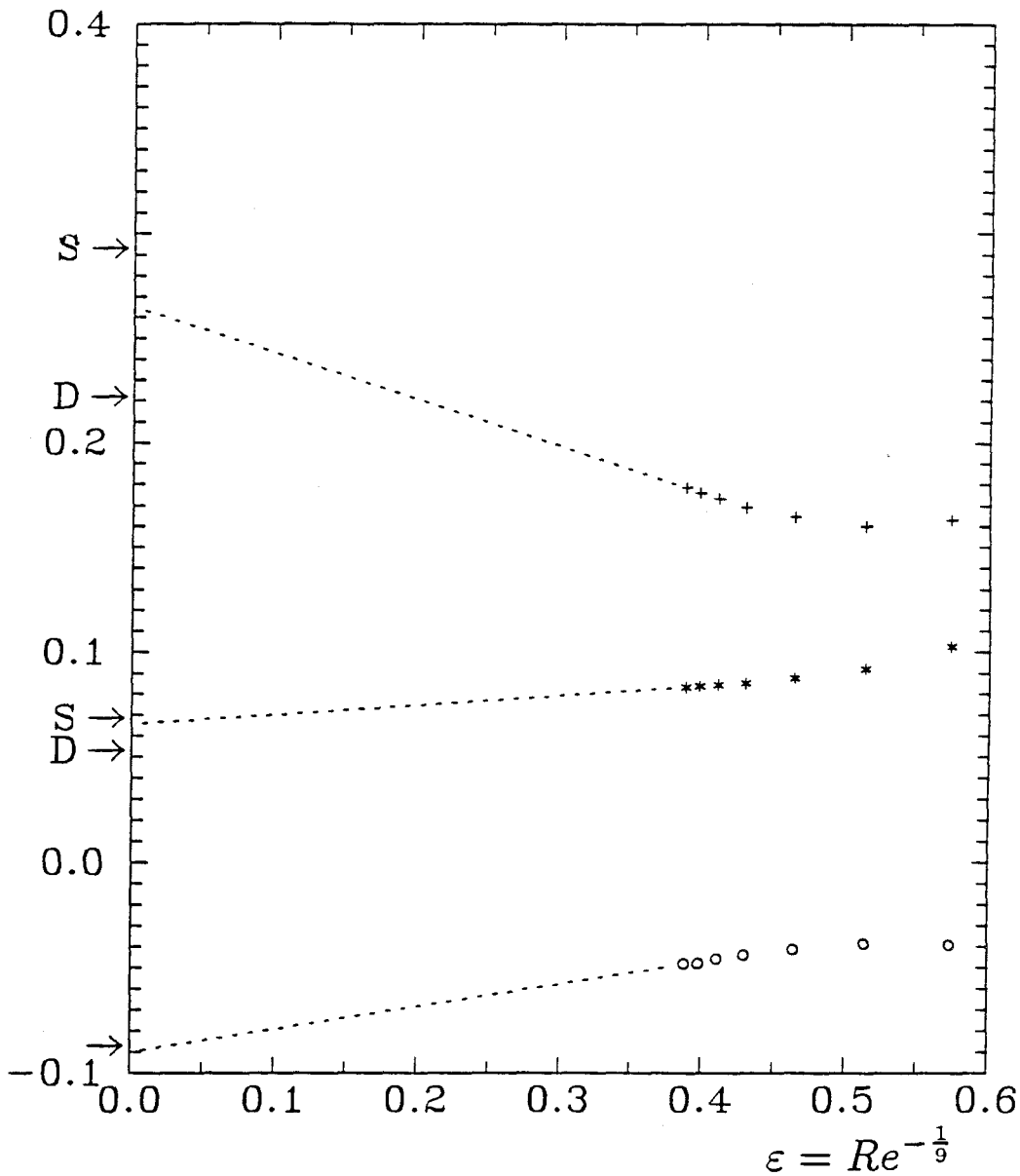

Figure 5.6 Second order fit to skin friction

Here $\varepsilon = Re^{-1/9}$, and results are given for $150 \leq Re \leq 5000$. $\min T'$ is given by $\circ$. $T'(-2)/2$ is given by $\star$, and $-4T'_{X'}(0)$ by $+$. The straight lines are the linear least squares fits through the four highest Reynolds numbers. At $\varepsilon = 0$, the extrapolated value is compared to the lower deck solutions of F.T. Smith (marked S) and van Dommelen and Shen (marked D).

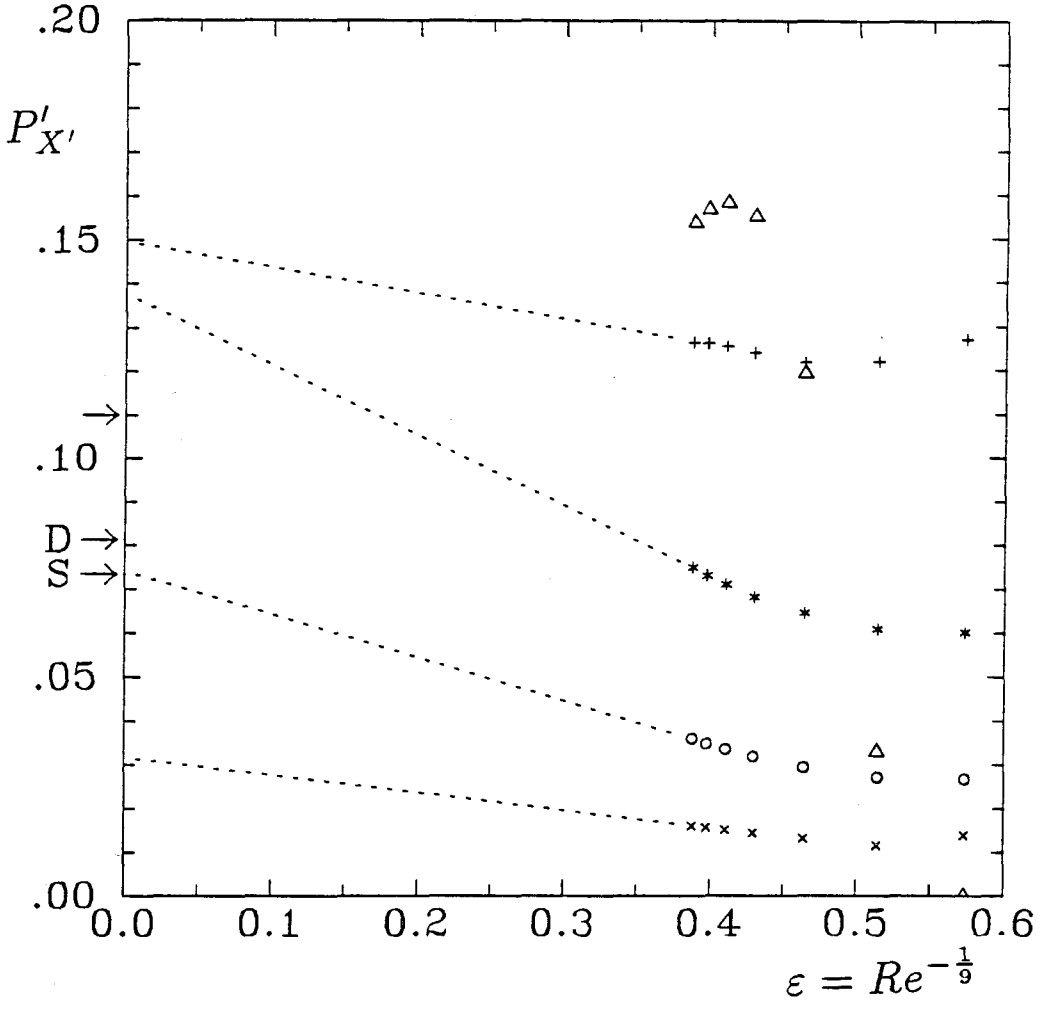

Figure 5.7 Second order fit to pressure gradient

See Figure 5.6 for caption. $P'_{X'}$ is given for $X' = -4$, -2, 0, 2, and 4, shown by Δ, $+$, $\star$, $\circ$, and $\times$ respectively. The extrapolated values are compared to the lower deck solution at $X' = -2$ and $X' = 0$.

5.6.1 Skin friction.

We find $\min T_0' = -0.090$, or $\min T_0 = -0.078$, exactly agreeing with first order triple deck theory. The minimum occurs at $X' \sim -3.4$, or $X \sim -6.5$, which also agrees exactly.

Linear extrapolation of the skin friction gradients at separation, shown as + in Figure 5.6, gives $-T'_{X'0} = 0.066$, or $-T_{X0} = 0.030$, which is bracketed by the triple deck results for this quantity, 0.025, 0.033, and 0.036. At least the error is no more than about 20%.

Carrying out the procedure at different values of X' also gives consistent results, as shown in Figure 5.9. This good agreement increases our confidence in the linear extrapolation, i.e., in ignoring possible higher order terms.

5.6.2 Pressure gradient.

Here the numerical agreement is less good although the procedure does reduce the errors considerably. It turns out that the maximum at $X' \sim -3.5$ is a higher order effect, as is the observed rapid decrease through separation. $P'_{X'}(-4)$, given by circles in Figure 5.7, has just started to decrease at the highest Reynolds numbers considered. It cannot be reliably extrapolated to $\varepsilon = 0$, but clearly its limit is less than $P'_{X'0}(-2)$.

At $X' = -2$ and 0 we find $P'_{X'0} = 0.150$ and 0.138, respectively, or $P_{X0} = 0.099$ and 0.091, giving a maximum pressure gradient about 9% larger than the value at separation. These values are larger than the triple deck values by 15–25%, although this error is much smaller than in our first order matching.

At $X' = 2$ and 4 the errors are much less. The overall agreement is shown in Figure 5.10.

5.6.3 Distance to separation.

After the above successes, we might hope that a higher order matching will also explain the calculated values of x_{sep}. In this case, as noted in §5.5.2, we expect large

Table 5.3 Extrapolation to $\varepsilon = 0$

As explained in §5.6 and Figures 5.6 and 5.7, a linear best fit was made of various quantities against ε, through Re = 2000, 3000, 4000 and 5000. The line is then transformed to standard lower deck coordinates using $U_0 = 0.734$ and $\mu = 0.493$. Q_0 is the $\varepsilon = 0$ intercept and Q_1 is the slope.

Quantity	X	Q_0	Q_1
T	-3.82	0.113	0.078
T_X	0	-0.030	0.025
$\min T$		-0.078	0.092
T	7.65	0.072	0.082
P_X	-7.65	~ 0.08	> 0
P_X	-3.82	0.099	-0.039
P_X	0	0.091	-0.107
P_X	3.82	0.049	-0.065
P_X	7.65	0.021	-0.027

contributions of order ε^4, so a linear extrapolation is not sufficient. In addition, the first order term, given in (5.19), is so small compared to the higher order terms that it is swamped by the errors in the calculations.

When $U_0 = 0.734$ and $\mu = 0.493$, (5.19) gives $x_{\text{sep}} = 0.0325\varepsilon$. A fit to x_{sep} of the form $a\varepsilon + b\varepsilon^4$ gives $a = 0.14$ and $b = 3.26$, but this does not explain all the variability in the data. Unfortunately, fitting a full fourth order polynomial gives unrealistic results (with, for example, $a < 0$). Our results are simply not accurate enough to capture this many terms in the expansion of x_{sep}.

One plausible, accurate fit was obtained by dropping the quadratic term:

$$x_{\text{sep}} = 0.0501\varepsilon + 1.2042\varepsilon^3 + 1.6244\varepsilon^4 + e, \tag{5.23}$$

where $|e| < 0.0004$. This is shown in Figure 5.8. Its estimate for the coefficient of the linear term is the right order of magnitude, but it would be extremely hard to obtain a better matching from finite Reynolds number calculations, or even to prove or disprove (5.23): the exponents are just too small and the sought after effect is at too high an order.

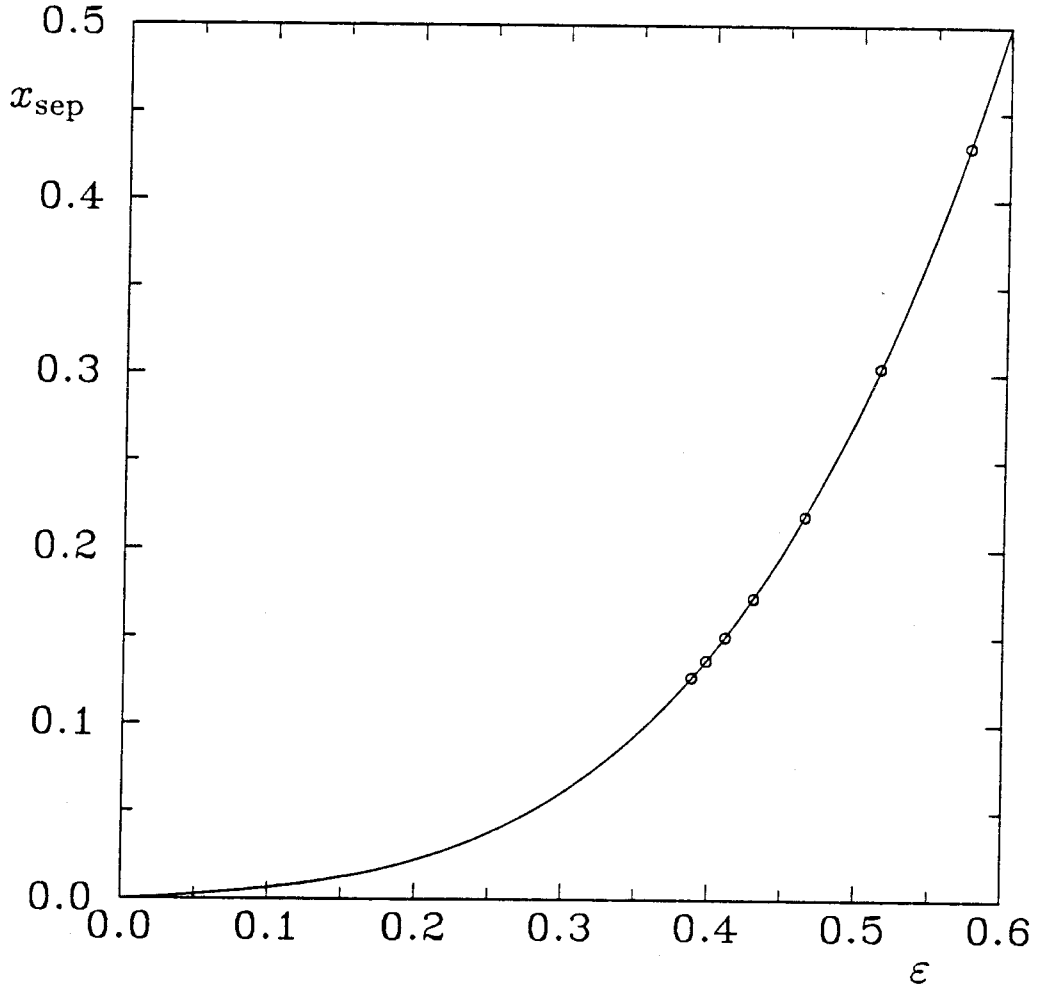

Figure 5.8 Distance to separation

The distance from the leading edge to the separation point is shown for $150 \leq Re \leq 5000$. The solid line is a plausible fit based on triple deck theory, given by (5.23).

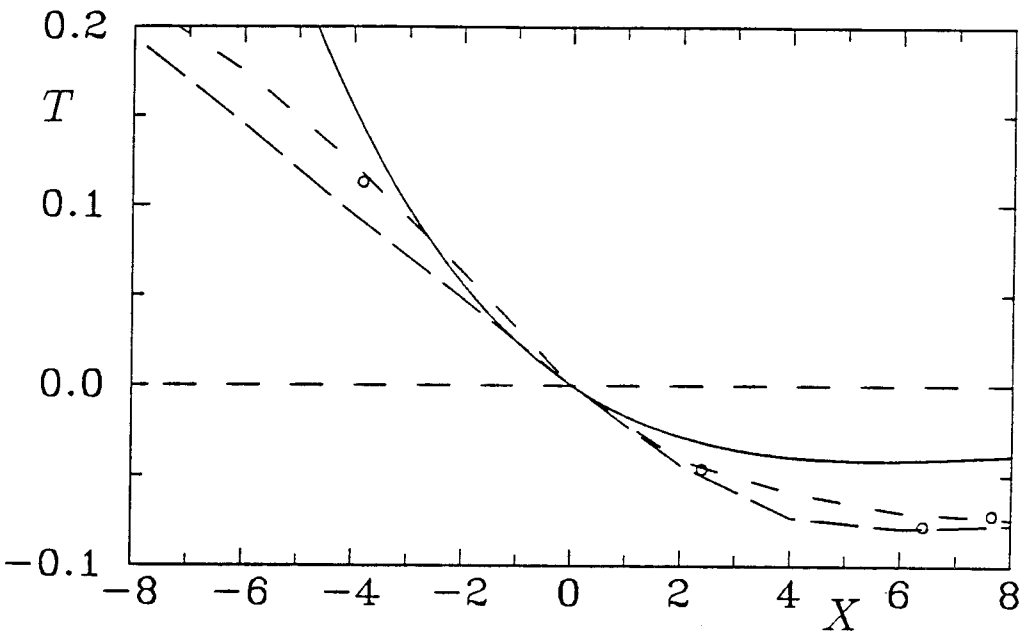

Figure 5.9 Skin friction compared with triple deck theory

Results are given in the standard lower deck coordinates X, T. The solid line is the $Re = 5000$ calculation (see Figure 5.4 for lower Reynolds numbers). The large dashes are van Dommelen and Shen's lower deck solution, and the small dashes are F.T. Smith's. The circles represent a linear extrapolation from the finite Reynolds number calculations. The value at $X = 6.5$ is the extrapolated minimum skin friction.

5.7 Discussion.

Second order matching removes all the qualitative disagreements (noted in §5.5) between the calculated flow near separation and the lower deck results. It also reduces the quantitative differences to about 20% or less when plausible values of U_0 and μ are used. The final comparison between our results and triple deck theory is shown in Figures 5.9 and 5.10.

This procedure could never be used to *find* U_0 and μ. In the MST family of vortices, $dU_0/d\omega_0 < 0$ and $d\mu/d\omega_0 < 0$. All the quantities of interest (see (5.20)–(5.22)) have a positive power of U_0 and a negative power of μ, so any system of equations designed to match them would be very ill-conditioned.

Our whole procedure that leads to a numerical confirmation of triple deck theory is based on the linear extrapolations in Figures 5.6 and 5.7. If higher order terms are not, in fact, small, then the extrapolation is not valid and the agreement is accidental.

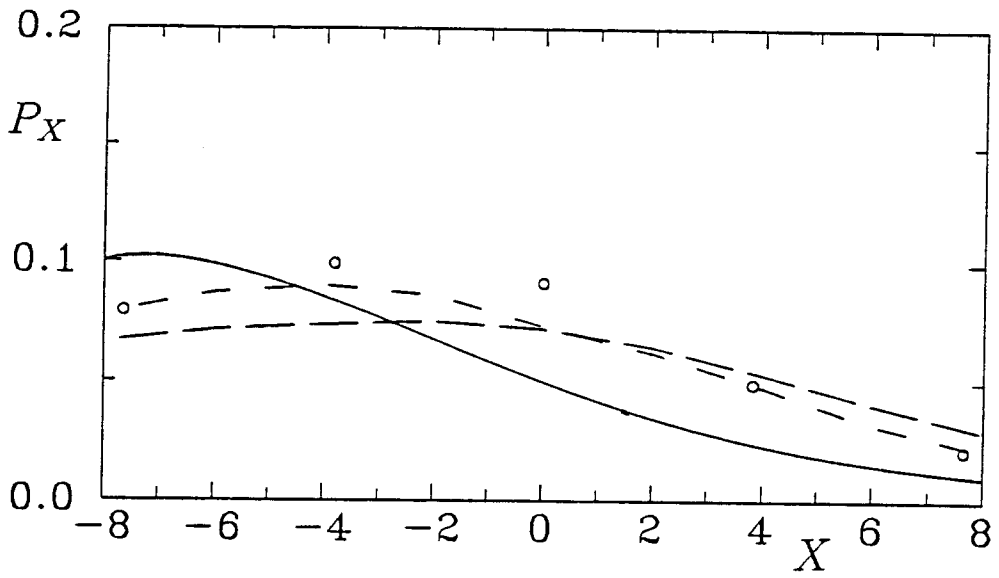

Figure 5.10 Pressure gradient compared with triple deck theory
See Figure 5.9 for legend.

(Note that the range of ε over which the linear behavior is observed is so small that a small quadratic effect would look like a linear one.) However, separation at the Reynolds numbers considered certainly does not match the first order theory.

A by-product of the extrapolation is an estimate of the second order correction at that point. These are given in Table 5.3. T_1 is everywhere positive (about 0.08) and has a fairly sudden increase near $X = 0$. P_{X1} is initially positive, changes sign at $X \sim 5$, and has a large maximum near $X = 0$. These predictions can be tested when the lower deck problem has been solved to second order. In the case of x_{sep}, only the guess that its quadratic term is small could be checked.

What is the source of the second order corrections? Obviously, there are the contributions induced by the first order terms, and terms from the regular perturbation expansion of the upstream boundary layer. But several important effects only enter at higher order. One is from the external flow: it separates at x_{sep}, but U_0 and c are evaluated from the flow separating at the leading edge. The MST vortex separating at $L = 1 - x_{\text{sep}}$ has separation speed LU_0 and streamline $y_{\text{sep}} \sim L^{-1/2} c x^{3/2}$. A naive application of (5.22) would then give $p_x \propto L^{14/9}$, so this can be a substantial effect.

To find it, (5.23) indicates that we would have to continue to fourth order.

The inviscid pressure gradient at separation is $p_x = U_0^2(cx^{-1/2} + c^2 + O(x^{1/2})$; i.e., it proceeds in powers of ε^2. Although the free interaction induces terms of ε^{-2}, ε^{-1} and every higher order in the interaction region, clearly the constant term in p_x will have a large influence which is only captured at third order. For example, in the irrotational corner eddy, p_x does not even start increasing until $x \sim 0.05$.

For these reasons, the linear dependence on ε in our results is rather surprising, although the close agreement with the lower deck solution stands in its favor.

5.8 Appendix: the stagnant corner eddy.

The Prandtl-Batchelor corner flow can be calculated using Kirchoff-Helmholtz free streamline theory in the case $\omega_0 = 0$ (and hence $u \equiv v \equiv 0$ in the eddy). The flow is assumed to separate at $x = 1$, $y = 0$ and reattach at $x = 0$, $y = 1$. The shape of the separating streamline and the velocity there are initially unknown.

The speed on the separating streamline is found to be $U_0 = 3/4$, and the complex velocity potential w at a point $z = x + iy$ is given implicitly by

$$z = \lambda + \frac{1}{3}\lambda^3, \tag{5.24}$$

where

$$\lambda = i\sqrt{w + \sqrt{w^2 - 9/16}}, \tag{5.25}$$

and positive square roots are taken on the positive real axis. The separating streamline is given by $\Im w = 0$ and $|w| < \frac{4}{3}$; then (5.24) reduces to $x^{2/3} + y^{2/3} = 1$, or $y \sim (\frac{2}{3}(1-x))^{3/2}$ as $x \to 1$. So the constant c in (5.3) is $\frac{3}{4}(\frac{2}{3})^{3/2}$ in this case.

The velocity u on $x > 1$, $y = 0$ is given implicitly by $x = u + \frac{1}{3}U_0^4 u^{-3}$, from which the behavior (5.2) can be retrieved.

Chapter 6

High Reynolds number flow over a finite flat plate

6.1 History and overview.

Determining the flow over a finite flat plate aligned with a uniform free stream is a classic problem in boundary layer theory. Unlike the flow past a semi-infinite plate, which is now understood and is discussed in Van Dyke (1964), the finite plate is considerably more complicated because of the multistructured wake and its upstream influence. Van Dyke also reviews this problem, but our brief study suggests that previous workers were too hasty to declare the problem closed.

Let the free stream be given by $u = 1$, $v = 0$ at infinity, and let the flat plate lie on the x axis between $x = 0$ and $x = 1$; then the Reynolds number R is given by $1/\nu$. The leading order behavior of the boundary layer was given by Blasius (1908): the local skin friction is $c_{\rm Bl} = \lambda(x/R)^{-1/2}$, where $\lambda = .33206$, and the normalized drag coefficient is $D_{\rm Bl} = 4\lambda R^{-1/2}$. This is valid when $x >> R^{-1/2}$; close to the leading edge, the boundary layer approximation is not valid, and a full Navier-Stokes solution is required, given by Veldman and van de Vooren, (1974), who found that the skin friction near the leading edge is about 13% larger than the Blasius value. We express the skin friction and drag relative to their Blasius values; i.e.,

$$\tau = \frac{u_y}{c_{\rm Bl}} \quad \text{and} \quad D = \frac{\nu \int_0^1 u_y \, dx}{D_{\rm Bl}}.$$

Goldstein (1930) analyzed the wake just behind the plate, and found a two-tiered structure, consisting of the continuing, constant Blasius layer, and an inner layer, required because of the change in boundary conditions at $x = 1$, in which $u(x, 0)$ grows like $(x - 1)^{1/3}$. The far wake has a similarity form, given in (6.3) below.

Kuo (1953) attempted to find the next term in the boundary layer of the main part of the plate by assuming that the vertical velocity outside the boundary layer

is zero in $x > 1$. The displacement effect of the first order boundary layer on the external flow can then be calculated, and finally the boundary layer equations re-integrated with this new external flow. This procedure gives the second order skin friction and drag as

$$\tau = 1 + R^{-1/2}K(x), \quad D = 1 + 3.10R^{-1/2}. \tag{6.1}$$

He found good agreement with observed and calculated values of the drag. This agreement, however, appears to be accidental: in the first place, the viscous region near the leading edge also contributes an $O(R^{-1/2})$ term to the drag, (as noted by Van Dyke (1964)), but more seriously, $K(x)$ is too small by a factor of at least 2 over most of the plate, say in $x < 0.8$. $K(x)$ has a logarithmic singularity at $x = 1$; thus, most of its integrated skin friction comes from near the trailing edge, which is just where Kuo's approximation is most questionable. The agreement in drag is thus a numerical coincidence, the deficit in skin friction over most of the plate being balanced by an excess caused by the singularity.

The theoretical situation was revolutionized by the independent discovery by Stewartson (1969) and Messiter (1970) that the upstream influence of Goldstein's sublayer is of streamwise extent $O(R^{-3/8})$, and is described by a triple deck established around the trailing edge. Full details are available elsewhere, for example in Stewartson's excellent review (1974). The lower deck equations are the same as those found in laminar separation, but the boundary conditions at $y = 0$ and as $x, y \to \infty$ are different. Also, because the limiting solution is known, there are no free parameters left in the equations or the scalings. This simplifies matters considerably, and the lower deck equations were solved by Jobe and Burggraf (1974), and later by Veldman and van de Vooren (1974) and by Melnik and Chow (1975), who found

$$\tau = 1 + \sqrt{x}\,T(X), \quad D = 1 + 2.00R^{-3/8}, \tag{6.2}$$

where $X = \lambda^{5/4}R^{3/8}(x - 1)$ is the inner length. (The $\sqrt{x}$ term arises from our definition of τ). They, too, reported excellent agreement with the drag, down to

a Reynolds number of 1 (!), and said that the numerical Navier-Stokes solutions of Dennis and Dunwoody, (1966) supported the existence of an $R^{-3/8}$ region, and even confirmed the value of $T(0)$, which is difficult in view of the singularity in skin friction present at the trailing edge (on the smallest, $O(R^{-3/4})$ scale analyzed by Stewartson (1968)). Since (6.1) and (6.2) are in conflict, they suggested that the $O(R^{-1})$ term in (6.1) was canceled by further terms in the triple deck expansion.

Now, at a Reynolds number of 100, the leading edge of the plate is at $X = -1.84$, not its asymptotic value $X = -\infty$. Comparing the actual skin friction with the triple deck prediction shows that the latter is also too small by a factor of about 2. The accidental agreement in drag must come from the inclusion in the integrated skin friction of the range from $-\infty$ to the leading edge.

6.2 Computations.

The skin friction results of Dennis and Dunwoody are sufficient to show that all is not well, but it is hard to extract detailed information from their graphs. We decided to solve the Navier-Stokes equations for a range of medium Reynolds numbers using our existing multigrid program. One difficulty was that the desired high order correction to the skin friction is caused by the upstream influence of the wake, which must therefore be well represented in the solution.

The downstream boundary condition for the vorticity is not crucial, because the equation governing the vorticity is largely parabolic in the wake, so errors made downstream decay exponentially upstream. We used $\omega_x = 0$ in the wake and $\omega = 0$ elsewhere. The stream function is more important—imposing the free stream condition would violate conservation of momentum—and we use the Oseén wake, given by Imai (1951). It has been pointed out by Fornberg (1980) that the Oseén wake is of no practical use in finding the far field of flow past a bluff body, because in addition to the narrow wake there is another large irrotational effect due to the trailing eddies. However, these are not present in our problem, so we expect Imai's approximation to apply at modest distances from the plate.

The computational coordinates are (ξ, η) as in the corner flow problem. The upper half plane maps into $\xi > 0$, $0 \leq \eta \leq \pi$, so the plate length is 2. (All our results have been translated into the plate length 1 case.) The first three terms of the far field expansion of the stream function can be written

$$\begin{aligned} \psi &= \psi_0 + \psi_1 + \psi_2 \\ \psi_0 &= y \\ \psi_1 &= -C_D\,(\mathrm{erf}(Q) - \theta/\pi) \\ \psi_2 &= -\frac{C_D^2}{2\sqrt{\pi}\nu P}\left(\sqrt{2}\,\mathrm{erf}(\sqrt{2}\,Q) - \exp(-Q^2)\mathrm{erf}(Q)\right) - \frac{A}{P}\exp(-Q^2) \end{aligned} \tag{6.3}$$

where

$$P = (r/\nu)^{1/2}\cos(\theta/2),$$

$$Q = (r/\nu)^{1/2}\sin(\theta/2),$$

A is an unknown constant, and (r, θ) are polar coordinates for (x, y).

This apparently does not agree with the formula used by Dennis and Dunwoody (1966), but it can be shown to be equivalent in the wake region to the result of Goldstein (1930). He found that the far wake merged smoothly with the near similarity wake if the origin for the former were $x = 0.48$. This is close enough to $x = \frac{1}{2}$ that we may take the origin for the Oseén expansion at the center of the plate, and use (6.3) directly. Any discrepancy can be absorbed in the constant A in the second order term.

$C_D = \nu \int_0^\pi \omega \sin\eta \, d\eta$ is recalculated after each relaxation and the first two terms of the expansion are imposed as a Dirichlet condition at a fixed value of $\xi = \xi_\infty$. Then ξ_∞ was increased until the flow had converged adequately.

The drag converged rapidly, since its main contribution comes from the singularity at the leading edge. τ was more sensitive, but did not change appreciably when the downstream boundary was moved from 8 to 20 plate lengths behind the trailing edge. As far as could be determined, τ agreed with the results in Dennis and Dunwoody.

Initially, with $\xi_\infty = 3.5$ and a 192×160 grid, τ appeared to have converged, but the vorticity in the downstream wake did not match its expected asymptotic

values. This was because the grid stretching downstream caused the wake to diffuse too quickly. Thus, it was necessary to locally refine the grid once in the wake by using a one level finer grid there, which cured the problem. For R =600, the highest Reynolds number considered, accuracy was checked on a 320×224 grid with a 440×50 refinement in the wake. We estimate that the relative error in the skin friction in this calculation is about 0.3%; however, we are mainly interested in the higher order correction, a small effect: this has a magnified relative error of about 2%. As in Chapter 3, the errors at smaller Reynolds numbers are much smaller.

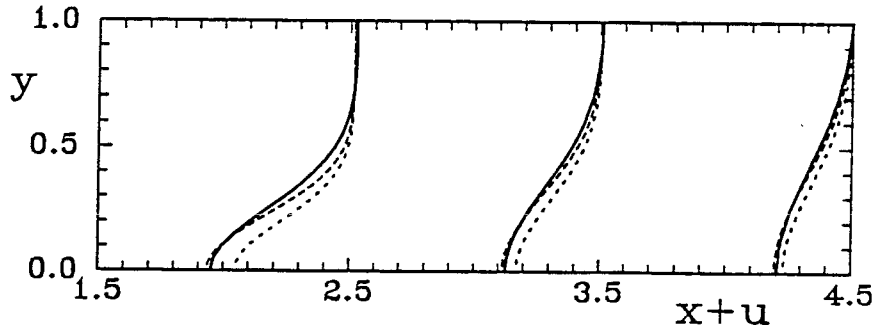

Figure 6.1 Velocity profiles in the wake

Here R = 200 and the solid lines are the velocity profiles at x =1.5, 2.5 and 3.5. The horizontal scale is the same for x and u. The dotted lines show the first order Oseén wake and the dashed lines show the second order wake with $A = 0$.

Our main interest in not in the wake, but it can be checked against the Oseén expansion given above. This is done in Figure 6.1 for $R = 200$ at three downstream positions, for the two and three term expansions with $A = 0$. ($A \neq 0$ did not significantly improve the agreement). Clearly the results are consistent with the Oseén wake. The near wake is more problematical, and in fact there is no clear region in which the $u(x,0) \sim x^{1/3}$ Goldstein similarity solution is evident. This is because close to the trailing edge, the full Navier-Stokes equations apply and instead we see $u(x,0) \sim x^{1/2}$. The expected scaling (see §6.4 below) was verified and we find

$$u(x,0) = Re^{1/4} X_{\rm te}^{1/2}(0.46 - 0.027X_{\rm te} + O(X_{\rm te}^2)), \tag{6.4}$$

where $X_{\rm te} = Re^{3/4}(x-1)$.

Table 6.1 gives the actual and relative drag coefficients, and τ is shown in Figure 6.2 for R =25, 50, 100, 200, 400 and 600. Notice that the skin friction is still more than 12% larger than the Blasius value even at $R = 600$. Various features are evident, which are discussed tentatively below. However, just as it is easy to err in considering only integral properties like the drag, so it is easy to mistake one weak asymptotic feature for another.

Table 6.1 Drag of a finite flat plate

R	C_D	D
25	0.4126	1.5530
50	0.2701	1.4379
100	0.1788	1.3460
200	0.1197	1.2742
400	0.0807	1.2145
600	0.0642	1.1847

6.3 The leading edge.

The increase in τ near the leading edge, which is sharper for higher Reynolds numbers, is believed to be a local viscous effect identical to that seen in the semi-infinite plate, as noted by Van Dyke (1964). Although formally confined to the viscous length scale R^{-1}, it is still about 0.05 at $Rx = 100$, which is why it shows up here. The amount of increase can be taken from the Navier-Stokes solution for flow past a semi-infinite flat plate of van de Vooren and Dijkstra (1970); the values we used are given in Table 6.3 at the end of the chapter. Sure enough, if this effect is subtracted off, τ looks similar near the leading edge for all Reynolds numbers—compare the leading edge region in Figures 6.2 and 6.3. The remaining discrepancy is thought to be a higher order effect, due to the fact that the external velocity is not exactly 1 at the leading edge.

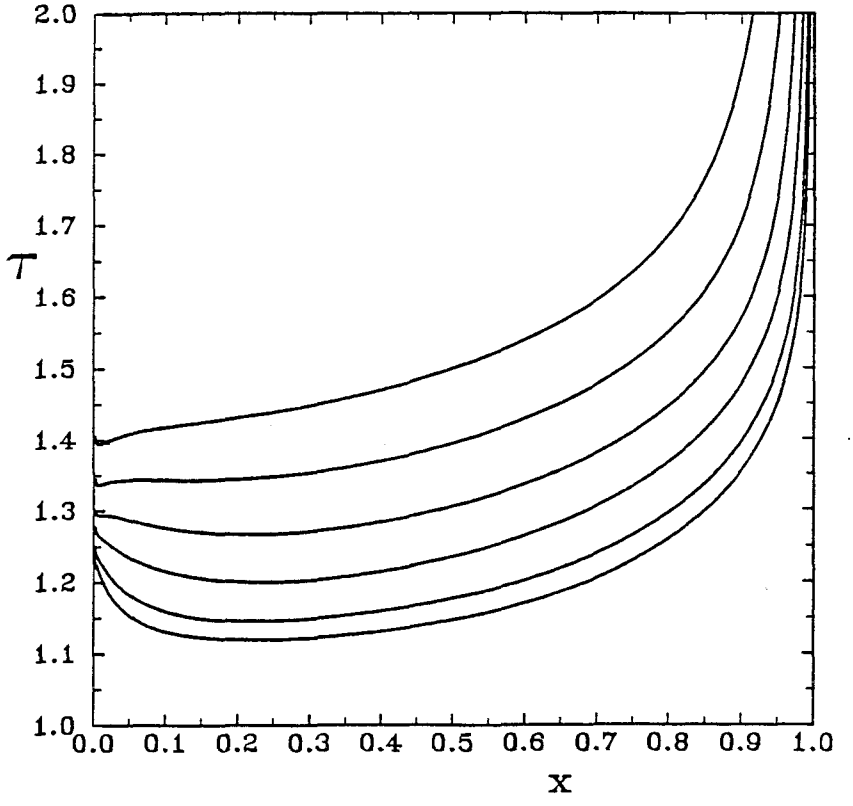

Figure 6.2 Higher order skin friction on a flat plate

τ= (skin friction)/(Blasius skin friction) is shown here for R =25, 50, 100, 200, 400, and 600; τ decreases with increasing Reynolds number.

6.4 The trailing edge.

Locally, the square root singularity of Carrier and Lin (1948) applies, which explains the blow-up in Figure 6.2 as $x \to 1$. However, it has been shown to apply only in a region of extent $R^{-3/4}$, and, in fact, on that scale the flow rapidly converges and is found to be given by

$$c_f = R^{1/2}|X_{te}|^{-1/2}\left(0.46 + 0.17|X_{te}| + O\left(X_{te}^2\right)\right) \tag{6.5}$$

where $X_{te} = (x-1)R^{3/4}$. (The coefficient of the quadratic term is about -0.027). Stewartson (1968) solved the linearized problem and found the constants in (6.5) to be 0.59 and 0.15. (Since this region is entirely contained in the innermost layer of the triple deck, his linear shear λ has been replaced here by the increased value 1.343×0.3321 due to the triple deck). The equality of the constants in (6.4) and (6.5)

can be shown from the Carrier-Lin solution $\psi = Ar^{3/2}(\sin\frac{1}{2}\theta + \sin\frac{3}{2}\theta)$, where r and θ are polar coordinates measured from the trailing edge.

The effect in (6.5) is significant out to $X_{te} \sim 2.8$, which is similar to the extent seen in the local Navier-Stokes solution of Schneider and Denny (1971) at $R = 10^5$, although they did not fit a singularity. This corresponds to $x = 0.91$ at $R = 100$, and $x = 0.98$ at $R = 600$. The drag due to (6.5) is difficult to calculate because of the smooth merging with the rest of the flow. However, the increased drag due to the *excess* skin friction is clearly positive, in contrast to the $-0.11R^{-5/4}$ given by Stewartson; we do not know the reason for this discrepancy.

The trailing edge singularity frustrates efforts to find the rest of the flow near there. It cannot simply be subtracted off (like the leading edge) because it is not a small effect, and is not known *a priori*. We shall simply have to rely on its small lateral extent not to confuse matters.

6.5 The triple deck assumed.

Recall from (6.2) that to first order, the triple deck effect in τ is of constant magnitude and $O(R^{-3/8})$ spatial extent. It is clear from Figure 6.2 that not all the variation is going to be explained by this. At $x = 0.2$, for example, the relative effect $\sqrt{x}\,T(X)$ is only about .03–.04. Consequently the first step was to assume that the triple deck was in fact present, subtract it off, and see what was left. The values of $T(X)$ used are given in Table 6.3 at the end of the chapter. The remainder turns out to be proportional to $R^{-1/2}$ everywhere on the plate, which would correspond to an overall displacement effect of the boundary layer and wake. This is shown in Figure 6.3. Over most of the plate there is only a small additional decrease of about 8% as R increases by a factor of 24, and a small increase closer to the trailing edge. The trailing edge singularity is seen to the right. The data thus suggest that other effects, such as successive terms in the triple deck expansion (the first of which would be $O(R^{-1/8})$), must be relatively small.

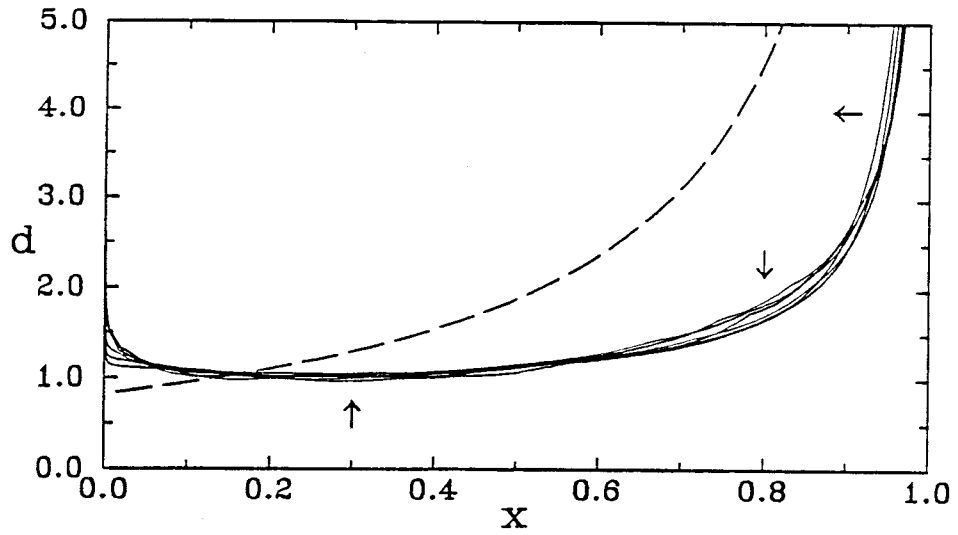

Figure 6.3 Displacement effect on the boundary layer

The remainder when the leading edge and triple deck effects are subtracted from τ is found to behave like $R^{-1/2}$. It is shown here scaled by $R^{1/2}$, where R is as in Figure 6.2. Arrows show the direction of decreasing R. (Slow wiggles are caused by interpolation of the subtracted functions.) The trailing edge singularity is seen to the right.
The dashed line is Kuo's displacement effect $K(x)$.

6.6 The triple deck confirmed?

To see if there was *a priori* evidence in the data for a trailing edge region of the triple deck kind, a least squares fit to τ was made of the form

$$\tau(x_i, R_j) = 1 + R_j^{-1/2} g(x_i) + \sqrt{x_i}\, h(X(x_i, R_j)), \quad 1 \le i \le N,\ 1 \le j \le p, \qquad (6.6)$$

where $X = \lambda^{5/4} R^{\alpha}(x-1)$. The unknowns are the displacement effect $g(x_i)$ and the triple deck effect $h(X_k)$, $1 \le k \le M$. h is linearly interpolated from its values at X_k to get a value at $X(x_i, R_j)$. This helps to couple the unknowns if M is not too large. The x_i's and X_k's are equally spaced. Of course, (6.6) is already quite restrictive, (i.e., the R dependencies of the effects are assumed), but we don't want to have too many unknowns and overfit the data. With $\alpha = 3/8$, the mean error in (6.6) is .0025, and we do indeed find the triple deck effect: $|h(X) - T(X)| < .005$ for $-2 < X < 0$. At large X there are less data and the error is larger, as it is at $X = 0$, since here h has been extrapolated, and we found $h(0) = 0.32$ as compared to $T(0) = 0.343$. Possibly a similar procedure was used by Dennis and Dunwoody (1966) as quoted by

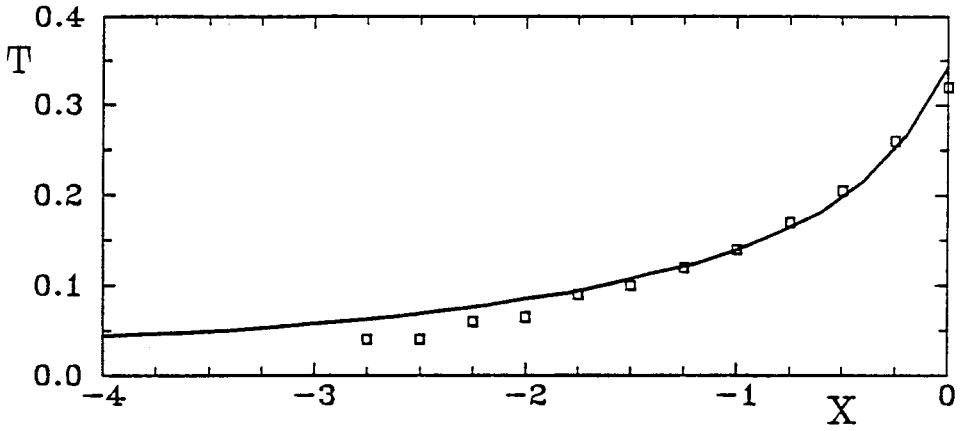

Figure 6.4 Least squares fit of the triple deck effect

The points are the fitted values $h(X_k)$, $1 \leq k \leq 12$, and the solid line is the triple deck solution of Jobe and Burggraf (1974).

Jobe and Burggraf (1974). The fit is shown in Figure 6.4 when $N = 19$, $M = 12$, $p = 4$ and R_j =100, 200, 400 and 600.

However, a fit with comparable mean error is also possible with other values of α, including $\alpha = 0$! Although this is rejected on theoretical grounds (h would then be part of the first order boundary layer), it does appear that there is no conclusive evidence of a region that scales with $R^{-3/8}$ over this range of Reynolds numbers. There is stronger evidence if we also consider the data obtained by Schneider and Denny (1971), who used an interactive boundary layer approach at $R = 10^5$, apparently applied in the range $0.5 < x < 2$. At this Reynolds number, displacement effects are negligible, and their calculated pressure disturbance covers an extent consistent with the triple deck.

6.7 Decomposition of friction and drag.

Our final proposed approximation is now clear. For $(1 - x)R^{3/4}$ less than about 2.8, c_f is given by (6.5); away from there, we have

$$\tau \approx 1 + L(Rx) + \sqrt{x}\,T(X) + R^{-1/2}d(x), \tag{6.7}$$

where L is the viscous contribution from the leading edge and we suggest that $d(x)$ is a displacement effect. These competing effects are shown in Figure 6.5 for R=600—clearly they are all significant. The contribution to the drag from L is asymptotically

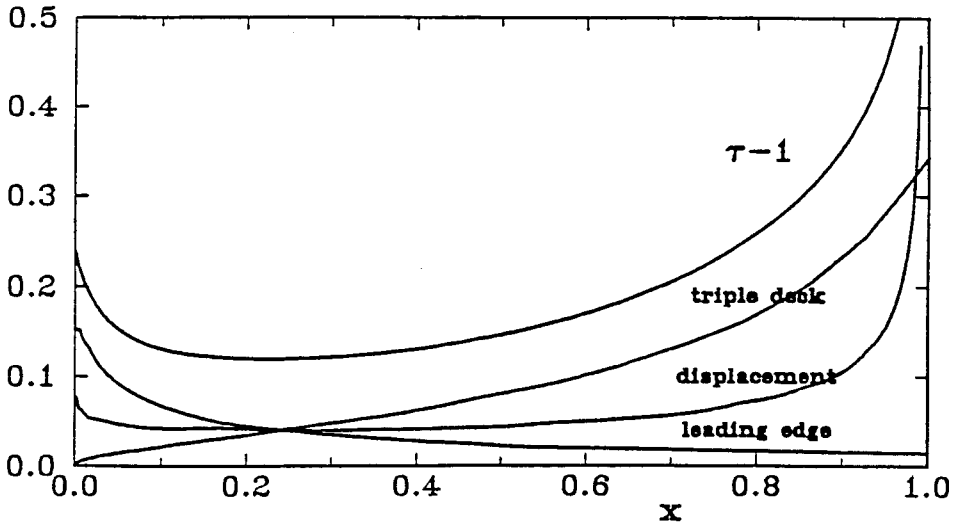

Figure 6.5 Decomposition of skin friction for $R = 600$

$2.326R^{-1}$. (Van Dyke (1964) apparently includes only half of this). Relative to the Blasius drag, this is $1.75R^{-1/2}$. The relative drag due to $d(x)$ is $1.49R^{-1/2}$. The contribution from the triple deck is

$$\begin{aligned}\frac{1}{2}\int_0^1 T(X(x))\,dx &= \frac{1}{2X}\int_{X(0)}^0 T(X)\,dX \\ &\sim \frac{1}{2X}\left(\int_{-\infty}^0 T(X)\,dX - \int_{-\infty}^{X(0)} 0.3106(-X)^{-4/3}\,dX\right) \quad \text{as } R\to\infty \\ &= 2.00R^{-3/8} - 2.93R^{-1/2} \end{aligned} \tag{6.8}$$

So, combing the four effects in (6.7), we have

$$D \approx 1 + 2.00R^{-3/8} + 0.31R^{-1/2}. \tag{6.9}$$

Table 6.2 shows that all three effects are significant for moderate Reynolds numbers. The reason for the good agreement with the drag found by Jobe and Burggraf (1974) is now clear: the terms of order $R^{-1/2}$, arising from three different sources, almost cancel, and their total is much smaller than the $R^{-3/8}$ term even for moderate Reynolds numbers. Of course, (6.9) is not formally accurate to the order written because there are also contributions from the next terms in the triple deck expansion which are $O(R^{-1/2})$. However, as noted in §6.5, inspection of the skin friction shows that these are expected to be small.

Table 6.2 Contributions to the drag.

Effect	$R = 100$	$R = 200$	$R = 400$	$R = 600$
actual drag	1.346	1.274	1.215	1.185
Blasius	1	1	1	1
triple deck	0.094	0.084	0.074	0.068
leading edge	0.103	0.084	0.066	0.057
remainder	0.149	0.106	0.075	0.060
power law fit to remainder: $R^{-0.50}$				

6.8 The displacement effect.

It is not possible to be absolutely sure that we have identified the correct asymptotic behavior of τ over the whole range of x based on a study of a small number of finite Reynolds numbers, although Schneider and Denny's study confirms that we have not misidentified the triple deck. The main problem concerns the cause of $d(x)$. As seen in Figure 6.3, it is completely different from the displacement effect calculated by Kuo (1953); in fact, it is roughly constant over the whole plate (away from the trailing edge singularity). We have confirmed Kuo's power series expansion of the boundary layer via a direct integration of the boundary layer equations. It is true that the jump in vertical velocity at $x = 1$ assumed by Kuo is in fact smoothed out by the third term in the triple deck expansion, thus removing the logarithmic singularity he found in $K(x)$; however, *away* from the trailing edge his analysis should still be valid. Either his approximation that the vertical velocity is zero in $x > 1$ is not valid, and the slow broadening of the wake downstream makes the "sink" effect of the finite plate less severe or local (triple deck) and global effects are so hopelessly intermingled at these moderate Reynolds numbers as to render our decomposition suspect. The computation of $T(X)$ in §6.5 remains in its favor, however.

Table 6.3 Magnitudes of leading edge and triple deck effects

Values taken from van de Vooren and Dijkstra (1970) and Jobe and Burggraf (1974), respectively.

$\log_{10} Rx$	0	0.5	1	1.5	2	2.5	3
$L(Rx)$	0.1524	0.1518	0.1316	0.0901	0.0488	0.0211	0.0087

$-X$	0.0	0.2	0.4	0.6	0.8	1.0	1.2	1.4	1.6	1.8
$T(X)$	0.343	0.266	0.216	0.182	0.160	0.140	0.124	0.114	0.102	0.092
$-X$	2.0	2.2	2.4	2.6	2.8	3.0	3.2	3.4	3.6	3.8
$T(X)$	0.086	0.078	0.072	0.066	0.062	0.058	0.054	0.050	0.048	0.046

$$T \sim 0.3106(-X)^{-4/3} \text{ as } X \to \infty$$

Chapter 7

Suggestions for further research

Our experience with multigrid has been similar to that of others: it is fairly easy to get a converged solution of some sort, but harder to get solutions at higher Reynolds numbers, and to pinpoint the area that is limiting the convergence rate. Achi Brandt's view is that at large Reynolds numbers, distinct phenomena may cause different problems in different parts of the flow field, so that to achieve increased performance it will be necessary for the program to recognize the local nature of the flow (e.g., inviscid, a shear layer, or fully viscous) and to take action accordingly.

A frustration of our work is that we have not been able to identify the cause of convergence failure at $Re = 6000$. We can only reiterate what is *not* at fault.

It is not a coarse grid problem, unless inverting $\tilde{L}$ rather than L on the coarsest grid commits a systematic error: removing the coarsest or the two coarsest grids gave identical results. The linear advection-diffusion equation considered in Chapter 2 can be solved with an asymptotic convergence rate of 0.5 at any Reynolds number, so we suspect that some aspect of the flow field itself is the culprit. The cell Reynolds number in the main part of the eddy, admittedly only about 5 in the undriven flows of Chapter 3, does not seem to be causing problems, as the driven flows of Chapter 4 converge with much higher cell Reynolds numbers (15–20) throughout the flow.

An algorithm in which artificial viscosity is used both in smoothing and in computing the defect also shows degraded convergence at about the same Reynolds number. This suggests that one potential problem—wiggles due to central differencing in the defect—has not yet set in. This is also indicated by our observation that limiting the defect corrections to the interchange between the two finest grids never improves convergence.

Thus, a good problem to study is the effect of unaligned internal shear layers on the convergence of a two grid cycle without defect correction.

Although our results could have been obtained with other methods, multigrid has given us the accurate results that made possible the confirmation of the Sychev model of laminar separation.

The results of Chapter 3 suggest three main questions on the nature of high Reynolds number flows:

1. The vorticity is substantially constant in the main part of the eddy by $Re = 3000$. Boundary layer theory could in principle give the limiting value of this plateau vorticity ω_0 by a consistency argument: the boundary layer must be continuous after being integrated around the eddy. However, ω_0 is still increasing almost linearly at $Re = 5000$, and even more rapid increases are observed in other flows (Fornberg 1985, Milos, Acrivos and Kim 1987). What asymptotic process controls the value of ω_0?
2. What is the asymptotic structure of the sequence of eddies that forms in the cusp, and do they have any effect on the primary separation?
3. What is the asymptotic structure of the colliding shear layers at the rear of a Prandtl-Batchelor flow?

The next two chapters are more conclusive. Although we have certainly demonstrated that simple Prandtl-Batchelor flows are indeed the limit of viscous flows at infinite Reynolds number, if the boundary conditions are chosen appropriately, the flows are unlikely to be of interest for themselves except for possible theoretical attention because of their simple structure.

Chapter 5 substantially confirms the triple deck model of laminar separation. It also suggests that the reason its predictions are not observed in other flows is that higher order effects can be comparatively large at the Reynolds numbers used in practice.

The conclusion of Chapter 6, on the flow over a finite flat plate, is simple: don't

believe everything you read. Hasty comparisons of only one flow quantity (the drag) gave accidentally good results in previous studies. We increase the dimension by one and study the skin friction, and in so doing may be falling into the same trap (but at a higher order). Nevertheless, the displacement-like effect seen in the boundary layer is real and substantial and remains to be explained.

References

Auzinger, W. (1987a), Defect corrections for multigrid solutions of the Dirichlet problem in general domains. *Math. Comput.* **48**, 471–484.

Auzinger, W. (1987b), Defect correction for nonlinear elliptic difference equations. *Numer. Math.* **51**, 199-208.

Batchelor, G.K. (1956), A proposal concerning laminar wakes behind bluff bodies at large Reynolds number. *J. Fluid Mech.* **1**, 380–398.

Batchelor, G.K. (1967), *An Introduction to Fluid Mechanics.* Cambridge University Press, Cambridge.

Blasius (1908), *Z. Math. Phys.* **56**. 1.

Brandt, A. (1984), Multigrid methods: 1984 guide with applications to fluid dynamics. Weizmann Institute of Science, Rehovot, Israel.

Brodetsky, S. (1923), Discontinuous fluid motion past circular and elliptic cylinders. *Proc. R. Soc. Lond. A* **102**, 542.

Brown, S.N. and Stewartson, K. (1969), Laminar separation. *A. Rev. Fluid Mech.* **1**, 45.

Carrier, G.F. and Lin, C.C. (1948). On the nature of the boundary layer near the leading edge of a flat plate. *Quart. Appl. Math.* **6**, 63–68.

Dennis, S.C.R. and Dunwoody, J. (1966), The steady flow of a viscous fluid past a flat plate. *J. Fluid Mech.* **24**, 577–595.

de Zeeuw, P.M. and van Asselt, E.J. (1985), The convergence rate of multi-level algorithms applied to the convection-diffusion equation. *SIAM J. Sci. Stat. Comput.* **6** no. 2, 492–503.

Fornberg, B. (1980), A numerical study of steady viscous flow past a circular cylinder. *J. Fluid Mech.* **98**, 819–855.

Fornberg, B. (1985), Steady viscous flow past a circular cylinder up to Reynolds number 600. *J. Comp. Phys.* **61**, 297–320.

Goldstein, S. (1930), Concerning some solutions of the boundary layer equations in hydrodynamics. *Proc. Camb. Phil. Soc.* **26**, 1–30.

Ghia, U., Ghia, K.N. and Shin, C.T. (1983), High-Re solutions for incompressible flow using the Navier-Stokes equations and a multigrid method. *J. Comp. Phys.* **48(3)** 387–411.

Hackbusch, W. (1985), *Multi-grid Methods and Applications.* Springer series in computational mathematics, vol. 4. Springer 1985.

Howarth, L. (1938), On the solution of the laminar boundary layer equations. *Proc. R. Soc. Lond. A* **164**, 547–579.

Imai, I. (1951), On the asymptotic behavior of viscous fluid flow at a great distance from a cylindrical body, with special reference to Filon's paradox. *Proc. Roy. Soc. A* **208**, 487–516.

Jobe, C.E. and Burggraf, O.R. (1974), The numerical solution of the asymptotic equations of trailing edge flow. *Proc. Roy. Soc. A* **340**, 91–111.

Korolev, C.P. (1980), *TsAGI, Uch. Zap.* **XI.3**, 7–16.

Kuo, Y.H. (1953), On the flow of an incompressible viscous fluid past a flat plate at moderate Reynolds numbers. *J. Math. and Phys.* **32**, 83–101.

Leal, L.G. (1973), Steady separated flow in a linearly decelerated free stream. *J. Fluid Mech.* **59**, 513–535.

Melnik, R.E. and Chow, R. (1975), Asymptotic theory of two-dimensional trailing edge flows. *Grumman Res. Dept. Report* RE–5105.

Messiter, A.F. (1970), Boundary-layer flow near the trailing edge of a flat plate. *SIAM J. Appl. Math.* **18**, 655-670.

Messiter, A.F. (1975), Laminar separation—a local asymptotic flow description for constant pressure downstream. *AGARD Symposium on Separated Flows.*

Milos, F.S., Acrivos, A. and Kim, J. (1987), Steady flow past sudden expansions at large Reynolds number II. Navier-Stokes solutions for the cascade expansion. *Phys. Fluids* **30**, 7–18.

Moore, D.W., Saffman, P.G. and Tanveer, S. (1988), The calculation of some Batchelor flows: the Sadovskii vortex and rotational corner flow. *Phys. Fluids* **31(5)** 978–990.

Prandtl, L. (1905) Motion of fluids with very little viscosity. Göttingen; translation in NACA TM–452 (1928).

Rosenhead, L., ed. (1963), *Laminar Boundary Layers.* Oxford University Press, Oxford.

Schneider, L.I. and Denny, V.I. (1971), Evolution of the laminar boundary layer behind a flat plate and its upstream influence. *A.I.A.A. J.* **9**, 655–660.

Schreiber, R. and Keller, H.B. (1983), Driven cavity flows by efficient numerical techniques. *J. Comp. Phys.* **49** no. 2, 310–333.

Schröder, W. and Keller, H.B. (1990), Wavy Taylor vortices. *J. Comp. Phys.*, to appear.

Smith, F.T. (1977), The laminar separation of an incompressible fluid streaming past a smooth surface. *Proc. R. Soc. Lond. A* **356** 443–463.

Smith, J.H.B. (1982), The representation of planar separated flow by regions of uniform vorticity, in *Vortex Motion* (Vieweg, Braunschweig), pp. 157–172.

Stewartson, K. (1968), On the flow near the trailing edge of a flat plate, *P. Roy. Soc. A* **306**, 275–290.

Stewartson, K. (1969), On the flow near the trailing edge of a flat plate II, *Mathematika* **16**, 106–121.

Stewartson, K. (1974), Multistructured boundary layers on flat plates and related bodies. *Adv. Appl. Mechs.* **14**, 145.

Sychev, V.V. (1972), Concerning laminar separation. *Izv. Akad. Nauk. SSSR, Mekh., Zhidk. Gaza* **3**, 47–59.

Sychev, V.V. (1979), Boundary layer separation from a plane surface. *TsAGI, Uch. Zap.* **IX.3**, 20–29 (1979); translation in NASA TM–75828.

Van de Velde, E.F., and Keller, H.B. (1987), The parallel solution of nonlinear elliptic equations. In *Parallel Computations and Their Impact on Mechanics*, ed. A.K. Noor, pp. 127–153.

van de Vooren, A.I., and Dijkstra, D. (1970), The Navier-Stokes solution for laminar flow past a semi-infinite flat plate. *J. Eng. Math.* **4**, 9–27.

van Dommelen, L.L., and Shen, S.F. (1984), Interactive separation from a fixed wall, *Proc. Symp. Numer. Phys. Aspects Aerodyn. Flows, 2nd Long Beach Conference*, ed. T. Cebeci, Springer Verlag.

Van Dyke, M.D. (1964), *Perturbation Methods in Fluid Mechanics.* Parabolic Press, Stanford, p. 39.

Veldman, A.E.P. and van de Vooren, A.I. (1974), Drag of a finite flate plate. *Proc. 4th Int. Conf. Num. Meth. Fluid Dyn.*, 423–430.